Universität Bremen

Modeling Insights into Arctic Climate and Cryospheric Characteristics during Past Interglacials

Kumulative Dissertation

zur Erlangung des akademischen Grades eines Doktors der Naturwissenschaften

- Dr. rer. nat. -

Fachbereich 5 – Geowissenschaften

Brian R. Crow

Mai 2024

Betreuung der Promotion durch:

Prof. Dr. Michael Schulz

Dr. Matthias Prange

MARUM – Zentrum für Marine Umweltwissenschaften
Fachbereich Geowissenschaften (FB5), Universität Bremen

Weitere Mitglieder des beratenden Ausschusses für die Promotion:

Prof. Dr. Lev Tarasov

Department of Physics and Physical Oceanography
Memorial University of Newfoundland
St. John's, NL, Canada

Prof. Dr. Ben Marzeion

Fachbereich Geographie (FB8), Universität Bremen

Erstgutachter:

Prof. Dr. Michael Schulz

MARUM – Zentrum für Marine Umweltwissenschaften

Geowissenschaften, Universität Bremen

Zweitgutachter:

Prof. Dr. Christoph Raible

OCCR – Oeschger Centre for Climate Change Research

Climate and Environmental Physics, University of Bern

Datum des Promotionskolloquiums: 20. September 2024

Versicherung an Eides Statt / *Affirmation in lieu of an oath*

gem. § 5 Abs. 5 der Promotionsordnung vom 28.04.2021 /

according to § 5 (5) of the Doctoral Degree Rules and Regulations of 28 April, 2021

Ich / I, Brian R. Crow,
(Vorname / First *Name*, Name / *Name*, Anschrift / *Address*, ggf. Matr.-Nr. / *student ID no., if applicable)*

versichere an Eides Statt durch meine Unterschrift, dass ich die vorliegende Dissertation selbständig und ohne fremde Hilfe angefertigt und alle Stellen, die ich wörtlich dem Sinne nach aus Veröffentlichungen entnommen habe, als solche kenntlich gemacht habe, mich auch keiner anderen als der angegebenen Literatur oder sonstiger Hilfsmittel bedient habe und die zu Prüfungszwecken beigelegte elektronische Version (PDF) der Dissertation mit der abgegebenen gedruckten Version identisch ist. / *With my signature I affirm in lieu of an oath that I prepared the submitted dissertation independently and without illicit assistance from third parties, that I appropriately referenced any text or content from other sources, that I used only literature and resources listed in the dissertation, and that the electronic (PDF) and printed versions of the dissertation are identical.*

Ich versichere an Eides Statt, dass ich die vorgenannten Angaben nach bestem Wissen und Gewissen gemacht habe und dass die Angaben der Wahrheit entsprechen und ich nichts verschwiegen habe*. / I affirm in lieu of an oath that the information provided herein to the best of my knowledge is true and complete.*

Die Strafbarkeit einer falschen eidesstattlichen Versicherung ist mir bekannt, namentlich die Strafandrohung gemäß § 156 StGB bis zu drei Jahren Freiheitsstrafe oder Geldstrafe bei vorsätzlicher Begehung der Tat bzw. gemäß § 161 Abs. 1 StGB bis zu einem Jahr Freiheitsstrafe oder Geldstrafe bei fahrlässiger Begehung. / *I am aware that a false affidavit is a criminal offence which is punishable by law in accordance with § 156 of the German Criminal Code (StGB) with up to three years imprisonment or a fine in case of intention, or in accordance with § 161 (1) of the German Criminal Code with up to one year imprisonment or a fine in case of negligence.*

Wiesbaden,
Ort / *Place*, Datum / *Date*

Unterschrift / *Signature*

Acknowledgements

The journey to completing a doctorate is a long one and involves a great deal of support from many people along the way. I'd like to begin by acknowledging those most directly involved in this work, my advisors Matthias and Michael. Beginning with their initial willingness (and even enthusiasm) to take on an American who'd already given up on the academic system once and continuing through when I told them I'd be taking on a full-time job before finishing this dissertation, they never wavered in their commitment to helping me get across the finish line. I'm very grateful for the opportunity that I was given and am proud of the fruits of our partnership.

Of course, the project for which Matthias and Michael selected me was only possible because of the ArcTrain program. Despite the unfortunate necessity of severely reducing our in-person activities (including international ones with our Canadian colleagues), many of my academic and personal highlights from my PhD come from ArcTrain scientific meetings and informal get-togethers. Being a foreigner in a new country with very limited language skills is often an isolating experience, but I'm grateful to the members of my ArcTrain cohort for being among the most accepting people I've yet encountered here.

In a related sense, I'd like to thank Lev Tarasov and his research group at Memorial University of Newfoundland and Canada for their comradery and expanding my scientific horizons during my ArcTrain-sanctioned visit to them in the fall of 2021. Ice sheet dynamics were at that point a relatively unfamiliar concept to me, but I learned a tremendous amount during my short 2.5 months there. Writing my second paper with Lev was also a rewarding experience and I am proud of our contribution to the literature.

There are also numerous non-ArcTrain friends, colleagues, and former roommates to whom I am grateful, including my cast of former officemates Andrès, Donghao, Sebastian, Anouk, and Marilena. Work was certainly much more enjoyable with you around. The same goes for my other GeoMod group colleagues, with whom coffee breaks and lunches were always a great way to recharge and, often times, learn something about German culture.

The last stages of this PhD have been by far the hardest for me, in no small part due to the extra challenge I heaped on myself by taking on full-time work as a natural catastrophe modeler in July 2023. However, my colleagues and department leadership at this new endeavor have been nothing but supportive of my ill-conceived plans to essentially have two difficult jobs simultaneously, from granting me extra time off for my PhD defense to simply being thoughtful and sympathetic conversation partners.

Finally, I would like to express my unending gratitude to my family, both in Germany and abroad. It will never cease to be difficult living so far away from my parents, but they have continued to support my decisions regardless. I know that their now multi-lingual, PhD-holding son is a huge source of pride for them, and I just want to convey in return how they have done so much to make my pursuits possible. I will always love and be

grateful to them. And to my partner, Alex, I don't even know how to express my gratitude for everything you've done for me. It's no exaggeration to say that I likely would have quit at some point in these last couple of years without you – maybe just on my PhD, maybe on life in Germany as a whole. Our little "German family" means the world to me, and I'm looking forward to regaining my nights and weekends to spend so much more time together. I love you and will forever be thankful for everything you've done.

Abstract

The melt of both the Greenland ice sheet (GrIS) and Arctic sea ice cover have accelerated in recent decades as the anthropogenic effects on the climate system continue to compound. Given the various complexities involved in accurately modeling the dynamics of both Arctic sea ice and the GrIS even in the present day, a look back into past interglacials can yield insights into how sea ice and the ice sheet may have behaved under similarly warm (or yet warmer) conditions to today. Proxy data containing information about past sea ice cover and ice-sheet configurations is severely limited, and as such, climate modeling is perhaps our most powerful tool for understanding ancient climate. This dissertation therefore consists of modeling-centric studies which seek to understand what properties were unique to the two most recent warmer-than-present interglacials, Marine Isotope Stages 5e (MIS-5e) and MIS-11c, and how they impacted the northern hemispheric cryosphere.

MIS-11c has long been identified as a unique interglacial, featuring an unusually long period of moderately warm global temperatures despite relatively weak orbital forcing conditions. Limited proxy evidence indicates that Arctic temperatures were several degrees warmer than preindustrial and a large fraction of the GrIS likely melted. Our first research question was therefore, are specific atmospheric feedbacks involved in contributing to the robust warmth and melt of the GrIS in MIS-11c? Our investigation using the CESM v1.2.2 climate model revealed, as expected, a robustly warmed Arctic and enhanced intertropical convergence zone (ITCZ) activity, leading to a reduced state of baroclinicity across the Northern Hemisphere (NH). Somewhat unexpectedly, however, this led to the emergence of a favored single equatorward-shifted jet state over the North Atlantic, reducing eddy heat flux over Greenland. Therefore, the dynamic consequences of strong Arctic warming produced a negative feedback to further atmospheric warming over Greenland, weakening northward atmospheric heat transport in MIS-11c. The contribution of atmospheric circulation changes to sustained heat and GrIS melt in MIS-11c therefore appears negative, at least over the North Atlantic sector.

Despite this apparent contradiction, a mixture of geologic evidence suggests that during MIS-11c, land ice retreated entirely away from Greenland's coasts, ice at the DYE-3 core site melted completely, and ice survived at the Summit location. Very few other constraints exist, however, so we conducted numerous sets of ensemble ice sheet simulations using the Glacial Systems Model (GSM) and CESM time slice simulations spanning 423 to 398 ka with 5 ka steps in between. In an effort to constrain the coupling uncertainties between ice-sheet model and climate model, the various ensembles employed different techniques for calculating the temperature lapse rate, used different present-day bias-correction datasets, and examined a pair of simplistic precipitation bias corrections. By matching the presence or absence of ice at the Summit and DYE-3 core sites with our model results, we produced a best-matched set of 31 simulations which have a mean sea-level contribution from the GrIS in MIS-11c of 3.9 m (an approximately 50% melt from present day). We furthermore determined that the spatially and temporally varying lapse rate, calculated from climate model data, is the most physically realistic method used and represents a stark improvement over the fixed lapse rates traditionally used by modelers.

Another potential factor influencing the melt of the GrIS in past interglacials is the loss of Arctic sea ice, particularly in the summer and fall. Again using a time-slice modeling approach, we determined that summer sea ice area has a clear inverse relationship with the integrated summer energy (ISE), a metric that accounts for both the varying intensity and length of summer seasons due to orbital variations. Early MIS-5e is characterized by exceptionally high ISE and shows a near-complete disappearance of September Arctic sea ice in our simulations, a result that is at least qualitatively supported by a small number of sediment core proxy records. However, summer sea ice levels are much higher already by our 124 ka simulation and for all MIS-11c simulations, indicating that any ice-free summer conditions in both interglacials must have been confined to a short period in early MIS-5e. Furthermore, the interannual variability is strongly related to the mean summer sea ice area, with low variability occurring at both low and high sea ice areas. Intermediate levels of summer sea ice exhibit the greatest interannual variability due to the presence of large quantities of sea ice across the central Arctic Ocean, where variable weather patterns can have a large seasonal impact on processes such as melt and export of ice. This suggests that the greatest volatility in Arctic summer sea ice regimes occurs during transitional phases between high summer ice concentrations and low summer ice concentrations, a phase that the modern Arctic appears to be entering.

The unifying theme of studies presented in this dissertation is that modeling recent past interglacial states with parallels to today can yield insight into the changes that should be expected in the climate of the near future. We were able to highlight some features of Arctic interglacial climate that appear across very differently-forced climatic periods and offered improved coupling techniques for future paleo-ice-climate modeling. The findings presented here constitute a significant step forward in the understanding of interglacial climate and support ongoing efforts to make better projections of our rapidly changing climate.

Zusammenfassung

Das Abschmelzen des grönländischen Eisschildes (GrIS) sowie des arktischen Meereises hat sich in den letzten Jahrzehnten durch anthropogene Einflüsse erheblich beschleunigt. Da eine Modellierung der Dynamik des arktischen Meereises und des grönländischen Eisschildes selbst in der heutigen Zeit höchst komplex ist, kann ein Blick in vergangene Zwischeneiszeiten Aufschluss darüber geben, wie sich das Meereis und das grönländische Eisschild unter ähnlich warmen bzw. noch wärmeren als heute Temperaturen verhalten haben könnten. Proxydaten, die Informationen über die Meereisbedeckung und die Konfiguration des Eisschildes in der Vergangenheit enthalten, sind nur eingeschränkt verfügbar, daher ist eine Klimamodellierung womöglich unser mächtigstes Werkzeug, um das Klima der Vergangenheit zu verstehen. Aus diesem Grund besteht diese Dissertation aus modellbasierten Studien, die darauf abzielen zu verstehen, welche Eigenschaften die beiden jüngsten wärmeren Interglaziale hatten, die marinen Isotopenstufen 5e (MIS-5e) und MIS-11c, und welche Auswirkung sie jeweils auf die Kryosphäre der nördlichen Hemisphäre hatten.

MIS-11c gilt seit langem als ein einzigartiges Interglazial, das sich durch eine ungewöhnlich lange Periode mäßig warmer globaler Temperaturen trotz relativ schwacher orbitaler Antriebsbedingungen auszeichnete. Begrenzte Beweise deuten darauf hin, dass die Temperaturen in der Arktis um mehrere Grad wärmer waren als in der vorindustriellen Zeit und ein großer Teil des GrIS geschmolzen sein dürfte. Unsere erste Forschungsfrage lautete daher: Spielten spezifische atmosphärische Rückkopplungen eine Rolle bei der starken Erwärmung und dem Abschmelzen des GrIS im MIS-11c? Unsere Untersuchung mit dem Klimamodell CESM v1.2.2 ergab erwartungsgemäß eine stark erwärmte Arktis und eine verstärkte Aktivität der intertropischen Konvergenzzone (ITCZ), was zu einer geringeren Baroklinität auf der Nordhalbkugel führte. Etwas unerwartet führte dies jedoch zur Entstehung eines einzelnen, äquatorwärts verschobenen Jet-Zustands über dem Nordatlantik, der den Wirbelwärmefluss über Grönland reduzierte. Diese dynamischen Folgen der starken Arktiserwärmung führten also während in MIS-11c zu einer negativen Rückkopplung auf die weitere Erwärmung der Atmosphäre über Grönland und schwächten den atmosphärischen Wärmetransport nach Norden. Der Beitrag der atmosphärischen Zirkulationsveränderungen zur anhaltenden Arktiserwärmung und GrIS-Schmelze in MIS-11c scheint daher negativ zu sein, zumindest über dem nordatlantischen Sektor.

Trotz dieses scheinbaren Widerspruchs deutet eine Mischung aus geologischen Beweisen darauf hin, dass sich das Landeis während MIS-11c vollständig von den grönländischen Küsten zurückzog, das Eis am DYE-3-Kern vollständig schmolz und das Eis am Standort Summit überlebte – dies zusammengenommen ist jedoch noch nicht ausreichend. Deshalb haben wir zahlreiche Ensemble-Eisschild-Simulationen mit dem Glacial Systems Model (GSM) und CESM-Zeitscheibensimulationen durchgeführt, die den Zeitraum von 423 bis 398 ka in dazwischen liegenden 5 ka-Schritten abdecken. Um Unsicherheiten bei der Kopplung zwischen dem Eisschildmodell und dem Klimamodell einzugrenzen, wurden in verschiedenen Ensembles unterschiedliche Techniken zur Berechnung des thermischen Höhengradienten verwendet, verschiedene Datensätze zur Korrektur von Verzerrungen in der Gegenwart genutzt und zwei vereinfachte Korrekturen der Niederschlagsmenge untersucht. Indem wir das Vorhandensein bzw. Nichtvorhandensein von Eis an den

Summit- und DYE-3-Eisbohrkernen mit unseren Modellergebnissen abgeglichen haben, haben wir eine am besten übereinstimmende Gruppe von 31 Simulationen erstellt, die einen durchschnittlichen Beitrag des GrIS zum Meeresspiegel im MIS-11c von 3,9 m ergeben hat (dies entspricht einer Schmelze von etwa 50 % gegenüber heute). Außerdem haben wir festgestellt, dass der räumlich und zeitlich variierende thermische Höhengradient, der aus den Klimamodelldaten berechnet wurde, die physikalisch realistischste Methode ist und eine deutliche Verbesserung gegenüber den fixen thermischen Höhengradienten darstellt, die traditionell von Modellierern verwendet werden.

Ein weiterer möglicher Faktor, der zum Abschmelzen des GrIS in vergangenen Zwischeneiszeiten beigetragen hat, ist der Verlust des arktischen Meereises, insbesondere im Sommer und Herbst. Mit Hilfe des Zeitscheibenmodellierungsansatzes haben wir festgestellt, dass die sommerliche Meereisfläche in einem eindeutigen inversen Verhältnis zur integrierten Sommerenergie (ISE) steht, einer Kennzahl, die sowohl unterschiedliche Intensitäten als auch unterschiedliche Längen der Sommersaison aufgrund von orbitalen Variationen berücksichtigt. Das frühere MIS-5e zeichnet sich durch eine außergewöhnlich hohe ISE aus und zeigt in unseren Simulationen ein fast vollständiges Verschwinden des arktischen Meereises im September – ein Ergebnis, das zumindest qualitativ durch eine kleine Anzahl von Sedimentkern-Proxy-Aufzeichnungen unterstützt wird. Allerdings fällt der sommerliche Meereisstand bereits bei unserer 124 ka-Simulation und bei allen MIS-11c-Simulationen deutlich höher aus, was darauf hindeutet, dass eisfreie Sommer in den beiden Interglazialen auf einen kurzen Zeitraum im frühen MIS-5e beschränkt gewesen sein müssen. Außerdem hängt die interannuelle Variabilität stark mit der durchschnittlichen Sommer-Meereisfläche zusammen, wobei die Variabilität sowohl bei niedrigen als auch bei hohen Meereisflächen gering ist. Die durchschnittliche Sommer-Meereisfläche weist die größte interannuelle Variabilität auf, weil es im zentralen Arktischen Ozean große Mengen an Meereis gibt, wo variable Wettermuster einen großen saisonalen Einfluss auf Prozesse wie das Schmelzen und den Export von Eis haben können. Dies deutet darauf hin, dass die größte Volatilität im arktischen Sommer-Meereisregime während der Übergangsphasen zwischen hohen und niedrigen Sommereiskonzentrationen auftritt. Dies ist die Phase, in die die Arktis aktuell einzutreten scheint.

Das verbindende Thema der in dieser Dissertation vorgestellten Studien ist, dass die Modellierung von Zwischeneiszeiten der jüngsten Vergangenheit mit Parallelen zu heute Aufschluss über die zu erwartenden Veränderungen im Klima der nahen Zukunft geben kann. Wir konnten einige Merkmale des arktischen interglazialen Klimas aufzeigen, die in sehr unterschiedlich geprägten Klimaperioden auftreten, und verbesserte Kopplungstechniken für zukünftige Paläo-Eis-Klimamodelle anbieten. Die hier vorgestellten Ergebnisse stellen einen bedeutenden Fortschritt im Verständnis des interglazialen Klimas dar und unterstützen die laufenden Bemühungen, bessere Prognosen für unser sich schnell veränderndes Klima zu erstellen.

Contents

Chapter 1

Introduction

The Pleistocene Epoch spans the last ca. 2.6 million years and has been characterized by constant oscillation between glacial and interglacial conditions. Fundamentally, glacial periods are characterized by the buildup of enormous ice sheets on land areas, predominantly in the northern hemisphere due to its higher proportion of land. As this water mass has its origins in the global oceans, corresponding drops in sea level also occur with each glacial period. Conversely, interglacials are characterized by large reductions in global land-ice volume and correspondingly higher sea levels. It was the transition from the last glacial period into the present interglacial around 20,000 to 10,000 years ago (20-10 ka) that arguably fostered the development of human civilization (e.g., Gupta, 2004).

Crucially, however, this cycle between glacial and interglacial conditions is neither metronomic nor symmetrical. Conditions favorable for the expansion or retreat of ice sheets are the result of a superposition of numerous forcing factors both internal and external to the climate system. These include several periodically varying elements of Earth's orbit, fluctuating greenhouse gas levels, and substantial feedback mechanisms such as increased albedo (the surface's ability to reflect sunlight) during periods of greater ice cover (e.g., Abe-Ouchi et al., 2013). The resulting glacial cycles are therefore only semi-regular and vary somewhat in magnitude and frequency (Hays et al., 1976). In general, glaciation is a slow process, with cycles of ice buildup in the most recent 800 kyr having a characteristic timescale of ~75-100 kyr. Deglaciation, on the other hand, is a comparatively rapid process, with typical timescales from maximum ice volume to minimum ice volume of just ~10-20 kyr.

As the influence of anthropogenic activities on present-day climate continues to increase, our climate trajectory for the near future looks to include an increasingly severe disruption to the previously observed glacial-interglacial cycles of the Pleistocene (Loutre and Berger, 2000; Ganopolski et al., 2016). While our projected future climate has no natural analogue (Yin and Berger, 2015), it is instructive to understand these previous instances of geologically abrupt warming that resulted in significant sea-level rise. The study presented in this thesis will utilize climate and ice sheet model simulations to detail the characteristics of two key interglacial periods and their effects specifically on the Greenland ice sheet (GrIS), which is thought to have been particularly affected by these prior warm periods. But first, we concern ourselves with a review of glacial climate theory, the documented characteristics of the two interglacials of interest (MIS-11 and MIS-5), and the techniques by which paleoclimate is studied.

1.1 Defining Interglacials

Physical evidence of widespread glaciations across the northern hemisphere was first documented by scientists in the 1800s (Hestmark, 2018). A unified theory suggesting a global drop in temperature and mass accumulation of ice as the origin of many remnant glaciers and other geological features first appeared in the 1830s (Agassiz, 1838), but took decades to gain widespread acceptance (Hansen, 1970). However, early glacial theory struggled to identify a clear mechanism for such globally robust temperature, ice cover, and sea level changes. Ever since, there have been increasingly refined explanations put forth for the patterns of ice buildup and retreat that have characterized the climate of the present epoch.

1.1.1 Mechanism

Fundamentally, glacial cycles arise due to the complex interaction of multiple periodically varying elements of Earth's orbital processes, known collectively as Milankovitch cycles (Milankovitch, 1941). These elements include the following:

- Orbital eccentricity: the degree of asymmetry in Earth's orbit around the Sun with respect to a perfect circle. Several components contribute to this variation, which has a dominant period of ~413 kyr but significant components centered around a mean of ~100 kyr. Eccentricity modulates both the intensity of solar radiation received in a given season and the relative length of seasons.
- Obliquity: the angle of the Earth's axial tilt varies between approximately 22.1° and 24.5° over the course of a ~41 kyr period, altering the amplitude of the seasonal cycle. From approximately 2.6 mya to 0.8 mya, the 41,000 year periodicity was the dominant period for glacial cycles (e.g., Berger and Wefer, 2003).
- Precession: the combined effects of the drift of the axial tilt of Earth and the inclination of the Earth's orbit results in a gradual shift of the timing of perihelion (Earth's closest approach to the sun) relative to the seasons. Several characteristic frequencies are encapsulated in this process, but the mean effect results in around a 23 kyr periodicity. The primary effect of a change in precession is to alter the seasonal distribution of insolation at a given latitude.

Collectively, these cycles serve to modify both the integrated annual total insolation and the seasonal distribution of insolation incident upon the Earth. This has its most significant consequences across the Northern Hemisphere middle and high latitudes, where reductions in insolation (particularly in summer) enable ice sheets to grow as snow accumulates and compacts into ice faster than it melts on an annual basis; conversely, significant increases in insolation help to trigger glacial termination events (e.g., Huybers, 2006).

Using a simple model relating insolation forcing to global ice volume, Huybers (2011) demonstrated that "precession will tend to influence the precise timing of a deglaciation within an obliquity cycle, but obliquity will more fundamentally govern the interval between glaciations." Favorable alignments of the precessional cycle with obliquity maxima may be the ultimate determining factor in whether a glacial terminates after its second or third ~40 kyr obliquity cycle, but termination consistently occurs at one of these two points during

the late Pleistocene (Huybers and Wunsch, 2005). Additional modeling support for the notion of critical insolation thresholds was contributed by Yin et al. (2021), whose Earth-system model of intermediate complexity (EMIC) simulations run continuously for the past eight glacial cycles consistently showed an abrupt drop in Atlantic Meridional Overturning Circulation (AMOC) intensity when mean NH insolation dropped below a certain threshold at the end of interglacials. This could suggest a role for insolation thresholds in both glacial inception and termination, consistent with (but far more complex than) what was originally proposed by Milankovic (1941).

As the Yin et al. (2021) study also suggests, insolation alone cannot explain the duration and timing of glacial terminations and inceptions. Indeed, feedbacks internal to the climate system and unique to the present geography of the Earth are necessary for the emergence of the approximately ~100 kyr glacial cycle of the late Pleistocene (e.g., Gildor and Tziperman, 2001; Lisiecki, 2010; Huybers, 2011; Abe-Ouchi et al., 2013). The necessity of internal climate mechanisms in fully explaining glacial cycle timing and intensity is demonstrated by the clear hysteresis behavior in northern hemisphere ice sheet volume; that is to say, when considering ice volume against either mean temperature or insolation anomalies in the Northern Hemisphere, there are at least two semi-stable equilibrium states that are dependent on the initial presence or absence of large ice volumes (Abe-Ouchi et al., 2013).

Hysteresis behavior can be partly explained by two main internal climate mechanisms, both of which contribute to the asymmetric nature of glacial cycles and help to set their duration. Most prominent are albedo changes due to varying extent of land ice, sea ice, and dust deposition (e.g., Gildor and Tziperman, 2001; Ganopolski and Calov, 2011). Alterations of carbon dioxide and other greenhouse gas levels also alter the radiative forcing balance and arise due to vegetation changes (Claussen, 2009), release from or sequestration into oceans (e.g., Sigman et al., 2010), and/or mineral weathering (e.g., Kölling et al., 2019). From these complexly interacting (and often competing) feedbacks and forcing mechanisms arises the characteristic "sawtooth" pattern of long gradual glaciations and abrupt deglaciations (Figure 1-1).

1.1.2 Defining Glacial-Interglacial Cycles

Observationally, numerous methods have been developed for the reconstruction of global temperature and precipitation during the ancient past, most notably by analyzing the ratios of oxygen isotopes contained in ice cores and marine sediment cores. These "observations" are also referred to as proxy records and refer broadly to various types of samples and analysis techniques. Additional examples include oxygen isotope ratio ($\delta^{18}O$) records from stalagmites in Chinese caves (e.g., Liu et al., 2020), silt composition and radioactive isotope analyses from lake and ocean sediment cores (e.g., Axford et al., 2013), examinations of ice-rafted detritus in marine sediments (e.g., Reyes et al., 2014), various biological markers from lake or ocean sediment deposits including ancient pollen (e.g., Willerslev et al., 2007), and even measuring the concentration of radiogenic chemical isotopes in bedrock to determine its exposure time to open sky (e.g., Bierman et al., 2014).

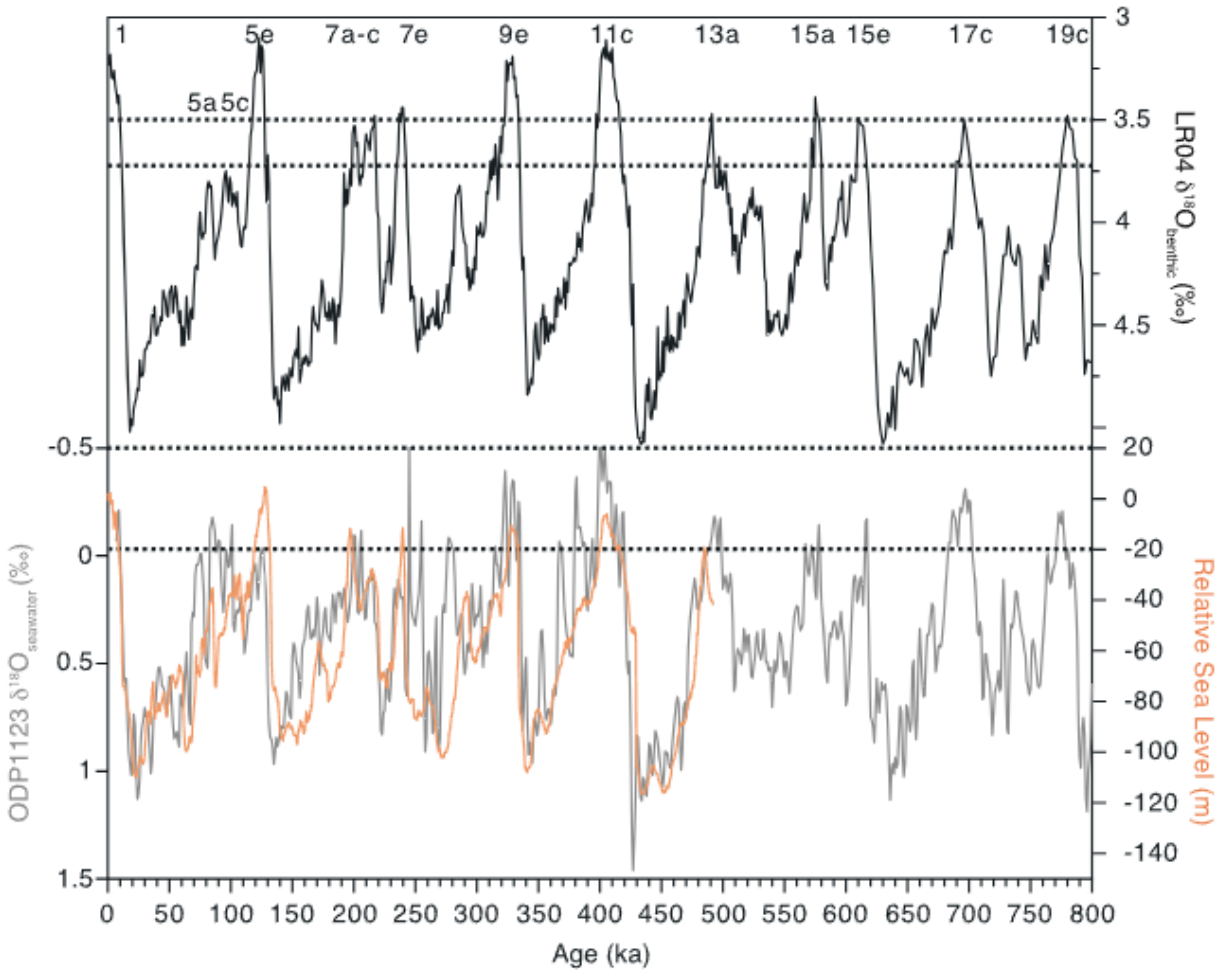

Figure 1-1. Reproduced Fig. 2 from Past Interglacials Working Group of PAGES (2016), depicting the characteristic "sawtooth" pattern of interglacial evolution. The top plot shows the Lisiecki and Raymo (2005) benthic stack, a composite record of oxygen isotope data that correlates strongly with global mean ocean temperatures. The bottom plot depicts the evolution of relative sea level in the Red Sea over the past 500 kyr (Rohling et al., 2009).

The study of marine cores in particular gave rise to the modern notation system, which originated with the seminal work of Emiliani (1955). Emiliani used periods of abrupt changes in oxygen isotopes to delineate stages, and the paleoclimate community has subsequently adopted and enhanced this system of nomenclature. The term "Marine Isotope Stages" has since come to be applied to recent geologic periods that are defined by fluctuations in the ratios of oxygen-18 and oxygen-16 isotopes present in marine sediment cores (e.g., Candy et al. 2014). Such records generally have a resolution of several thousand years and can provide valuable ocean temperature proxy data, as these ratios have a strong relationship with temperature (Milker et al., 2013; Lisiecki and Raymo, 2005).

Specifically, global temperature records are often developed from analysis of marine sediments containing deposited foraminifera microfossils. The $\delta^{18}O$ of foraminifera shells is directly related to the temperature and $\delta^{18}O$ content of the water in which they form, and the $\delta^{18}O$ of the water is in turn proportional to the water's salinity and the global ice volume (Lisiecki and Raymo, 2005). Records of $\delta^{18}O$ therefore offer a relatively globally coherent signal, and the correlation of these various records has enabled the emergence of unified "stacks" such as the heavily cited Lisiecki and Raymo "LR04" benthic stack. Such records must be assigned

an age model, however, as they contain no inherent timing information. An age model simply describes the age of the features present in the stack by calculating age based on e.g. contemporaneous ice-core records or sedimentation rates calculated as a function of orbital parameters (Lisiecki and Raymo, 2005). These records are often the best, and sometimes only, accurate method of estimating ocean temperatures for periods thousands of years ago, and are therefore particularly useful in diagnosing climate states throughout much of the Quaternary and Holocene geologic periods (~2.6 MY ago through present).

Of even more direct interest to this study is the age dating of ice core records from the Greenland and Antarctic ice sheets. Several key coring projects have been conducted in recent decades, producing ice records of various physical and temporal lengths, some spanning the entirety of the late Pleistocene period. Noteworthy is the EPICA Dome C core, which reached a depth of 3260 m and contains basal ice dating back approximately 800 kyr (EPICA Community Members, 2004; Parrenin et al., 2007; Lüthi et al., 2008). Outside of Antarctica, the longest available ice core record comes from the NGRIP site, in which the deepest ice has been dated to 123 ka (North Greenland Ice Core Project members, 2004).

Ice core dating is a complex process utilizing various techniques that must often be compared and correlated with one another to provide much meaning. Techniques include visually counting annual accumulation layers, analyzing the deuterium ratio of the ice itself, measuring the quantity and composition of gas bubbles trapped in the ice, and analyzing isotopic ratios of elements such as uranium and beryllium from dust trapped in the samples (e.g., Petit et al., 1999; Extier et al., 2018; Bazin et al., 2013). Together, these techniques can provide a continuous record of (most crucially) local temperature changes on millennial timescales, but also of changes in ice accumulation rates, overall dust loading of the atmosphere, and composition of atmospheric trace gasses. In combination with the various other forms of paleorecords mentioned previously, a scattershot picture of various overlapping snapshots of local climate from around the world can be built, thus providing at least a partial picture of ancient climate.

1.1.3 Limitations of Paleo-reconstructions

Individually, the paleo-datasets used to reconstruct past climate variations give only limited information, but intercomparison and matching variations across records enables a more complete picture to emerge. However, there are still several key assumptions and dependencies which undermine the absolute reliability of these records and necessitate the use of other approaches (such as modeling) to better understand past climates.

The most severe limitation on paleoproxies as a whole is the spatial and temporal coverage of records. While many thousands of records of various types now exist, each effectively represents just a single point and extends through a very geologically limited window in time. Ice cores provide a clear example of this: they are the very definition of a point measurement, but can provide a relatively consistent and long-duration record of climate, as in the EPICA Dome C core. However, the extremely limited spatial coverage leaves many questions as to what ice coverage may have looked like in past interglacials and when bedrock was last exposed (e.g., Schaefer et al., 2016; Bierman et al., 2016; Briner et al., 2022). The Briner et al. (2022) study identifies

future high-priority sites of interest for drilling additional ice cores, but the length and expense of such projects means that acquiring such additional data is likely to be decades away.

As another example, Milker et al. (2013) examine a wide array of sea-surface temperature proxy records focusing on the Marine Isotope Stage 11 period (ca. 424-374 ka), combining 78 different records from 57 different sites. This represents a large fraction of all sea-surface temperature records available for this period to date, and yet spatial coverage is very limited in, e.g., the central and western Atlantic, the north Pacific, the Indian, and the Arctic Oceans. The estimated temporal resolution of the various records ranges from as high as 300 years to as low as over 15 kyr, and thus these records cannot effectively resolve millennial-scale temporal variability (Milker et al., 2013).

Such studies highlight an additional limitation of many paleorecords: the need to "tune" or correlate the time series to another well-dated dataset in order to have confidence in the record's temporal development. The already-mentioned LR04 benthic stack record utilizes age control points related to orbital obliquity and precession in 21 June insolation at 65°N, thus artificially tying parts of the sediment isotope record to a pre-calculated orbital model (Lisiecki and Raymo, 2005). Other comparable records are then in turn tuned to the LR04 stack, such as those examined by Milker et al. (2013), introducing the possibility of compounding temporal biases.

Given the considerable uncertainties, it is no surprise that oftentimes competing interpretations of the same or very similar records often emerge. For instance, ^{26}Al and ^{10}Be concentrations in bedrock samples from the GISP2 ice core have been interpreted as evidence of both a very static and stable eastern GrIS in the past 1 million years (Bierman et al., 2016) and of an eastern GrIS that is likely to have been susceptible to periodic retreat during interglacial peaks (Schaefer et al., 2016). Climate models are therefore an extraordinarily useful tool for conducting plausibility checks on varying hypotheses and "filling in the gaps" of spatially and temporally limited datasets. The role of models will be discussed more specifically in 1.3, after a brief introduction to the two most important interglacial periods for this study.

1.2 Key Interglacials

In the latter part of the Pleistocene, glacial-interglacial cycles became more intense, with ice volume changes (and corresponding sea level changes) becoming substantially greater. This transition is known as the mid-Brunhes shift, and it occurred at the end of the Marine Isotope Stage 11 (MIS-11) glacial period around 430 ka (EPICA Community Members, 2004; Jouzel et al., 2007).

It is during this period of more dramatic glacial cycles that we find our present interglacial climate as well as a handful of other broadly similar interglacial periods. In particular, the interglacial periods designated as MIS-11c and MIS-5e are suggested by various lines of evidence to have had global mean temperatures at or above those of the present-day climate. Correspondingly, reductions in the volume of the Greenland and/or Antarctic

ice sheets relative to their present sizes are thought to have occurred, resulting in sea level increases above present-day levels of a magnitude that would have far-reaching consequences if repeated today.

1.2.1 MIS-11c Interglacial

MIS-11c corresponds to the warm period beginning with Glacial Termination V at around 425,000 years before present and ending during substantial re-glaciation around 390 ka (e.g., Jouzel et al., 2007; Milker et al., 2013; Tzedakis et al., 2022). The significance of this period is related to three of its key characteristics:

- the unusual duration of interglacial/warm conditions;
- the general similarity of Earth's orbital configuration to that of our present interglacial (the Holocene);
- and the high likelihood that the GrIS at its minimum reached at least 50-80% lower in volume than today (Reyes et al., 2014; Dutton et al., 2015).

Due to the similarities in the amplitude of eccentricity and obliquity to present conditions, MIS-11 has been proposed as a potential analogue for the Holocene (e.g. Loutre and Berger, 2000; Alley et al., 2010; Candy et al., 2013; Yin and Berger, 2015). Slightly higher natural greenhouse gas concentrations and a different seasonal pattern of insolation are primarily what differentiate MIS-11c and the present interglacial (Yin and Berger, 2012). Comparison of the LR04 benthic stack temperature proxy record (Lisiecki and Raymo, 2005) also shows very similar evolution of global ocean temperatures and sea levels between ca. 440-410 ka and 30-0 ka (Raymo and Mitrovica, 2012). Additionally, global temperatures, while somewhat poorly constrained, are thought to have been only modestly warmer than preindustrial temperatures at their highest, though with regional Arctic and subarctic temperature anomalies in the range of 2-4°C above present (e.g., Melles et al., 2012; Coletti et al., 2015).

Various lines of evidence have converged to suggest that the warmest temperatures during the MIS-11 period occurred around 415-405 kya (e.g., Raymo and Mitrovica, 2012; Cronin et al., 2019). Maximum boreal summer temperature anomalies around Greenland have been modeled at around 3°C and are estimated to have been warmer than today's summer temperatures for around 12-17 kyr (Robinson et al., 2017). This extended period of warmth is believed to have been sufficient to enable not only the dramatic retreat of the GrIS (Raymo and Mitrovica, 2012; Reyes et al., 2014; Christ et al., 2023), but the growth of boreal forest in portions of southern Greenland, as evidenced by the presence of pollen and insect DNA in some ocean sediment cores located on the southern fringes of the continental shelf (Willerslev et al., 2007; de Vernal and Hillaire-Marcel, 2008). Such a stark departure in the regional climate has been ascribed in part to higher summer insolation than present-day conditions, but with a significant contribution from stronger poleward heat transport via the Atlantic Meridional Overturning Circulation (AMOC; Rachmayani et al., 2017). The degree to which other internal climate mechanisms may have enhanced or sustained warm temperature anomalies during the interglacial period remains an open question.

Consequently, the global sea level highstand is estimated to have been around 6-13 meters higher than the sea level of today (Dutton et al., 2015). Much of this rise can be attributed to the melt of the GrIS, which is

simulated to have contributed approximately 6.1 meters of sea-level equivalent (95% confidence interval 3.9-7.0 m) during this time period (Robinson et al., 2017). Given that the entirety of the GrIS is believed to contain approximately 7.4 m of sea-level equivalent (Morlighem et al., 2017), this constitutes a near-disappearance of the ice sheet during MIS-11c, with only the highest elevations thought to have retained significant ice cover. Such a level of melt is supported by the limited geological evidence, with the Camp Century (Christ et al., 2023) and DYE-3 (Yau et al., 2016a, 2016b) ice core locations likely completely deglaciated during this time. Achieving such a level of melt was apparently highly dependent on the unusual duration of warmth in MIS-11 rather than the intensity of the insolation forcing, which was relatively modest for an interglacial (e.g., Robinson et al., 2017; Rachmayani et al., 2017).

The unusual duration of interglacial warmth during MIS-11 naturally gives rise to questions about the climate state that sustained such conditions. While Milker et al. (2013) suggest that the close relationship between SST proxy records and modeled SSTs supports the notion that orbital forcing was the dominant driver during this period, other studies suggest that the summer temperatures achieved over Greenland cannot be explained by insolation changes alone (e.g., Rachmayani et al., 2017). Parsing out the role of internal climate mechanisms in forcing the melt of the GrIS will therefore be crucial to improving understanding of the climate in this period in geologic history (Capron et al., 2019).

1.2.2 MIS-5e Interglacial

Of all the paleoclimatic eras that have been studied, perhaps none has enjoyed so much attention as the interglacial known as Marine Isotope Stage 5e (also known as LIG, the Last Interglacial). Its relative recency in geologic terms and status as the interglacial period most immediately preceding the present day means that the relative availability of paleoproxy records is far higher than for older periods. This availability of proxies for comparison also makes it an appealing target for paleoclimate modelers seeking to understand interglacial characteristics or variety. This section will focus on an overview of the climatic characteristics of MIS-5e as established by paleodata records and modeling studies, with a particular emphasis on Greenland and the Arctic region.

The favorable alignment of precession with high obliquity and large eccentricity during the LIG resulted in significantly higher boreal summer insolation across the Northern Hemisphere, particularly around 130-125 ka (Otto-Bliesner et al., 2013; Bartlein and Schaefer, 2019). High-latitude boreal summers were therefore substantially warmer than present day, but negative winter insolation anomalies at least partially offset this and resulted in a broadly similar global annual mean temperature (e.g., Melles et al., 2012; Otto-Bliesner et al., 2013; Coletti et al., 2015). These “intensified” northern summers ensured that conditions favorable for the melt of the GrIS and rising global sea levels were present, with sea levels believed to be above present-day from approximately 129 ka to 116 ka (e.g., Lisiecki and Raymo, 2005; Dutton et al., 2015). However, difficulties remain in assessing the exact timing and magnitude of the sea-level highstand, which may have occurred in multiple phases or oscillated several times (e.g., Hearty et al., 2007), making it difficult to assess individual contributions from GrIS or Antarctica.

Numerous coupled ice-climate modeling studies have sought to bound the likely contribution from the GrIS to the LIG sea level, with initially widely scattered estimates that have started to converge in more recent years. Tarasov and Peltier (2003) constrained climate inputs to their simulation to largely match temperatures from ice cores and found a broad 2.0 to 5.2 m likely contribution range from Greenland. Similarly, an ensemble of coupled simulations filtered by matching temperatures with the NEEM and GISP2 ice core records indicate a potentially large sea level contribution of 4.1 to 6.2 m (Yau et al., 2016a). Somewhat lesser contributions of 2.2 to 3.4 m (Otto-Bliesner et al., 2006), 0.6 to 3.5 m (Stone et al., 2013), 1.2 to 3.5 m (Helsen et al., 2013), ca. 1.4 m (Goelzer et al., 2016), and ca. 3.0 m (Sommers et al., 2021) were suggested by studies that used more sophisticated models, but did not apply such data-based constraints to their inputs. The extent of Greenland deglaciation during the LIG thus remains an open question.

Luckily, multiple well-dated and continuous ice core records from several sites across the GrIS help to constrain the possible evolution of the GrIS during the LIG. Isotopic analysis from multiple ice-core sites across Greenland point to probable air temperature anomalies relative to today of several degrees, including 8 +/- 4°C in northeastern Greenland (e.g., CAPE-Last Interglacial Project Members, 2006; NEEM Community members, 2013). High confidence exists in continuous ice cover around the Summit region of Greenland through the LIG (Raynaud et al., 1997; NorthGRIP, 2004), with ice likely also remaining at DYE-3 (Yau et al., 2016b). However, forcing the input temperatures of climate simulations to match the temperatures recorded in ice cores often results in the simulated disappearance of ice at sites such as DYE-3 and NEEM, giving rise to something of a paradox (Goelzer et al., 2016).

The degree to which the GrIS retreated during the LIG has important implications not only for the sea-level rise contribution it made during this period, but also for the climatic impacts resulting from partial loss of the ice sheet, including not just local but potentially Arctic-wide temperature increases (e.g., Melles et al., 2012; Merz et al., 2014). AOGCM simulations that do not allow for dynamic vegetation and ice-sheet changes suggest substantially lesser warming than seen in proxy records, though the set of proxies examined is biased towards the northern high latitudes (Otto-Bliesner et al., 2013). Boreal summer air temperature proxies are also indicative of a steep (and perhaps near-total) loss of summer sea ice in the Arctic, though a large spread exists among PMIP4 model simulation members (Sime et al., 2023).

1.3 Modeling of Past Interglacials and Ice Sheets

With the severe limitations in paleodata (described in 1.1.3), climate and ice models naturally constitute the next-best of understanding the climate from the ancient past. Several categories of models with varying degrees of sophistication have been used in the past to simulate climate, with more sophisticated fully coupled models becoming more common in recent years as the availability of supercomputing power increases. In this discussion, particular focus is given to prior studies that utilized atmosphere-ocean general circulation models (AOGCMs), or the most sophisticated and computationally expensive class of models, as we have chosen to use one such model (CESM) for our studies.

1.3.1 PMIP Project

The Paleoclimate Model Intercomparison Project (PMIP) is a long-running research protocol and data-sharing initiative related to the Climate Model Intercomparison Projects (CMIPs) that grew out of the Intergovernmental Panel on Climate Change (IPCC) assessment reports. The original PMIP project began in the 1990s with guidelines on how to conduct Holocene Climate Optimum (ca. 6 ka) and Last Glacial Maximum (LGM; ca. 21 ka) experiments (Joussaume and Taylor, 1995). These initial experiments were necessarily highly simplified, utilizing e.g. fixed modern-day sea surface temperatures and prescribed ice sheets, but established such still-utilized and ubiquitous paleoclimate modeling principles as the alteration of orbital and greenhouse gas parameters to set standards for modeling of specific periods (Joussaume et al., 1999).

Advances in model sophistication and available computing power in the years that followed led to a proliferation of dynamic ocean and vegetation models which could be interactively coupled to the atmospheric models already widely in use. Thus, PMIP2 incorporated explicit comparisons between model generations and the multi-system climate feedbacks as simulated by these coupled models (Crucifix et al., 2005). In particular, they demonstrated that the explicit coupled simulation of ocean surface temperatures resulted in notably cooler global temperatures during the LGM, particularly in the tropics (Braconnot et al., 2007a).

Directly relevant for the studies in this dissertation are their conclusions that: (1) explicit simulation of ocean temperatures results in robust African monsoon enhancements during precession minima (such as at 6 ka) and (2) explicit treatment of sea ice amplifies the seasonal temperature cycle in the northern high latitudes (Braconnot et al., 2007a). A follow-up PMIP2 comparison study estimated that sea ice- and snow cover-driven albedo changes were responsible for approximately 50% of Northern Hemisphere cooling at LGM, indicating the significance of accurately simulating the seasonal sea ice cycle (Braconnot et al., 2007b).

The third and fourth generations of the PMIP project expanded the focus to include not only the 850-1850 CE millennium, but also past warm periods in the form of the Last Interglacial (LIG; also MIS-5e) and the mid-Pliocene (ca. 3.2 million years ago). The Last Millennium simulations enable better understanding of recent climate variability and climatic changes that have already occurred since the preindustrial era (Braconnot et al., 2012). The inclusion of the MIS-5e simulations (127 ka conditions) provided standardized guidelines for one of the time-slice simulations utilized in this study and a framework by which our results can be directly compared with numerous other studies.

The goals of evaluating and comparing simulations under 127 ka conditions include improved understanding of how specific forcing mechanisms affect climate (e.g., GHG changes vs. orbital forcing), evaluating how well models simulate warmer climatic eras by comparing with paleoclimate data, and exploring interactions between changing ice sheets, the oceans, and the atmosphere (Braconnot et al., 2012; Otto-Bliesner et al., 2017). Of particular interest for the studies in this dissertation are those that also simulate dynamically evolving

ice sheets or can be run in conjunction with ice sheet models, for which there are numerous methodological approaches.

1.3.2 Coupled Climate-Ice Sheet Modeling

Dynamic ice sheets as interactive components of fully coupled climate models are a somewhat recent development, due primarily to high ice-dynamic process uncertainty and the complexity of ice-climate interactions (Vizcaíno, 2014). These numerous uncertainties are typically reduced to parameterizations in ice sheet models, which lend them to tuning, sensitivity testing, or the use of ensembles (e.g., Ritz et al., 1996; Hebeler et al., 2008; Stone et al., 2010). The need for computational efficiency to explore the many permutations of these complex parameter spaces has resulted in the predominant use of EMICs for joint climate-ice modeling studies.

Earth-system models of intermediate complexity are fundamentally streamlined models of interacting geophysical systems, operating at lower spatial and temporal resolutions in order to achieve computational efficiency (Claussen et al., 2002). However, because of this efficiency, they sometimes include sophisticated components historically lacking in complex AOGCMs, such as biogeochemistry and glacial isostatic adjustment (e.g., Tarasov and Peltier, 1997; Claussen et al., 2002; Goosse et al., 2010). Some EMICs in widespread use for coupled ice-climate studies, particularly in the paleoclimate sphere, include CLIMBER (Petoukhov et al., 2000; Montoya et al., 2005), LOVECLIM (Driesschaert et al., 2007; Goosse et al., 2010), and the UVic Earth System Climate Model (Weaver et al., 2001). Each of these models to varying degrees utilize parameterizations of e.g., atmospheric and oceanic processes to enable simulation of global climate evolution over very long periods of time and/or run many interactions of the same period of interest (i.e., glacial cycles; examples include Ganopolski and Calov, 2011; Goelzer et al., 2016; Yin et al., 2021).

In such parametrically complex systems, ensembles containing numerous members are a key tool for developing meaningful results. Each member of an ensemble consists of the same coupled model system, but with one or more varied parameters. The most common use-case for this technique is defining a range of plausible outcomes where paleodata or other verification sources are less prevalent, i.e. during past interglacials (numerous examples, but see e.g., Tarasov and Peltier, 2004; Applegate et al., 2012; Robinson et al., 2017). Coupled ice-climate model ensembles can also be used to evaluate the likely ranges of particular parameters in cases of process uncertainty, such as with ice sliding (e.g., Albrecht et al., 2020), or to examine numerous scenarios, such as the effects of various future CO2 emission trajectories on ice sheet melt (e.g., Huybrechts and Wolde, 1999; Stone et al., 2010; Aschwanden et al., 2019).

While the simplicity of EMICs allows for exploration of uncertainties in the climate forcing space via climate model parameterizations or simulation of multiple scenarios, coupled ice-climate modeling of ancient climates is also increasingly possible with full AOGCMs. The simplest way to accomplish this is by maintaining a fixed ice sheet in the AOGCM, which has the disadvantage of neglecting the climate feedbacks that would in reality occur as a result of, e.g., altering surface topography and albedo (e.g., Otto-Bliesner et al., 2006; Born and

Nisancioglu, 2012; Stone et al., 2013). Despite the missing interactivity with the ice sheets, the computational demands of a full AOGCM usually mean that transient simulations of long time periods are impractical, though "acceleration" of the timescale over which forcing evolves and/or relatively low spatial resolutions are possible compensating options (e.g., Smith and Gregory, 2012; Varma et al., 2016).

Alternatively, the complex AOGCM can be used to model shorter "snapshots" of past climate states in finer detail. While not used in conjunction with ice sheet models, the climate at peak astronomical forcing conditions of all recent interglacials ranging from MIS-1 to MIS-19 were compared using CCSM3 in Herold et al. (2012) and Rachmayani et al. (2016). Similar experiments using peak MIS-5e and MIS-11c forcings from CCSM3 one-way coupled to the GLIMMER ice sheet model demonstrated the advantages of using such models: despite stronger astronomical forcing in MIS-5e than MIS-11c, the experiments realistically produced greater GrIS melt in MIS-11c due to enhanced poleward oceanic heat flux (Rachmayani et al., 2017). Such a result may not have been possible in coupled EMIC simulations, which often rely on slab-ocean or greatly simplified ocean models.

By strategically choosing several such time slices spanning an interglacial period, as Stone et al. (2013) did by modeling MIS-5e at 130, 125, and 120 ka and interpolating between, the climate forcing for a far longer period can be generally captured. This "time slice" methodology will be revisited to examine several aspects of the MIS-5e and MIS-11c interglacial climates in the results chapters of this dissertation.

1.3.3 Limitations and Uncertainties

Any of the coupled ice-climate model systems described in the previous section will be subject to a number of limitations, particularly with regards to how information is exchanged between the modules comprising the model or coupled setups. One particularly prominent such example is the communication of surface air temperatures from climate models to the ice surface as represented in the coupled ice-sheet model. Depending on the exact model configuration, the surface temperatures given could be at a different elevation than the ice surface due to, for example, differences in model resolution or the climate model utilizing fixed ice sheets. This necessitates implementing a downscaling or correction factor to the temperature for it to be representative of the actual surface elevation. Many such techniques exist to achieve this, including:

- utilizing a higher-resolution regional climate model as an intermediary, known as dynamical downscaling (e.g., Goelzer et al., 2017);
- utilizing fixed or parametric scalar lapse rate values (e.g., Huybrechts and T'siobbel, 1997; Otto-Bliesner, 2006; Vizcaíno et al., 2008; Stone et al., 2010);
- utilizing monthly or seasonally varying lapse rates for correction (Erokhina et al., 2017) or, as will be fully explored in Chapter 4 of this dissertation, more sophisticated spatially and temporally varying schemes;
- or most ideally, fully two-way coupled simulations at sufficient resolution to resolve critical features such as outlet glaciers and regions of steep ice margins. Such simulations remain impractical due to the extreme computational expense.

Of course, surface temperatures are but one of the critical variables that need to be communicated between interacting ice sheet and climate models. The other major component of surface mass balance for an ice sheet is the type and amount of precipitation, whose classification is often done on the basis of surface air temperature (e.g., Fitzgerald et al., 2012). Treatment of liquid precipitation over ice sheets can also vary widely, from the rather crude assumption of instantaneous runoff (e.g., Kirchner et al., 2011; Quiquet et al., 2012) to sophisticated but still parameterized porous transport and refreezing schemes (e.g., Reijmer et al., 2012; Steger et al., 2017). Additionally, precipitation downscaling often does not directly account for orographic effects, even if a simple accommodation of elevation-based differences is included (e.g., Sellevold et al., 2019). A more advanced wind-based orographic adjustment scheme is implemented in the Glacial Systems Model (Bahadory and Tarasov, 2018), but even this relies on a more simplistic relationship between modeled winds and precipitation than actually exists.

The integrated effects of temperature and precipitation together are often summarized in a surface mass balance (SMB) scheme. Coupled model systems have often utilized SMB schemes of various complexity and incorporating various components, but discussion here will be particularly concerned with melt schema. These can span simple functions of accumulated positive degree day schemes (surface temperatures greater than 0°C, also known as PDD; Reeh, 1991) to insolation-integrated PDD schemes (Tarasov and Peltier, 2002; Fitzgerald et al., 2012; Tarasov et al., in prep.) to elevation-class downscaling (Sellevold et al., 2019) to integrated energy-moisture balance models such as REMBO (Robinson et al., 2010; Calov et al., 2015). Each such scheme comes with its own compromises; for example, PDDs are generally naive to varying insolation and REMBO assumes fixed vertical profiles for temperature and humidity changes (Robinson et al., 2010). Significant room for improvement therefore remains with regards to minimizing uncertainty in coupled ice- and climate-model systems.

Limitations for ice-climate modeling extend beyond the coupling between model systems and into internal mechanisms of the ice model itself. The use of ensembles to explore the potential parameter space for a given ice model was already touched on in the previous section, but the presence of numerous parameterizations in ice models is fundamentally due to significant process uncertainty (e.g., Marshall, 2005). For instance, not yet fully understood and sub-grid scale processes govern the grounding line location and movement of marine-terminating glaciers, therefore requiring various forms of parameterization. Fürst et al. (2015) artificially enhanced basal sliding of marine glaciers as temperature increased to simulate frontal ablation. Others opt for a more sophisticated plume model, accounting not only for ocean water temperatures, but also factors such as local geometry and subglacial discharge (e.g., Beckmann et al., 2019).

A further very prominent example is the continued necessity of enhancement factors as part of modified Glen's flow law equations in modern 3D thermomechanical ice sheet models. These are essentially "fudge factor" scalars used to multiply the deviatoric stresses acting on the ice in order to produce results nearer to observations. Typically, grounded sections of ice sheets have higher velocities than modeled and floating ice

shelves have their velocities overestimated (Ma et al., 2010). Therefore, two separate enhancement factors for the two cases are employed (e.g. Huybrechts, 1990), resulting in tunable parameters being included in the fundamental physics equations of even state-of-the-art ice models.

A final major hurdle for studies seeking to model paleo-ice sheets is the problem of initialization. For present-day and near-future simulations, a spin-up ensemble conducted over the most recent one or two glacial cycles can be performed (e.g., Aschwanden et al., 2013; Bindschadler et al., 2013) and filtered using various observational criteria to arrive at a reasonable approximation of today's ice sheets (e.g., Tarasov et al., in prep.). However, past constraints are often limited to overall sea-level estimates (Lisiecko and Raymo, 2005), the presence or absence of ice at a given time where an ice core sample was taken (e.g., Bierman et al. 2014; Yau et al., 2016b; Bierman et al., 2016; Schaefer et al., 2016; Christ et al., 2023), or indirect cues such as from sedimentation (e.g., Reyes et al., 2014). Given that modeled ice sheets can be quite sensitive to variables like bed topography (Hebeler et al., 2008) and initial thermal states (Rogozhina et al., 2011), the fundamental unknowability of these boundary conditions introduces significant uncertainty.

1.3.4 Modeling GrIS Melt in Recent Interglacials

Of particular interest for the studies conducted as part of this dissertation are how coupled ice-climate models have been specifically used to estimate melt of the Greenland ice sheet in previous interglacials. The first challenge with such simulations is, as mentioned in the previous section, developing an appropriate initialization state, as this can be particularly impactful to the final simulated result (e.g., Stone et al., 2010; Rogozhina et al., 2011; Sommers et al., 2021). Recent Greenland-centric studies have favored the "paleo spin-up" option to allow relative equilibrium between the climate forcing, the ice sheet geometry, and the ice thermal state, when possible conducted over one or more full glacial cycles (e.g., Robinson et al., 2010; Calov et al., 2015; Fürst et al., 2015; Robinson et al., 2017). This provides an internally consistent initial state for further simulation.

Coupled modeling studies involving the paleo-Greenland ice sheet have overwhelmingly targeted the Last Interglacial (LIG)/MIS-5e, due to its geologic recency and the related availability of paleoproxy data for constraints and validation. These studies have however yielded some useful and presumably generalizable conclusions about the melt behavior of the GrIS during warm interglacials. As one example, the steep elevation gradients around the margin of the Greenland ice sheet are thought to make it particularly susceptible to model biases in surface air temperature. A simple coupled EMIC setup was used to demonstrate that without accounting for surface air temperature biases, the GrIS volume of the Eemian could be more than 60% larger than the control simulation, a much bigger deviation than failing to account for refreezing or the ice-albedo feedback (Fyke et al., 2011).

Similarly, the GrIS demonstrates strong sensitivity to the elevation feedback, in which ice retreat accelerates with a lowering ice surface (which in turn produces higher surface air temperatures) in warmer-than-present conditions (e.g., Otto-Bliesner et al., 2006). A sophisticated fully-transient AOGCM-ice sheet simulation

produced approximately similar sea-level contributions from the GrIS during MIS-5e (3.4 m from Otto-Bliesner et al., 2006, 3.0 m from Sommers et al., 2021), but also demonstrated that even a severely reduced GrIS would regrow when temperatures dropped below approximately modern levels. Furthermore, explicitly modeling vegetation and allowing it to evolve with other climatic changes is necessary to achieve better concurrence with paleoproxy data, and failing to include dynamic vegetation in the simulation results in much less MIS-5e ice melt (Sommers et al., 2021).

Furthermore, underlying climatic subtleties that distinguish the interglacials can have a substantial impact on the modeled GrIS melt response. Rachmayani et al. (2017) found that CCSM3 simulations forced only with orbital and greenhouse gas characteristics for 125 ka (MIS-5e) and 410 ka (MIS-11c) do in fact produce more surface ablation and total melt for the GrIS in MIS-11c, despite higher summer insolation in MIS-5e. This is primarily ascribed to a strengthened AMOC in MIS-11c that arises out of feedbacks unrelated to Greenland, but also due to the small additional greenhouse gas radiative forcing of 0.25 W m^{-2} and the slight relative annual mean insolation forcing of +0.4 W m^{-2} (Rachmayani et al., 2017). However, this study used only one climate snapshot per interglacial, and the results may therefore be different if different time slices are chosen or if the meltwater from Greenland was being routed into the ocean model, potentially counteracting the other feedbacks and even weakening the AMOC as in Otto-Bliesner et al. (2006).

Ultimately, constraining the possible range of sea-level rise contributions from the GrIS during these past interglacials is a key goal, as this can also contribute to better predictions for near-future sea-level rise. Simulations attempting to reproduce a modern-day GrIS or Antarctic ice sheet configuration have a wealth of observational data for verification, but typical paleodata constraints are often anchored to analyses of ice cores. By constraining climate forcing to more closely fit the available ice-core data, Tarasov and Peltier (2003) were able to broadly estimate the range of sea-level contribution from the GrIS in the MIS-5e interglacial at 2.0 to 5.2 m. Though the available paleodata constraints are much more limited for the MIS-11c interglacial as for MIS-5e, Robinson et al. (2017) were able to apply a broadly similar methodology to a large EMIC-ice sheet model ensemble, filtering member simulations on the basis of ice core constraints. The filtered ensemble suggests mean summer temperatures around Greenland peaked around 2.8°C warmer than present and that the GrIS likely contributed 3.9 to 7.0 m of sea-level rise during MIS-11c (Robinson et al., 2017). To date, this remains the only prominent transient coupled modeling study reconstructing the GrIS in MIS-11c, providing an important inspiration for some of the work contained in this dissertation.

1.4 Key Research Questions

Fundamentally, the multi-faceted studies that comprise this dissertation concern themselves with the following key questions:

1. Did atmospheric feedbacks contribute to increasing the vulnerability of the Greenland ice sheet to melt during the MIS-11c interglacial? If so, what climatic mechanisms may have been involved? Additionally, how might atmospheric feedbacks during the MIS-11c interglacial have acted to help sustain its warmth for such an anomalously long time period?

2. To what extent can modeled Greenland ice sheet retreat during MIS-11c be reconciled with the limited available paleo-reconstructions? Given the highly uncertain reconstructions, how do modeling methodologies impact simulated melt extent?
3. How did Arctic sea ice and the Northern Hemisphere atmospheric circulation respond to the very different forcing conditions of the MIS-5e and MIS-11c interglacials? How might these differences have contributed to or influenced the differences in GrIS melt between the two eras?

In essence, all of these questions strive towards resolving the ongoing apparent contradiction that a greater portion of the GrIS appeared to have melted during MIS-11c, which was more weakly forced and overall cooler than MIS-5e. Exploring potentially related atmospheric and sea ice characteristics through time slice simulations of these periods provides insights into the feedback mechanisms that contributed to and sustained the warmth of MIS-11c. This ultimately contributes to understanding what critical feedback mechanisms will play a role in the melt of the GrIS in the present and near future.

1.5 Overview of Own Research

The research described in this manuscript was born of a project conceived by Matthias Prange and Michael Schulz of MARUM and the University of Bremen, who then served as advisors for the project. Additional project guidance and feedback was contributed by Lev Tarasov of Memorial University of Newfoundland, Canada, particularly for issues relating to ice-sheet modeling. He also served as the outside advisory committee member for this doctoral work.

This dissertation consists of three manuscripts, two of which have completed journal publication at the time of writing. What follows are brief descriptions of each, along with descriptions of all contributions made by others. Since their names appear frequently, Matthias Prange will be henceforth abbreviated as MP, Michael Schulz as MS, and Lev Tarasov as LT. Unless otherwise noted, all analysis of model simulations, writing of manuscripts and dissertation contents, and creation of figures was carried out by Brian Crow (henceforth BC).

Manuscript 1 (Chapter 3)

Dynamic boreal summer atmospheric circulation response as negative feedback to Greenland melt during the MIS-11 interglacial, by Brian R. Crow, Matthias Prange, and Michael Schulz, published in Climate of the Past on 12 April 2022.

Summary:

In this paper, time-slice CESM simulations of the MIS-11c interglacial are used to investigate what role atmospheric feedbacks may have played in boosting the melt of the Greenland ice sheet during this time. The simulations indicate that boreal summers were particularly warm around Greenland and the surrounding North Atlantic Ocean, with temperatures near or above present-day levels for around 20 kyr. Additionally, the North African monsoon was considerably enhanced, and these two factors contributed to a statistically significant weakening of upper-atmospheric winds over the North Atlantic. The primary jet regime also shifted to

resemble that of a single unified jet stream rather than a split polar/subtropical jet, which more closely resembles the pattern thought to dominate glacial periods rather than interglacials. The end result is actually reduced lower-tropospheric eddy heat fluxes over Greenland and the surrounding areas, implying that warming in this region is actually somewhat counteracted by a negative atmospheric feedback during MIS-11. This result is contrary to the initial hypothesis and contributes further support to the idea that MIS-11c was an unusual interglacial.

Contributions:

The research questions investigated were developed in consultation with MP and MS. Access to the HLRN supercomputing system on which the CESM simulations were conducted was gained with assistance from MP, MS, Andreas Manschke of the University of Bremen, and Lars Nerger of the Alfred Wegener Institute. The methodology for the simulations was developed in collaboration with MP and results were extensively discussed with MP and MS. LT and postdoc Heather Andres also provided inspiration and helpful discussion of results related to jet behavior, something they had similarly published on (Andres and Tarasov, 2019). Additional contributions to the final manuscript were made by an anonymous reviewer, Alexander Robinson (reviewer who identified himself and contributed time-series data for Fig. 1), and editor Quizhen Yin (who also contributed data for Fig. 1).

Manuscript 2 (Chapter 4)

Uncertainties originating from GCM downscaling and bias correction with application to the MIS-11c Greenland Ice Sheet, by Brian R. Crow, Lev Tarasov, Michael Schulz, and Matthias Prange, published in Climate of the Past on 6 February 2024.

Summary:

The uncertainties inherent in reconstructed paleo-ice sheets often necessitate the use of ice-sheet model ensembles, something which on a practical basis rules out two-way coupling with AOGCMs. We therefore sought to address the often-neglected questions of how best to downscale temperature and precipitation from a relatively coarse AOGCM grid to a higher-resolution (and very spatially sensitive) ice-sheet model grid. In particular, the change in air temperature with elevation (lapse rate) is often assumed constant in simulations, but this leads to severe underestimation of GrIS melt in our simulations of the MIS-11c interglacial. Several alternatives are therefore tested, the best of which consists of a fully spatially and temporally varying lapse rate, calculated based on the actual model temperatures at a monthly and per-grid point basis. This much more realistically captures the considerable spatial and temporal variance of air temperature changes over Greenland and leads to ice sheet melt that matches paleodata constraints much more successfully.

Contributions:

The research questions investigated in this manuscript and the methodologies used were defined in consultation primarily with LT, but with significant additional contributions from MP. After BC prepared input data for the GSM (ice-sheet model) from CESM outputs, LT set up and executed all GSM ensemble simulations. BC

conducted all analysis on the outputs of the GSM simulations. The ice-model simulations and some of the analysis were also carried out on computing resources furnished by the Digital Research Alliance of Canada/ACENET. Present-day CESM simulation data were provided by Ute Merkel of the University of Bremen Geosystems Modeling group. The manuscript was written by BC, but with extensive comments and feedback from all authors. Minor but helpful improvements to the final manuscript were contributed by two anonymous reviewers and editor Marisa Montoya.

Manuscript 3 (Chapter 5)

Arctic sea-ice cover during the Last Interglacial and MIS-11c: Long-term and short-term variability, by Brian R. Crow and Matthias Prange, in preparation for publication.

Summary:

Considerable paleoproxy and modeling evidence exists that the early, high-insolation stages of the MIS-5e interglacial were characterized by ice-free summers in most or all of the Arctic. This therefore makes this period a potential analogue for the near-future state of the Arctic, which is expected to become seasonally ice-free within the 21st century. A comparison of CESM simulations of both the MIS-5e and MIS-11c interglacials indicates that summer sea ice levels have a strong inverse relationship with the integrated summer energy, a metric that captures both the duration and intensity of NH summers rather than simply the high-latitude insolation maximum. ISE is at its highest during our 127 ka simulation (early MIS-5e) and corresponds to the narrow window of time in which both our simulation and a limited set of sea-ice paleoproxy data indicate that seasonally ice-free conditions were possible in the high Arctic. Summer sea-ice reductions were not as drastic during the lower ISE of the MIS-11c simulations, but remained at or below preindustrial levels for over 15 kyr. Analyses of the interannual variability of summer sea ice also revealed multiple interesting patterns. Sea-ice variability is maximized at intermediate levels of ice, with both very low and very high September ice areas being geographically constrained. As our modern Arctic approaches these intermediate sea-ice summers in the next decade or two, understanding the volatility of these transitionary sea-ice regimes will be of tremendous importance.

Contributions:

The research questions were developed in consultation with MP, who also provided extensive editorial input on writing and feedback on results and figures. All analysis and figure creation was carried out by BC.

Chapter 2

Methods and Data

The studies that comprised this dissertation were based on detailed analysis of a number of paleoclimate simulations, some of which were additionally coupled to an ice model offline. The details of both model configurations will be divulged here, and the process by which the offline coupling was accomplished will be described in extensive detail.

2.1 Climate Model

The climate model chosen for this study is the Community Earth System Model (CESM) v1.2.2, a fully-coupled atmosphere-ocean general circulation model (AOGCM) developed primarily by the National Corporation for Atmospheric Research (NCAR) in the United States (Hurrell et al., 2013).

There are several benefits to using CESM. Firstly, the model is freely available to the public and extensively documented. Secondly, other researchers have already made use of CESM on the HLRN supercomputer system (formally the Norddeutscher Verbund für Hoch- und Höchstleistungsrechnen, or "North German Supercomputing Alliance"). This includes the processes associated with porting the model, including finding a compatible compiler configuration and establishing the complex network of directory structures. Thirdly, various CESM configurations have already been used as part of the Paleoclimate Model Intercomparison Project (PMIP), which compares the outputs of climate models run under various standardized conditions (Joussaume and Taylor, 1995). Finally, the availability of numerous predefined "compsets," or pre-built configurations with specified combinations of component models and initial conditions, make setting up a run based on preindustrial or prehistoric conditions rather straightforward.

2.1.1 Model Configuration

CESM v1.2.2 consists of eight individual components, including seven geophysical system models and a dynamic coupler to manage interactivity. The geophysical systems modeled include the atmosphere (Community Atmosphere Model), land (Community Land Model), ocean (Parallel Ocean Program), sea ice (Community Ice CodE), land ice (Community Ice Sheet Model), ocean waves, and a joint runoff-river transport model (River Transport Model). Our chosen configuration does not use an ocean wave model or the internal ice sheet model, CISM. Coupled ice sheet experiments are instead coupled externally with the Glacial Systems Model (GSM).

Of particular note for our purposes are atmospheric and ocean module configurations. This setup utilizes the Community Atmospheric Model version 5 (CAM5; Neale et al., 2012) at a 1.9° latitude by 2.5° longitude resolution with 30 sigma-hybrid coordinate vertical levels. This is not the highest available resolution for CAM5, but is a practical medium-high resolution choice for long-duration simulations. The ocean component is the Parallel Ocean Program version 2 (POP2) on a pole-rotated grid of approximately 1° resolution. The

rotation of the grid places the North Pole in the middle of Greenland, preventing calculated singularities in volume-oriented fields from occurring at the true geographic north pole.

All components can be run in parallel in a customizable configuration. The optimal parallelization scheme will vary based on the available computer architecture, so the optimization process used for this study is detailed in section 2.1.6.

2.1.2 Baseline Preindustrial Simulation

In order to establish appropriate baseline conditions for the model, a control run is necessary. The control run is integrated for 2500 years of stable preindustrial (i.e., 1850 CE) conditions, which is adequate time to ensure equilibration of most aspects of the simulated climate system (and should be sufficient for statistical equilibrium of all components). An equilibrated model climate that has had consistent forcing input for 2500 years should enable an assessment of the model's stable state, its biases relative to reanalysis or observational datasets, and its range of internal variability.

Standards for paleoclimate modeling studies in the current generation of climate models have been recommended by the members of the Paleoclimate Modelling Intercomparison Project 4 (PMIP4). In a series of four papers, standardized paleo-experiment guidelines are provided for modeling teams wishing to contribute to the comparison project (Kageyama et al., 2018; Otto-Bliesner et al., 2017; Jungclaus et al., 2017; Kageyama et al., 2017). Of particular relevance is their specification of GHGs and orbital configurations for key periods of interest, including the preindustrial control period. We have therefore adopted the same GHG, orbital, land ice configuration, and geography as that specified for the "1850 CE *piControl*" run in Otto-Bliesner et al. (2017). This should enable direct comparisons with similar paleoclimate studies.

2.1.3 Time Slice Selection

Our experiments for past interglacials aim to reproduce the climate conditions of the entire MIS-11c and MIS-5e periods. However, transient simulations of 10,000 years or more are impractical with the computational resources available to this project. A modified "time slice" method (similar to Stone et al. 2013) has therefore been used to develop climate states across MIS-11 and MIS-5. The time slice methodology can fundamentally be described as using shorter simulations to provide windows of insight into much longer climatic periods. For instance, if interested in the evolution of climate over a hypothetical 10,000-year period, one could run simulations of just a few hundred years each with boundary conditions corresponding to the beginning, middle, and end of this period and examine the changes between simulations.

The time slices chosen for our experiments are based upon the identification of precession parameter ($e \cdot \sin\varpi$, where e is eccentricity and ϖ is the longitude of the perihelion) minima and maxima, to the nearest 1000 years. Additional intermediate times are selected to fill large time gaps. Using the Laskar et al. (2004) orbital parameters and insolation, a total of six key points in the orbital forcing trajectory within MIS-11c were identified. These simulations and their respective justifications are as follows:

- 423 ka: intermediate point in orbital forcing, near the beginning of warm interglacial conditions.
- 418 ka: precession index maximum.
- 413 ka: intermediate point.
- 408 ka: precession index minimum.
- 403 ka: intermediate point, near time of estimated sea-level highstand during MIS-11.
- 398 ka: precession index maximum, near the end of interglacial conditions.

This 25,000-year span approximately represents the time period over which global climate approached and then exceeded modern temperatures and sea levels before falling back towards glacial conditions (e.g., Milker et al., 2013; Dutton et al., 2015).

Simulations for MIS-5 similarly cover the entire span of interglacial conditions. However, due to the substantially shorter duration of interglacial warmth compared to MIS-11, only three simulations were initially completed. Upon further examination, it was determined that the climate of MIS-5 evolves relatively rapidly, and some additional intermediate time slices to further resolve these evolutions were completed. The representative time slices are as follows:

- 127 ka: precession index minimum.
- 124 ka: completed later, additional intermediate point.
- 121 ka: intermediate point in precession cycle.
- 118.5 ka: completed later, additional intermediate point.
- 116 ka: precession index maximum, near beginning of re-glaciation in the northern hemisphere.

The 127 kya and 116 kya periods are convenient bookends since proxy records and previous transient simulations have indicated that these roughly correspond to the times when global mean surface temperatures first and last exceeded modern levels, respectively (e.g., Otto-Bliesner et al., 2013; Dutton et al., 2015).

The simulations for each period are branched from end-year 1500 of the standard preindustrial control (piCtrl) simulation and integrated for 1000 years, enabling statistical equilibration of all climate system components except for deep ocean temperatures, which retain a small trend. However, given this project's focus on the Greenland ice sheet, which has only limited marine-terminating ice shelves and at maximum depths of less than 600 meters, deep-ocean temperatures are not considered important for our purposes.

At the branching time, the crucial namelist variables for orbital parameters and GHGs are adjusted to appropriate levels for each period. Some variables, such as ocean temperatures, Atlantic meridional overturning circulation (AMOC) strength, and surface air temperatures, are retained for the full 1000 years to examine their trends and stability. However, most variables are examined only for the final 100 years of each run, corresponding to the "equilibrated" period of each run. How the input orbital and GHG parameters for each run are determined is described in the following sub-section.

2.1.4 Determination of Input Parameters

A crucial component of the model forcing for paleoclimates is GHG concentrations. It is well established that CO2 varies significantly between glacial and interglacial periods; these variations constitute a feedback that simultaneously responds to global conditions like ice cover and temperature and also helps to maintain the mechanism of glacial/interglacial cycles. Methane (CH4) and nitrous oxide (N2O) have also varied widely in the late Pleistocene and have contributed additional small climate forcings. As these are the primary sources of GHG forcing (excluding water vapor, which is explicitly calculated in the model and is very closely tied to oceanic and atmospheric temperatures), they will be adjusted to best represent the period of interest.

For each of the two modeled paleo-eras, carbon dioxide concentrations from the ~800,000 year Antarctic ice core record were obtained from the European Project for Ice Coring in Antarctica (EPICA) record. Their data is primarily composed of a ~650,000 year record from the Dome C ice core site, located at 75.1°S, 123.35°E, 3233 m above sea level (Siegenthaler et al., 2005 and Lüthi et al., 2008), with minor revisions to resolve analytical biases by Bereiter et al. (2015). Greenhouse gas levels for each simulation were then calculated as means of all data points in this record within +/- 2.5 kyr of the time slice date (e.g., 423 ka GHGs were calculated as the mean of 425.5 to 420.5 ka from the EPICA record). This was done to account for the inherent dating uncertainties and short-term fluctuations present within the samples.

Following from the experimental setup of Otto-Bliesner et al. (2017), a nominal adjustment of +23 ppb was made to Antarctic CH4 values due to the assumed latitudinal gradient in methane. Due to its short atmospheric lifetime and having a disproportionate number of sources in the Northern Hemisphere, methane is consistently higher in the NH than the SH throughout modern and Holocene paleoproxy records. Therefore, based on a 46 ppb difference observed between Greenland and Antarctic ice cores for the early Holocene period, the +23 ppb adjustment represents a more appropriate global average value than the raw Antarctic number. The table below shows the GHG concentrations and orbital parameters used for each simulation (Table 2-1).

Experiment	Long. of Perihelion (°)	Eccentricity	Obliquity (°)	CO_2 (ppm)	CH_4 (ppb)	N_2O (ppb)
piCtrl	100.3	0.016764	23.46	284.3	808.2	273.0
6 ka	0.9	0.018682	22.85	269.8	597.0	262.0
MIS-11c Experiments						
423 ka	12.2	0.011374	23.79	268.9	652.8	284.8
418 ka	102.6	0.013295	24.22	273.3	677.0	272.9
413 ka	190.6	0.014836	24.17	273.7	705.3	273.4
408 ka	278.5	0.015795	23.69	280.3	726.1	279.8
403 ka	7.2	0.016067	23.04	279.8	675.4	285.7
398 ka	97.9	0.015498	22.55	276.7	623.4	285.8
MIS-5e Experiments						
127 ka	272.7	0.040986	24.09	273.2	672.7	257.8
124 ka	320.5	0.042243	23.72	271.7	648.0	260.8
121 ka	9.2	0.043149	23.24	272.8	616.8	263.0
118.5 ka	50.4	0.043659	22.85	269.8	582.8	261.9
116 ka	92.2	0.043877	22.54	267.8	533.6	257.2

Table 2-1. Summary information on the orbital and greenhouse gas parameters that were adjusted for each experiment.

As briefly introduced above, Laskar (2004) developed equations for the very precise calculation of orbital parameters for the past several million years. These data are available at 100-year increments starting at the year 2000 and include the precession index, axial obliquity, orbital eccentricity, and the longitude of perihelion. Using the 100-year data, orbital characteristics were plotted, and local minima and maxima of the precession index were identified. As described in Section 2.2, these minima and maxima were used to identify key time slices to simulate in each paleo-era. The nearest even 1000-year increment was then selected as the representative time period, and the orbital parameters used for each run are therefore not exactly at the minima/maxima, but within a few centuries.

2.1.5 Sensitivity Testing and Alternate Baseline

In order to demonstrate that the climate state that develops during each time-slice simulation is independent of the specific initial conditions (within reasonable limits), a sensitivity test was conducted for the MIS-11 time slices. Two versions of the 418 ka simulation were run: one initialized using the conditions from the end of year 500 of the preindustrial control run and one initialized using the conditions from the end of year 500 of the 423 ka simulation. A comparison of the equilibrated periods (last 100 years) of each run indicates that no statistically significant differences exist between them. The preindustrial control initialization was therefore

used for each of the time slice simulations (albeit from year 1500), as this enabled running numerous time slices in parallel to each other.

It should be noted that while 500 years (or even 1500 years) is insufficient to fully equilibrate the deep ocean in the model climate, it should be more than sufficient for the atmosphere, land, and surface ocean to come into statistical equilibrium. This is expected to include adjustments to the AMOC, which has a characteristic response timescale of one to a few centuries (Zhu et al., 2015). Thus, critical effects on the global surface climate, such as surface ocean heat fluxes, storm tracks, air temperature changes and variability, etc., should all be thoroughly accounted for.

In addition to the PMIP4-standard preindustrial control run, a 6 ka mid-Holocene run was also conducted. The 6 ka period is significant for being near the Holocene Climate Optimum, or warmest observed period in the Holocene prior to industrialization (e.g., Renssen et al., 2012). The purpose of this run, which mirrors the other time slice runs in methodology, is to establish climatic conditions for the mid-Holocene with which to force any control/Holocene ice sheet model run that is conducted with data from these climate simulations in the future. It also gives us an additional baseline to which paleo-interglacial conditions can be compared. A protocol for "midHolocene" simulations is also established in Otto-Bliesner et al. (2017), and their GHG and orbital parameters have been adopted for our simulation as well. Ice sheets, geography, and land use are assumed to be the same as the piControl setup.

2.1.6 Processor Optimization

For the chosen model configuration, a number of tests were performed on the HLRN architecture to attempt to optimize the runtime of the model. The HLRN system limits each submitted job to a continuous runtime of 12 hours before stopping; the goal is therefore to optimize the number of simulated climate years per 12-hour block. In order to achieve this, different elements of the model need to be run in parallel, and finding the most efficient partitioning of tasks among compute nodes is the main goal of optimization.

The HLRN-Berlin machine, nicknamed "Lise," is the machine that the control and paleo-simulations were run on. It has 1146 compute nodes consisting of 96 processor cores apiece for a total of 110,016 compute cores. Based on the previous experiences of other researchers with running CESM on older iterations of HLRN machinery, a "first guess" processor configuration was provided at the beginning of the optimization process. However, this configuration was optimized for a machine that had 40 cores per node and used CAM4, which is much less computationally demanding than CAM5. Therefore, notable adjustments in the allocation of nodes were necessary to account for both the changed load distribution and computer architecture.

A trial-and-error testing procedure then followed, with several different sequences of parallel versus serial model components tested. Testing consisted of setting up a run under preindustrial control conditions and integrating using standard time steps and coupling frequencies for a total of 1 model year. The integration time was then recorded in order to estimate the number of years that could be calculated per 12-hour block.

The ocean and atmosphere models were always run in parallel, though with varied processor ratios between them. Several different configurations of the land, sea ice, coupler and runoff models were then tested, with different arrangements of components and different processor ratios between them. The diagram below illustrates the configuration that was ultimately utilized for all runs (Figure 2-1), with the order of operations within each model time step flowing from top to bottom. Boxes that are side-by-side are processed in parallel, whereas those aligned sequentially are computed after those components above them. The diagram illustrates only the rough structure of the configuration; while the widths of the boxes are proportional to the number of cores allocated to each component, the vertical axis is not indicative of the time taken for each component to complete simulation.

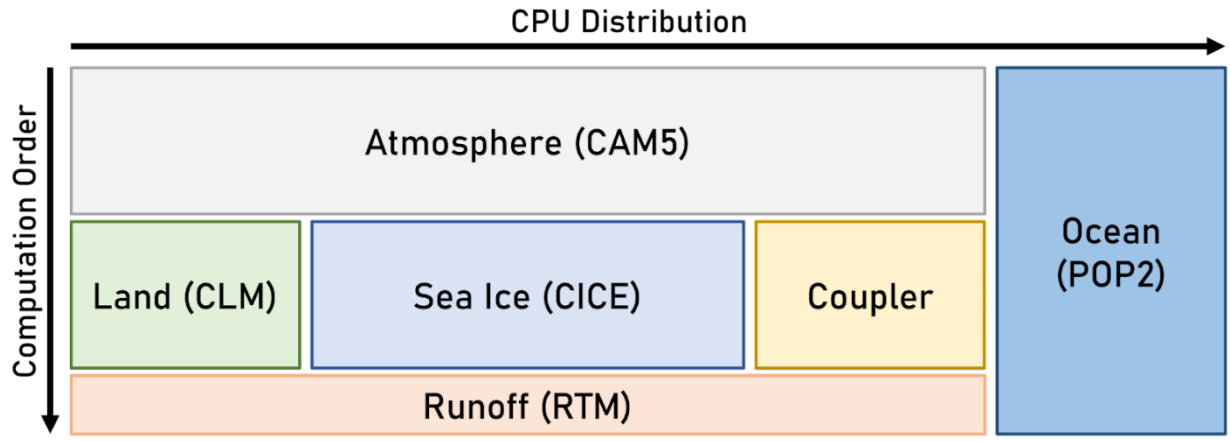

Figure 2-1. Schematic illustration of the parallelization scheme used for all CESM simulations in this study. The horizontal width of the boxes is directly proportional to the number of assigned processor cores. The time taken for each computation is represented schematically in the vertical axis, but the vertical dimension of the boxes is not proportional to computation time.

The most efficient tested configuration consists of the land model, sea ice model, and coupler operating in parallel following the atmosphere. The runoff model, which has a very low computational burden, simply follows the land/sea ice/coupler sequence and takes just a few seconds per time step. (The ocean runs in parallel to the entire atmosphere → land/sea ice/coupler → runoff sequence). While using the runoff model in sequence is not the most efficient possible outcome computationally, the alternative of parallelization resulted in a larger amount of wasted resources due to the short time it takes to calculate runoff per time step. The key issue for computational efficiency is balancing the two heaviest components of the model, which are the atmosphere and the ocean.

Ultimately, a 4:1 ratio of compute nodes was used for atmosphere to ocean. Processors used for the atmosphere then divided the remaining non-ocean tasks as illustrated in the conceptual diagram, with varying ratios between land, sea ice, and the coupler. A final arrangement of 1:2:1 was used for the ratio between land, sea ice, and coupler processors, with the runoff model then taking only a few seconds afterwards and utilizing just a quarter of the atmosphere processors at the end of the sequence. This configuration is capable of running 25 model years in approximately nine hours on average using a total of 960 processor cores.

2.2 Ice Sheet Model

The second manuscript of this dissertation consists in large part of coupled ice-climate simulations of the Greenland ice sheet (GrIS) of MIS-11c. The climate forcing is extracted from the MIS-11 CESM simulations described above. The ice simulations are conducted offline, however, not utilizing CESM's built-in ice sheet model. Procedures for extracting and reformatting climate data are described briefly below in Section 2.2.2. More detailed information on the selection of GSM parameters and our study-specific MIS-11c initialization procedure are provided in Chapter 4.3-4.5.

2.2.1 Model Description

The Glacial Systems Model is an ice-sheet model that has been specifically developed for simulating large-scale glacial features through one or more entire glacial-interglacial cycles. It is an unparallelized model that is designed for running large ensembles and includes parameterizations of as many uncertain glacial processes as possible (Tarasov et al., in prep.). Spatial resolution is limited to a maximum of around 10 km for continental-scale simulations, but subgrid models for surface mass balance and ice flow are included. Our simulations utilized a resolution of 0.5 degrees longitude by 0.25 degrees latitude.

GSM is a hybrid shallow shelf/shallow ice approximation model (SSA/SIA), utilizing an evolution of the dynamical core from Pollard and DeConto (2012 and 2015). The ice thermodynamics are energy-conserving, and the bed thermodynamics explicitly resolve permafrost and include corrections for seasonally snow-covered land surfaces. The bed mechanics are based on a global visco-elastic glacial isostatic rebound solver (Tarasov and Peltier, 1997). It utilizes a 4 km deep permafrost-resolving bed thermodynamics model that also contains adjustments for seasonal snow cover of ice-free regions (Tarasov and Peltier, 2007). Its positive degree day (PDD) scheme has a novel inclusion of shortwave radiation fluxes, lending it additional complexity in comparison to traditional PDD schemes.

GSM is typically two-way coupled to the earth-system model of intermediate complexity LOVECLIM (Goosse et al., 2010; Bahadory and Tarasov, 2018; Bahadory et al., 2021), but was adapted for the purposes of this study to accept one-way forcing from AOGCMs like CESM. This involves conversion procedures for many of the CESM outputs that are described in more detail in the Methodology sub-section of Chapter 4, primarily consisting of regridding to the appropriate latitude-longitude grid, unit conversions where necessary, and the writing out of inputs in a plain-text format specific to GSM.

2.3 Calendar Correction Procedure

Thanks primarily to a combination of precession of the equinoxes and variable eccentricity, the modern-day calendar does not necessarily offer an appropriate delineation of seasons under past orbital conditions. Instead, it makes sense to view global seasonal progression in an angular sense, with each calendar month corresponding to a particular slice of Earth's orbit around the sun (i.e., each month would correspond to a 30° section of Earth's orbit in a hypothetical 12-month calendar with identical month lengths). When paleoclimate

simulations are conducted utilizing a fixed 365-day calendar, as the CESM simulations described here are, corrections become necessary for obtaining representative monthly or seasonal climatologies.

MIS-11c had very low eccentricity throughout, similar to the orbital configuration of the present day, and thus the calendar effects are minimal. However, MIS-5e is characterized by rather high eccentricity, and seasonal extremes are thus heightened. Prior to analyzing all MIS-5e CESM outputs, we have therefore recalculated monthly data using the PaleoCalAdjust program described in Bartlein and Shafer (2019).

PaleoCalAdjust first calculates the angular month centroids relative to a fixed 21 March spring equinox. It then calculates the variable month lengths in terms of modern calendar dates by applying modern calendar month lengths (assuming 365 days every year, e.g., February has 28 days) and therefore a new start and end "date" for each month. Monthly-mean data is then interpolated to daily and re-aggregated within the boundaries of the newly-aggregated months. The resulting time series should be more representative of monthly data in terms of how it would typically be viewed relative to the modern calendar - i.e., "January" data will reflect the equivalent portion of Earth's annual orbit that begins shortly after the winter solstice.

After this process is complete, the timestamps contained in the netCDF files that are produced are irregular, reflecting the new start, median, and end dates of the recalculated months. To ensure smooth read-in to Python analysis programs and interpretation by e.g. the Climate Data Operators (CDO) and netCDF Operators (NCO) packages, a post-processing script is then implemented to re-impose the original, regular timestamps.

2.4 Model Data Analysis

Finally, analysis of output from both CESM and GSM was conducted primarily with numerous Python scripts. Most output data was in the form of netCDF, which cooperates well with the Python package Xarray (Hoyer and Hamman, 2017). Maps were produced utilizing Matplotlib (Hunter, 2007) and its since-deprecated subsidiary, Basemap.

Data utilized in the study contained in Chapter 3 (Crow et al., 2022a) was made publicly available for download via PANGAEA (Crow et al., 2022b).

Chapter 3

Dynamic boreal summer atmospheric circulation response as negative feedback to Greenland melt during the MIS-11 interglacial

Brian R. Crow[1,2], Matthias Prange[1,2], Michael Schulz[1,2]

[1]MARUM - Center for Marine Environmental Sciences, University of Bremen, 28359 Bremen, Germany
[2]Faculty of Geosciences, University of Bremen, 28359 Bremen, Germany

Manuscript published in Climate of the Past, 2022, (18) 775-792, doi: 10.5194/cp-18-775-202

Abstract. The unique alignment of orbital precession and obliquity during the Marine Isotope Stage 11 (MIS-11) interglacial produced perhaps the longest period of planetary warmth above preindustrial conditions in the past 800 kyr. Reconstructions point to a significantly reduced Greenland ice sheet volume during this period as a result, although the remaining extent and volume of the ice sheet are poorly constrained. A series of time slice simulations across MIS-11 using a coupled climate model indicates that boreal summer was particularly warm around Greenland and the high latitudes of the Atlantic sector for a period of at least 20 kyr. This state of reduced atmospheric baroclinicity, coupled with an enhanced and poleward-shifted intertropical convergence zone and North African monsoon, favored weakened high-latitude winds and the emergence of a single, unified midlatitude jet stream across the North Atlantic sector during boreal summer. Consequent reductions in the lower-tropospheric meridional eddy heat flux over the North Atlantic therefore emerge as a negative feedback to additional warming over Greenland. The relationship between Greenland precipitation and the state of the North Atlantic jet is less apparent, but slight changes in summer precipitation appear to be dominated by increases during the remainder of the year. Such a dynamic state is surprising, as it bears stronger resemblance to the unified-jet state postulated as typical for glacial states than to the modern-day interglacial state.

3.1 Introduction

The Marine Isotope Stage 11c interglacial (approximately 424 ka to 395 ka; hereafter MIS-11) is likely the longest and one of the warmest interglacials of the past million years (e.g., Lisiecki and Raymo, 2005; Raymo and Mitrovica, 2012). Its climatological significance lies in the extent to which sea levels rose during this period, estimated at around 6-13 meters above that of the present day (Dutton et al., 2015). A substantial percentage of this rise is attributed to the melt of the Greenland ice sheet (GrIS), which may have contributed as much as 4 m to 7 m of its estimated 7.4 m of present-day sea-level equivalent water content (Morlighem et al., 2017; Robinson et al., 2017). Antarctica has recently been estimated to have contributed another 6.7-8.2 m (Mas e Braga et al., 2021). The prolonged warmth of this period therefore is of direct relevance to understanding the processes that cause GrIS melt, a highly pertinent question as planetary warming is likely to continue in the near future.

As suggested by the wide range in sea-level rise estimates, considerable uncertainty exists with regards to both the degree of melt of the GrIS and the global and regional temperature anomalies during MIS-11. Pollen records indicate the development of some boreal coniferous forests around the margins of southern Greenland at some point during MIS-11 (de Vernal and Hillaire-Marcel, 2008; Willerslev et al., 2007), indicating both the prevalence of ice-free ground and sufficient summer warmth to support tree growth. Peak temperatures during this time remain poorly constrained, however. While some ice-core data (e.g., Masson-Delmotte et al., 2010) and sea surface temperature (SST) reconstructions (Dickson et al., 2009) suggest global temperatures 1-2°C warmer than preindustrial, with Arctic anomalies potentially several degrees higher (Melles et al., 2012), orbital parameters and greenhouse-gas (GHG) measurements are broadly similar to those of the Holocene (Berger and Loutre, 2003). As such, climate models have historically struggled to replicate the temperature anomalies implied by both the limited paleo-temperature records and the implied degree of GrIS melt (e.g., Robinson et al., 2017; Reyes et al., 2014).

A mechanism invoked as potential means for achieving and sustaining higher temperatures during MIS-11, particularly in the Arctic during boreal summer, is a strengthened Atlantic meridional overturning circulation (AMOC; Rachmayani et al., 2017). The authors of that study ascribed this strengthening primarily to salinity increases in the North Atlantic, in turn a product of favorable alterations of the surface wind and pressure fields inducing stronger ocean surface currents. The extent to which factors related to atmospheric transport of heat and moisture are involved was left as a question for future research, and one that we attempt to address further in our analysis.

Multiple modelling approaches have been utilized to attempt to refine understanding of the MIS-11 interglacial climate. Computing resources are a major limitation to simulating multi-millennial timescales with modern complex climate models. Researchers typically choose between using simplified or low-resolution models such as Earth system models of intermediate complexity (EMICs; e.g., Yin and Berger, 2012; Ganopolski and Calov, 2011) or simulating shorter “snapshots” of the climate state at representative key periods (e.g., Herold

et al., 2012; Stone et al., 2013; Milker et al., 2013; Rachmayani et al., 2016, 2017). The latter approach is often referred to as the "time slice" method, and is frequently adopted when utilizing complex coupled atmosphere-ocean global climate models (AOGCMs). A complex AOGCM such as the Community Earth System Model (CESM; Hurrell et al., 2013; Gent et al., 2011) would require many months of computation time to complete a transient simulation of the MIS-11 interglacial even on a high-performance computer; thus the time slice approach is more practical for capturing the evolution of the climate over such a long period.

Still others have utilized a combined approach, running both an EMIC and an AOGCM over several time slices to compare them with each other and with reconstructions. Kleinen et al. (2014) produced broadly similar estimates of the climate state in MIS-11 with both CLIMBER2 (an EMIC) and CCSM3 (an AOGCM), though the increased resolution of CCSM3 enabled much better identification of regional climate features, such as the enhanced African summer monsoon during the 410 ka and 416 ka periods of MIS-11. Verifying such climatic signals is difficult due to the limited spatial and temporal resolution of proxy records during MIS-11 (e.g., Milker et al., 2013), but are important to identify to the extent possible. Robust regional climatic changes, especially in the tropics, are known to contribute to remote changes in mid- and high-latitude climate via teleconnection mechanisms (e.g., Yuan et al., 2018).

A key aspect of replicating the regional distribution of temperature changes under different climate forcing regimes is adequately capturing feedback mechanisms internal to the climate system. Orbital forcing in particular has widespread consequences, as different distributions and intensities of surface heating cause the atmospheric and oceanic circulations to respond in different ways (e.g., Merz et al., 2015; Fischer and Jungclaus, 2010). Despite relatively modest changes in the magnitude of seasonal insolation values throughout most of MIS-11, the latitudinal distribution of insolation is still notably different relative to the preindustrial period. The high Northern Hemisphere summer insolation during a long interval of MIS-11 was responsible for both enhancing the African monsoon and weakening the mean hemispheric lower-tropospheric baroclinicity (Rachmayani et al., 2016; Mohtadi et al., 2016; Wu and Tsai, 2021). Both weakened midlatitude baroclinicity in the atmosphere and enhanced tropical forcing have been identified as mechanisms for shifting the preferred state of the North Atlantic upper-tropospheric jet stream from a split regime (separate subtropical and polar front jets) to a unified hybrid jet regime (Lee and Kim, 2003; Son and Lee, 2005; Andres and Tarasov, 2019). Altered jet regimes in turn have consequences for the development and propagation of atmospheric eddies, thus affecting a major source of atmospheric heat at high latitudes (e.g., Nakamura and Oort, 1988; Overland and Turet, 1994; Serreze et al., 2007).

Internal climate system mechanics contributing to the pronounced melt of the GrIS during MIS-11 remain largely unidentified. In the present study, we utilize some of the highest-resolution climate simulations performed to date under MIS-11 conditions in order to parse these mechanisms further. In particular, our interest lies in identifying the atmospheric changes across the North Atlantic sector that were most consequential for mass balance changes in the Greenland ice sheet. We therefore explore the extent to which

insolation-induced changes in the jet stream may have led to feedbacks affecting the poleward transport of atmospheric heat and moisture.

3.2 Methods

3.2.1 Model configuration

The climate model chosen for this study is the CESM v1.2.2, a fully coupled atmosphere-ocean general circulation model with sea ice, land, and runoff components. The CESM and Community Climate System Model (CCSM) family has been widely utilized in paleoclimate studies. Our particular configuration utilizes the Community Atmosphere Model version 5 (CAM5). The land and atmosphere models have an approximate resolution of 1.9° latitude by 2.5° longitude with 30 hybrid coordinate vertical layers in the atmosphere. The ocean and sea-ice grids are comprised of an orthogonal curvilinear grid at nominally 1° resolution with the North Pole displaced over Greenland to avoid singularities in flux calculations in the Arctic Ocean.

Fixed present-day ice sheet topography was assumed for all MIS-11 time slice experiments, and therefore the land ice model component was disabled. This is perhaps the largest assumption of these simulations, but enables isolation of the effects of changing orbital and GHG forcings on the simulated climate. Options for applying different ice sheet configurations were also severely limited by the sparse Greenland ice-core data extending back through MIS-11, and only a small number of modelling studies have produced transient reconstructions (e.g., Robinson et al., 2017). CESM version 1 and CAM5 do have a well-documented high-latitude cold bias due to a combination of anomalously strong high-latitude circulation features and radiative effects (e.g., Wang et al., 2018); however, our simulations are internally consistent, as the same core model configuration is merely compared with different parameters.

A control run was conducted which adheres to the standards set forth by the Paleoclimate Modelling Intercomparison Project 4 (PMIP4) for a preindustrial baseline (Otto-Bliesner et al., 2017). This simulation was integrated for 2500 years to enable full equilibration of the surface climate and quasi-equilibration of deep-ocean temperatures. The experimental MIS-11 runs were branched from year 1500 of the control integration, with only orbital and GHG parameters altered as described below.

3.2.2 Experimental design and parameters

The time slice technique (see e.g., Stone et al., 2013; Rachmayani et al., 2017) was utilized in this study, as transient simulations of 20 kyr duration or more remain prohibitively expensive in a relatively high-resolution AOGCM. Each selected slice is integrated for 1000 years at constant forcing conditions, enabling effective equilibrium of the surface climate (entire atmosphere and upper portion of the oceans) at conditions representative of the selected time. This timescale is insufficient for complete equilibration of the deep oceans. However, as the Greenland ice sheet does not have large ice shelves grounded at or below sea level, this is judged unimportant for our study (c.f. Varma et al., 2016). Temperature trends in the deep ocean are also modest in our simulations, with typical drift being on the order of 0.05°C century^{-1} below 1000 meters depth. The 1000 years of each experiment consist of 900 years of spin-up time, then the final century is treated as the

equilibrated period. All results presented are therefore 100-year time series or averages from the end of each simulation. The time slices were chosen to align approximately with minima and maxima in precession (which has a powerful modulating effect on the seasonal distribution of insolation) during the warm interglacial period of MIS-11. Intermediate 5 kyr steps were also selected to ensure fuller coverage of the period of interest. The characteristic parameters of each time slice and the preindustrial control run are detailed in Table 3-1.

Experiment	*Long. of perihelion (°)*	*Eccentricity*	*Obliquity (°)*	*CO_2 (ppm)*	*CH_4 (ppb)*	*N_2O (ppb)*
piCtrl	100.3	0.016764	23.46	284.7	791.6	275.7
423 ka	12.2	0.011374	23.79	268.9	652.8	284.8
418 ka	102.6	0.013295	24.22	273.3	677.0	272.9
413 ka	190.6	0.014836	24.17	273.7	705.3	273.4
408 ka	278.5	0.015795	23.69	280.3	726.1	279.8
403 ka	7.2	0.016067	23.04	279.8	675.4	285.7
398 ka	97.9	0.015498	22.55	276.7	623.4	285.8

Table 3-1. Orbital parameters and GHG values used as fixed inputs into each simulation.

For each experimental simulation, orbital parameters were calculated following Laskar et al. (2004) at the representative time period. Greenhouse-gas concentrations were obtained from the European Project for Ice Coring in Antarctica (EPICA) record, primarily consisting of data from Dome C (Siegenthaler et al., 2005; Lüthi et al., 2008). Following the experimental setup detailed in Otto-Bliesner et al. (2017), a nominal +23 ppb adjustment was applied to Antarctic CH4 values, accounting for the fact that methane persistently exists in higher concentrations in the Northern Hemisphere during interglacials. GHG values represent means of a 5 kyr window around the representative time (i.e., 423 ka GHG values are given by a mean of all values between 425.5 ka and 420.5 ka), which accounts for the inherent uncertainty in GHG values due to short-term variability (centennial and millennial scale) and the analysis techniques.

A sensitivity experiment was also conducted to ensure that the results of the time slice experiments were not dependent upon initialization. To this end, additional simulations for 418 ka were conducted, branching from year 500 of the preindustrial control run and from year 500 of the 423 ka run. A comparison of the equilibrated periods (final 100 years of each integration) showed that no statistically significant differences existed between them.

3.2.3 Statistical techniques

A number of correlation plots are presented in the results section. These present Pearson's *r* values, 95% confidence intervals of the *r* values, and *p* values. Pearson's *r* is calculated with respect to the mean values of given quantities for each particular time slice. On interannual timescales, regional temperatures, eddy heat fluxes, etc. are noisy and influenced by a number of different factors. The most prudent comparison is therefore between the long-term mean patterns in each time slice simulation. When correlating 2 m air temperature and precipitation for all MIS-11 experiments, for example, the values correlated consist only of the six mean

seasonal precipitation values from the time slices and the six mean seasonal temperature values from the time slices. The *n* for these correlations is therefore only six, and the degrees of freedom just four. In reality, 600 total seasonal values likely have a much greater number of degrees of freedom, although each time slice's 100 years of data is best classified as a red-noise time series and therefore does not have a full 100 degrees of freedom (Thomson, 1982). The significance of the correlations presented are therefore conservative.

Student's *t* tests are also employed to determine whether climatological changes between the time slice simulations and the preindustrial simulation are significant. For all variables tested, the seasonal values at each grid point and in each time slice are treated as an independent time series ($n = 100$). This necessarily assumes spatial independence of each grid point. Critical values and *p* values are then obtained based on the effective degrees of freedom of each time series, reduced from 100 based on the lag-1 autocorrelation. The inherent assumption of normally distributed, spatially independent variables is not fully applicable for spatially coherent, non-normal variables like wind, eddy heat flux, and precipitation, but degrees of freedom are sufficiently large in all cases to ensure that *t* testing retains some explanatory power (Decremer et al., 2014). The 95% confidence threshold presented in all figures here should not be considered as absolute, but an approximate representation of where anomalies are noteworthy.

3.3 Results

3.3.1 Surface temperature response

The surface temperature response is the most obvious effect of the varying orbital and GHG conditions throughout MIS-11 (Fig. 3-1). Global-mean 2 m air temperatures were at or modestly above preindustrial levels for each of the 423-408 ka simulations (dark blue). As expected, the temperature pattern is considerably amplified over Greenland, with positive anomalies reaching 2-3°C above preindustrial during the warmest period (413 ka). This result generally aligns well with the temperature anomalies over Greenland from two other recent studies utilizing EMICs for transient simulations of MIS-11. First, an ensemble of coupled REMBO-SICOPOLIS simulations with transient ice sheets was performed by Robinson et al. (2017), depicted in the gray line and shading in Fig. 3-1. Their simulations in turn rely on temperature anomalies derived from a transient climate simulation from the CLIMBER2 EMIC (Ganopolski and Calov, 2011). Our simulations deviate significantly from the these at the first time slice (423 ka), and to a lesser extent at 418 ka. This is most likely a result of our simulations assuming a fixed ice modern-day Greenland ice sheet, whereas the transient simulations still had greater Greenland and North American ice coverage from the previous glaciation. This is affirmed by further comparing our simulations to those of Yin et al. (2021), who utilized LOVECLIM1.3 with transient orbital and GHG forcing, but fixed present-day ice sheets. Near-surface air temperatures from their simulations (light red in Fig. 3-1) averaged around Greenland match our results very closely, including at 423 ka. Except for the discrepancies at 423 ka, differences between the fixed ice and fully transient simulations are otherwise minimal during MIS-11.

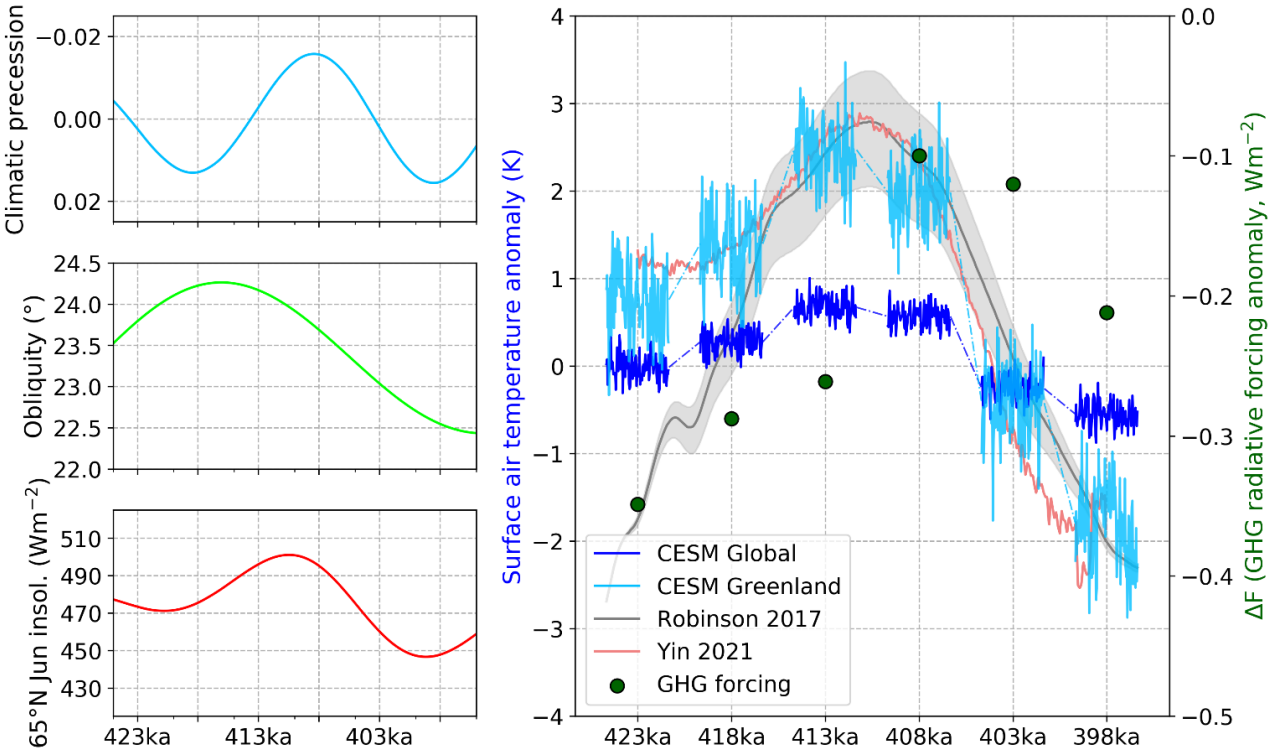

Figure 3-1. (Left) Orbital parameters and high-latitude summer insolation during the MIS-11 interglacial. (Right) Mean boreal summer global and area-weighted mean Greenland (55-85°N, 280-350°E) 2 m air temperature anomaly "pseudo-time series" relative to the preindustrial control simulation are given by the dark blue (global) and light blue (Greenland) curves. The pseudo-time series depict seasonal-mean boreal summer (June-July-August; JJA) values from the final 100 years of each simulation; the time *x* axis is therefore not to scale for these curves and the discontinuities are larger than depicted. The gray curve is the time series of JJA mean temperatures over Greenland from Robinson et al. (2017), which is based on an ensemble of transient, coupled REMBO-SICOPOLIS simulations; the surrounding grey shading represents the 95% confidence interval for temperatures based on this ensemble, while the solid line represents the likeliest estimate. The light red curve is the temperature time series for the Greenland region from the fixed ice LOVECLIM simulation of Yin et al. (2021). The green dots in the right panel indicate the radiative forcing anomaly based on the combined effects of CO2, CH4, and N2O, after IPCC (2001).

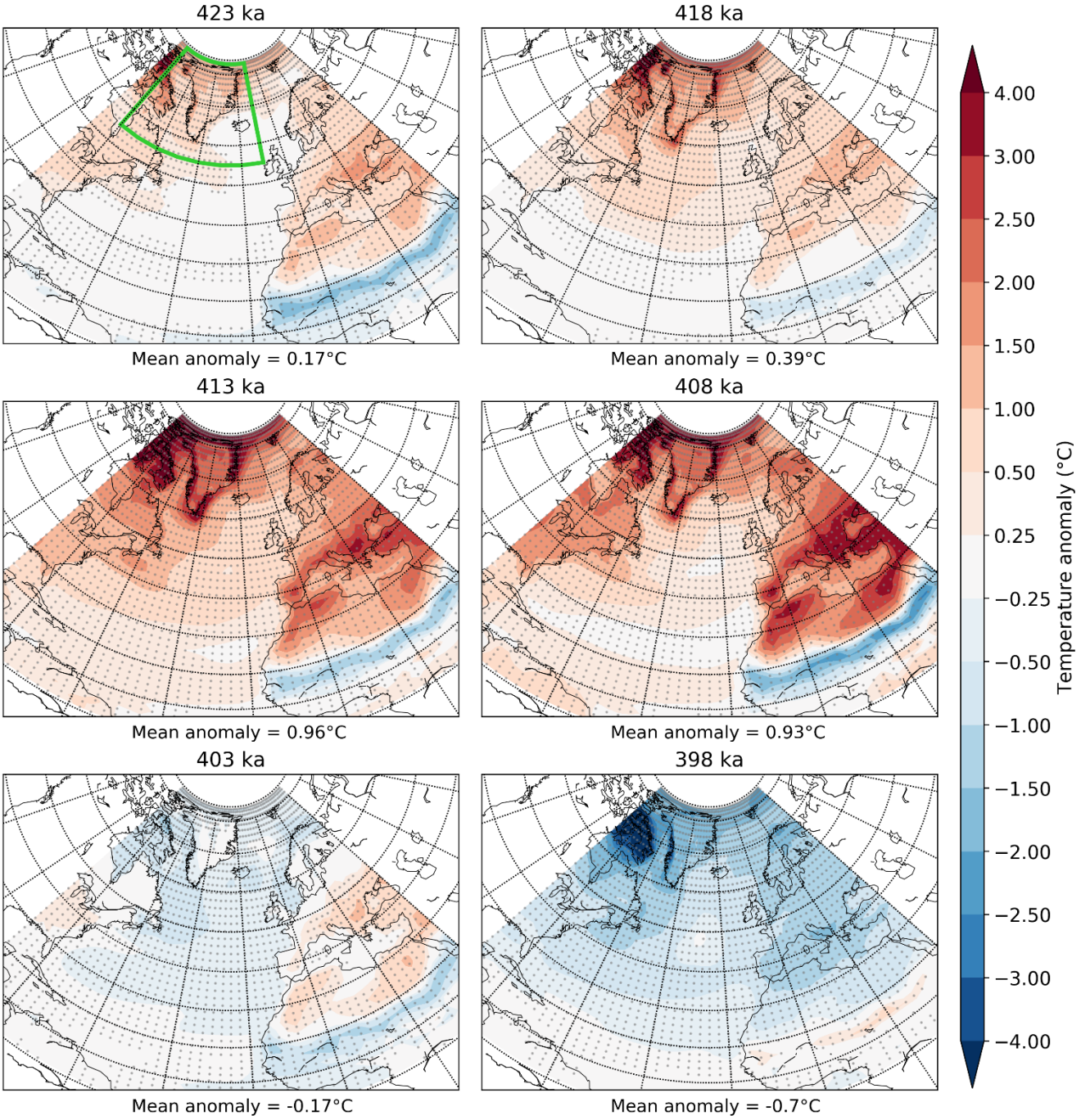

Figure 3-2. Mean JJA 2 m temperature anomalies for the final 100 years of each CESM simulation corresponding to the listed time slices. Regions with stippling pass Student's *t* test at the 95% significance level. The green box in the 423 ka panel indicates the averaging region for the mean temperature values used in Fig. 3-1 and in the correlation plots (Fig. 3-4 and 3-7), 55-85°N and 280-350°E. The mean anomaly value listed beneath each panel is a cosine-weighted mean value of the complete shaded area (0-87°N, 270°E-40°E).

The spatial distribution and magnitude of boreal summer temperature anomalies across the North Atlantic sector also varied notably throughout the analysis period (Fig. 3-2). Anomalies as high as 4-5°C above pre industrial are evident around northern Greenland and the Canadian Arctic during the peak warmth of 413-408 ka due to the combined effects of high insolation and regional feedbacks, including reduced sea-ice cover (not shown). More modest and relatively uniform warming is present across much of the rest of the Atlantic basin, with the exception being areas immediately surrounding the Mediterranean Sea. A narrow but stark band of 1-2°C cool anomalies stands out in sub-Saharan Africa during the 423 ka and 413-408 ka simulations, the result

of increased cloud cover and surface cooling induced by evaporation associated with enhanced monsoonal and intertropical convergence zone (ITCZ) convection. Also evident is the abrupt return of surface air temperatures to near-preindustrial conditions by 403 ka and substantial cool anomalies by 398 ka, consistent with conditions potentially favorable for renewed glaciation.

Inevitably, these results contain some bias introduced by using a fixed modern-day Greenland ice sheet in the simulations. In addition to the aforementioned warmth at 423 ka, temperature anomalies are likely somewhat underestimated over Greenland itself for later analysis periods, as the lowering and partial removal of ice surfaces would have enabled even warmer conditions. Additionally, changes in Greenland topography may also induce further warming on local to regional scales due to katabatic winds (Merz et al., 2014). These potential biases are particularly relevant for the 413-398 ka time slices, when the ice sheet was likely smaller than the present day.

Regardless of the exact magnitude of summer warming during MIS-11, the signal for large, statistically significant warming at high latitudes is robust. One clear consequence of strong warming at high latitudes, especially when paired with tropical surface cooling over Africa, is the reduction of the mean Equator-to-pole surface temperature gradient, and thus the contribution of the thermal wind balance to the geostrophic flow. A dynamic adjustment of baroclinic processes is therefore to be expected, including attendant changes in jet stream and baroclinic eddy behavior.

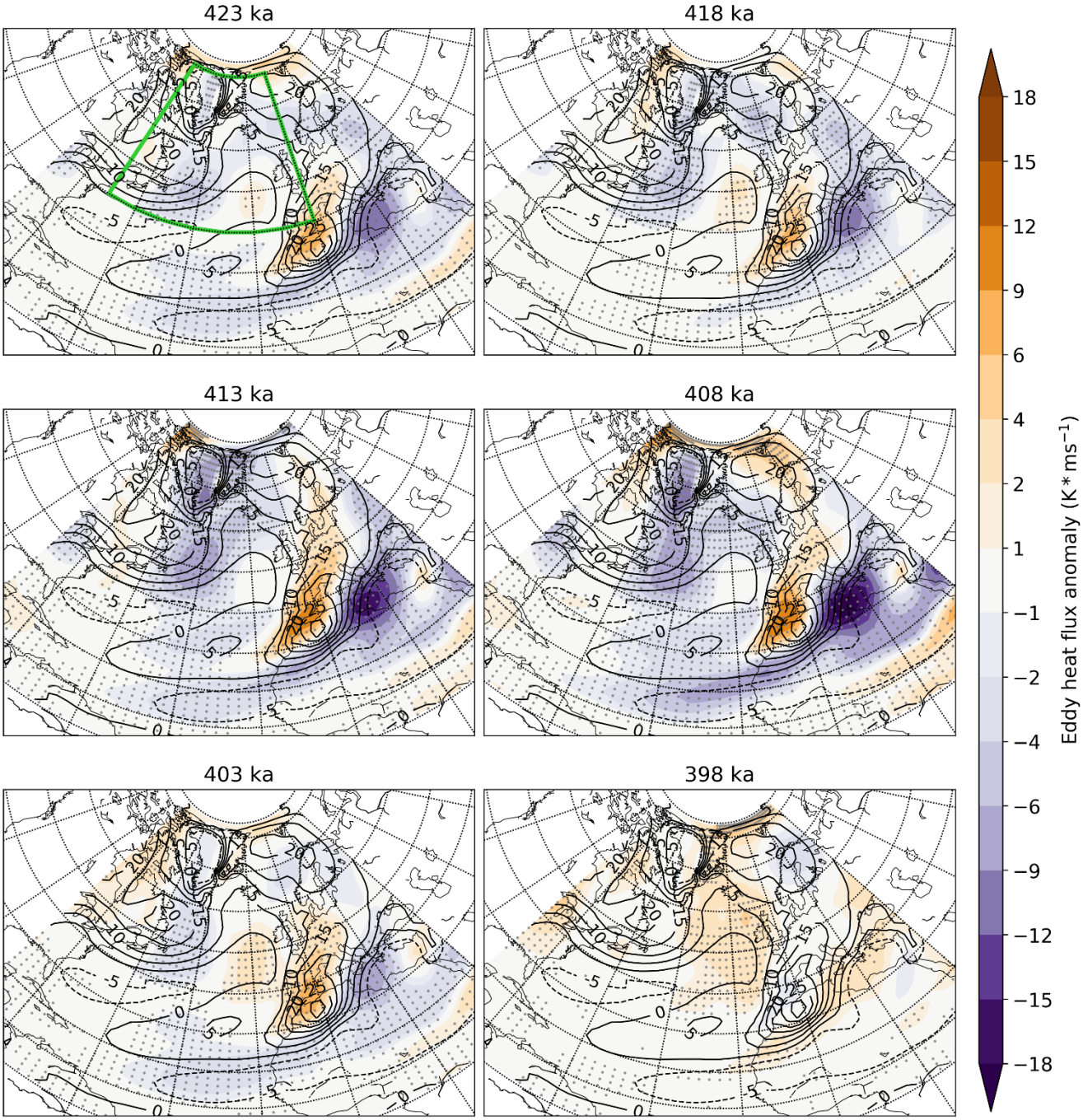

Figure 3-3. Mean lower-tropospheric (700 hPa) total eddy heat flux anomalies over the North Atlantic. Black contour values indicate the mean JJA total eddy heat flux from the final century of the piCtrl run (baseline climatology). Shaded values shown are boreal summer mean anomalies over the final 100 years of each designated simulation, stippled where the difference is statistically significant at the 95% level. The green box in the 423 ka panel shows the area (40-80°N, 290-0°E) over which area-mean values are computed for correlations in Fig. 3-4 and 3-8.

3.3.2 Atmospheric eddy response

Particularly robust changes are present in the lower-tropospheric meridional eddy heat flux (EHF) anomalies across the North Atlantic sector. Note that future references to baroclinicity, meridional temperature gradients, or eddy heat fluxes in this text are concerning only lower-tropospheric quantities, and EHF in general refers to the meridional flux of heat by atmospheric eddies. Figure 3-3 illustrates the mean patterns of total (transient plus stationary) boreal (sensible) summer eddy heat flux anomalies relative to the preindustrial control

simulation. Stationary eddy heat fluxes are defined as $\overline{v^*}\,\overline{T^*}$, where v^* and T^* are the zonally anomalous meridional wind and temperature, respectively, with anomalies calculated at daily intervals and at the 700 hPa atmospheric pressure level before being averaged to seasonal values. Transient eddy heat fluxes are likewise defined as $\overline{v'T'}$, or the product of the time-anomalous meridional wind and temperature. The total EHF is simply the sum of the transient and stationary meridional eddy heat fluxes and is, in effect, representative of the heat-advecting effects in the lower-to-middle troposphere of the atmospheric waves captured in the model. Over the large majority of the analysis domain, total meridional EHF anomalies are dominated by the transient eddy component (not shown). The values represented in the figure are averages of all the June-July-August (JJA) days in the 100-year period, relative to the preindustrial simulation.

Two features in the total meridional EHF anomaly fields stand out. First, the couplet of positive and negative anomalies over southwestern Europe and the central Mediterranean during 423-408 ka is indicative of a robust shift in the favored storm track. Positive EHF anomalies are indicative of either an increased and anomalous meridional temperature gradient or frequent large southerly wind anomalies (transient or stationary), or more likely, some combination thereof. Given that the mean temperature gradient appears unchanged or even slightly weaker (Fig. 3-2), the likely source of this anomaly is increased frequency and/or intensity of wave activity and meridional transport in this region. Conversely, reductions exist over the central Mediterranean, consistent with a shift in baroclinic wave activity away from this region. Considered together, the strong anomaly couplet (for all periods except 398 ka) over Europe and the Mediterranean represents a northwestward shift in the mean storm track over the eastern Atlantic.

A second region of widespread and statistically significant reduction in total eddy heat fluxes is present over much of Greenland and the open North Atlantic. The magnitude is overall smaller than the anomalies over Europe and the Mediterranean, but rather than marking a simple shift or intensification of the preindustrial pattern, it appears to resemble an entirely different wave pattern. Meridional heat flux from eddies is clearly reduced in the MIS-11 simulations (except 398 ka) in a broad area extending from the Canadian Maritime Provinces up through much of Greenland, a region that experiences relatively large meridional EHF in the preindustrial mean (black contours in Fig. 3-3). As will be discussed in Section 3.3.3, this is a clear indication of an altered storm track across the North Atlantic.

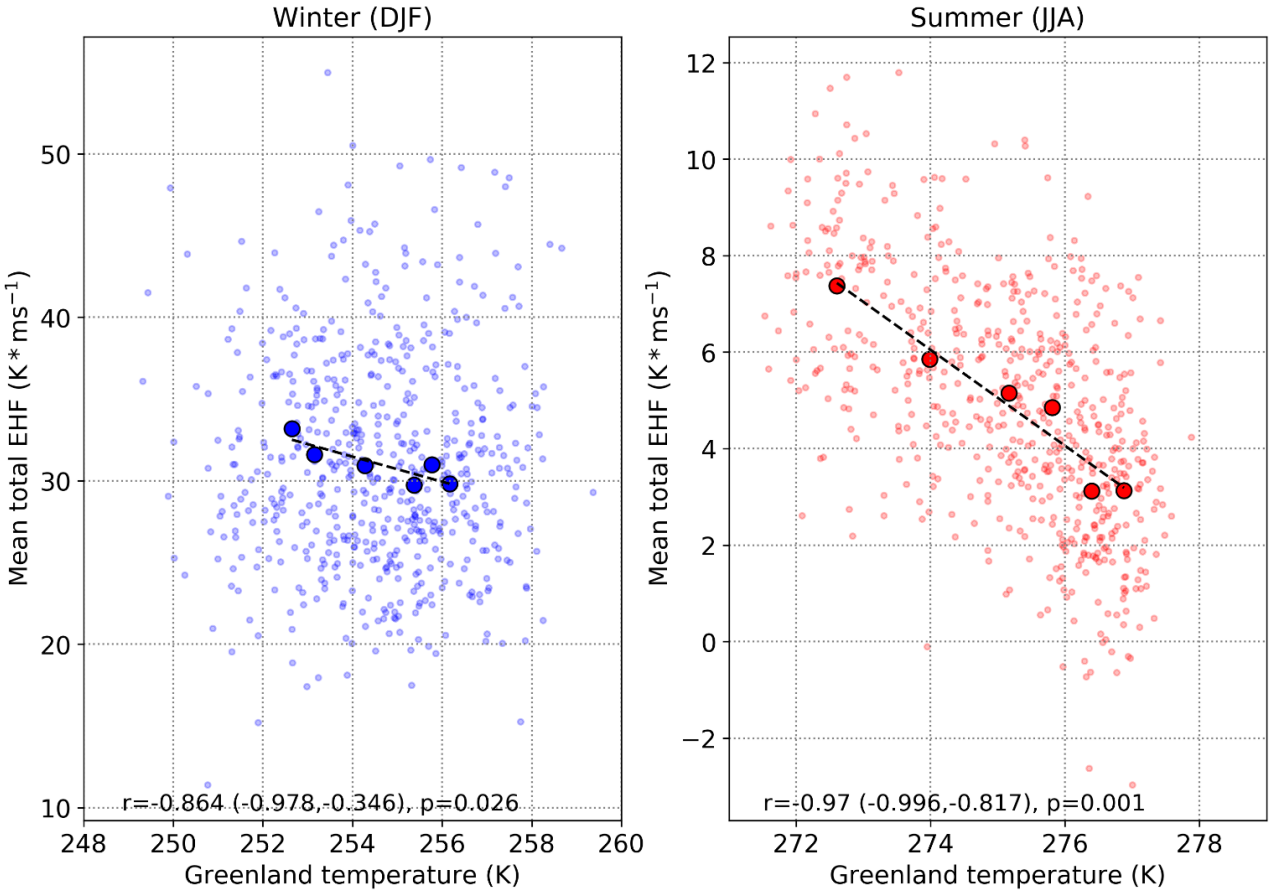

Figure 3-4. Correlations between the mean surface air temperature around Greenland (55-85°N, 280-350°E) and the seasonal-mean total (stationary + transient) eddy heat flux over the North Atlantic (40-80°N, 290-0°E). Correlations, *p* values, and trend lines are calculated using mean values of temperature and EHF anomalies for each of the six time slices. Individual years are lightly colored small dots, and the mean of each of the six time slice simulations are given by large, outlined dots.

As implied by comparing the eddy heat flux and surface temperature maps, a strong negative correlation exists between the temperature averaged over Greenland and its immediate surroundings (the region enclosed by the green box in the top-left panel of Fig. 3-2) and the mean eddy heat flux over the North Atlantic region (the larger region enclosed by the green box in Fig. 3-3). The strength of this relationship is also strongly dependent on the season (Fig. 3-4). While both boreal winter-mean and summer-mean EHF-temperature relationships exceed the 95% confidence threshold, the correlation is much stronger and has a much narrower confidence interval in boreal summer. This can be partly explained by the much larger magnitude and variability of seasonal-mean North Atlantic eddy heat fluxes in winter, but is also indicative of a more robust dynamic response in the summer season.

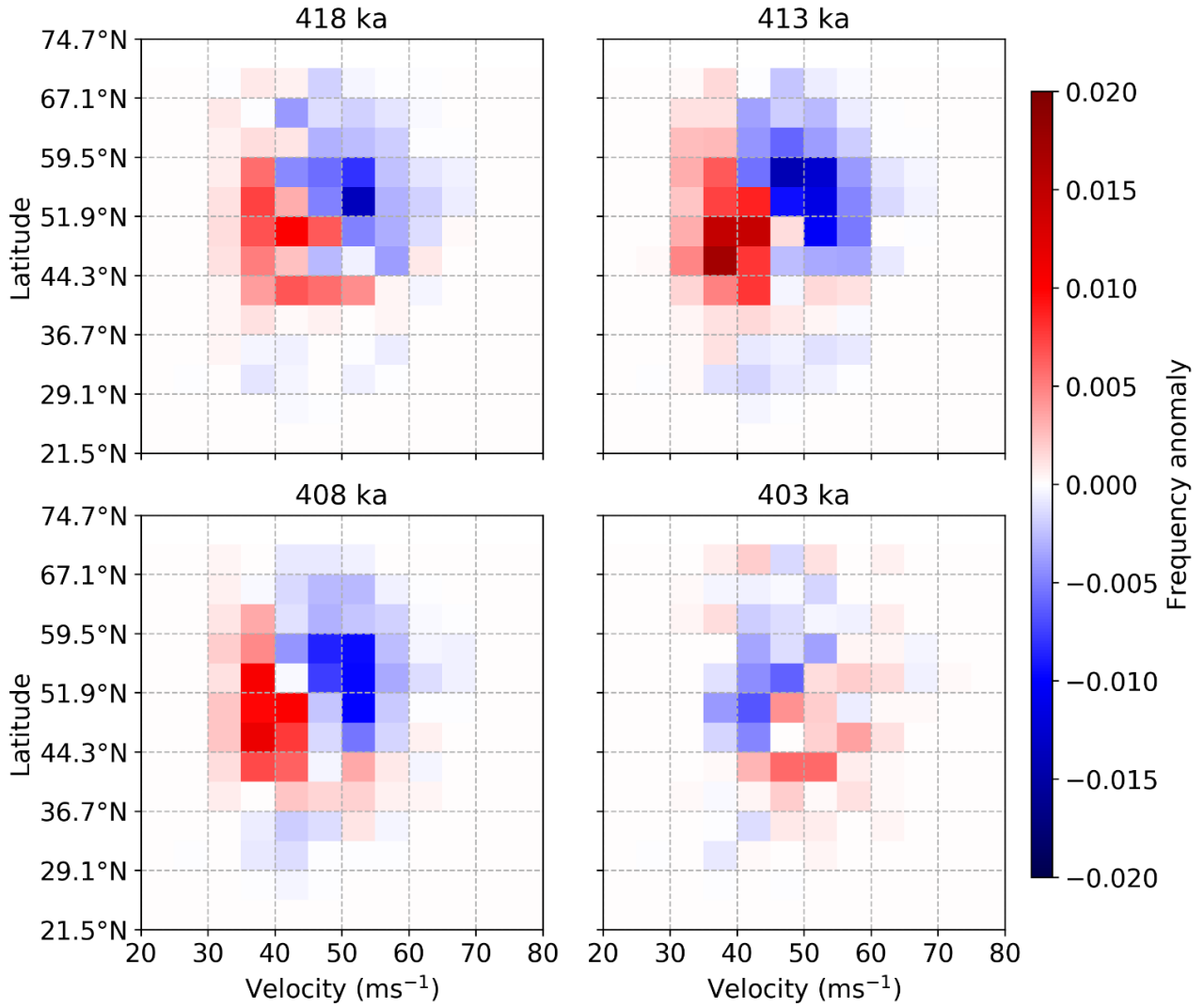

Figure 3-5. Changes in the frequency of the latitude and peak velocity of JJA daily maximum 300 hPa winds over the North Atlantic for the core MIS-11 interglacial period of 418-403 ka. Latitude bins are approximately 3.8°, containing two model grid cells each. Velocity bins are at intervals of 5 m s^{-1}. Frequency matrices are computed relative to the preindustrial control simulation, and the velocity maxima reflect the maximum single value at any grid point in the analysis domain.

3.3.3 Jet stream response

While reduced meridional temperature gradients play a role in reducing eddy heat fluxes, changes in eddy activity are the dominant cause. Eddy activity in the midlatitudes has a symbiotic relationship with the jet stream, which both drives and is driven by wave activity. An attendant change is therefore expected in jet behavior, which is apparent in the daily jet frequency matrices (Fig. 3-5). A clear shift in the favored latitude and strength of the boreal summer North Atlantic jet is evident, with weaker and lower-latitude daily maximum 300 hPa winds clearly favored in the 418 ka, 413 ka, and 408 ka experiments. These three warm periods also show a slight reduction in the frequency of low-latitude jet maxima, denoted by the slight negative frequency anomalies on the lower flank of the robust couplet. This is consistent with a decreasing tendency towards wind maxima in the typical (modern) latitude of the subtropical jet, an observation which is further supported by the presence of negative mean 300 hPa wind anomalies (Fig. 3-6).

Thus, both purely eddy-driven high-latitude jet maxima and purely subtropical jet maxima are reduced (the southern flank subtropical wind weakening is even more clearly visible in the *u* component of the wind field; not shown), with the dominant state instead emerging as a broad hybrid eddy-thermal jet in the midlatitudes. Son and Lee (2005) used an idealized aquaplanet model simulation to demonstrate that either weakened midlatitude baroclinicity or stronger tropical ascent could cause the jet to transition to a unified state. Interestingly, both mechanisms are present during MIS-11 boreal summers in our considerably more realistic simulations. As discussed in Section 3.3.1, baroclinicity changes are clear in the temperature anomaly patterns (Fig. 3-2) and additionally implied by the robust negative correlation between jet strength and mean 2 meter air temperature over the North Atlantic (Fig. 3-7). As will be discussed further in Section 3.3.5, the band of tropical cooling over Africa is a result of increased convection, cloud cover, and evaporative surface cooling, thus indicating enhanced tropical ascent.

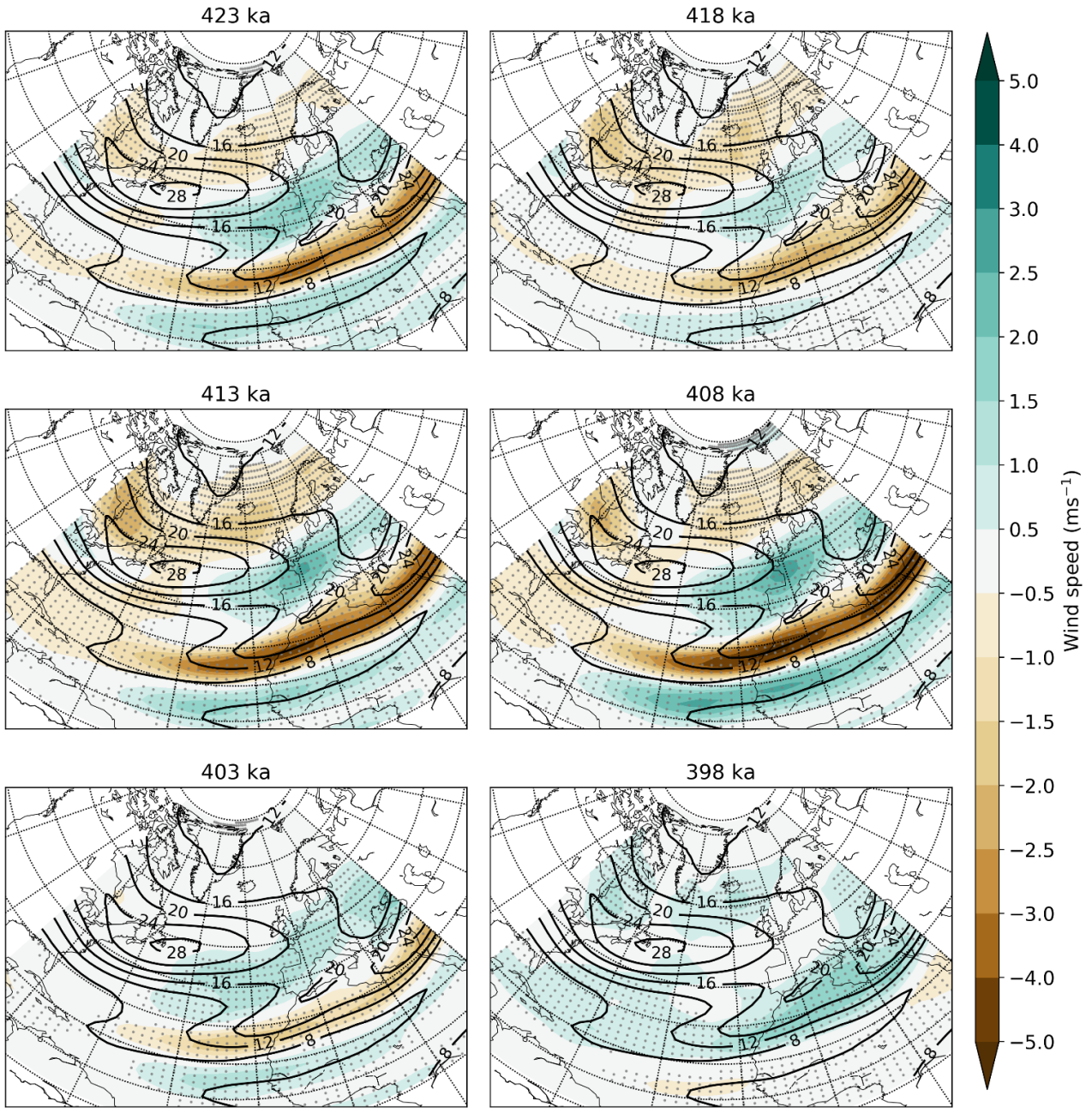

Figure 3-6. Mean JJA wind anomalies at 300 hPa across the MIS-11 simulations (colors) and climatological 300 hPa wind velocities from the piCtrl simulation (black contours). Anomalies significant at the 95% level via *t* testing are stippled. Evident reductions in mean winds across both the typical subtropical jet location (~25-35°N) and the typical polar jet location (~50-70°N) are present in most time slices, along with increases in mean winds across the eastern midlatitude North Atlantic and western Europe.

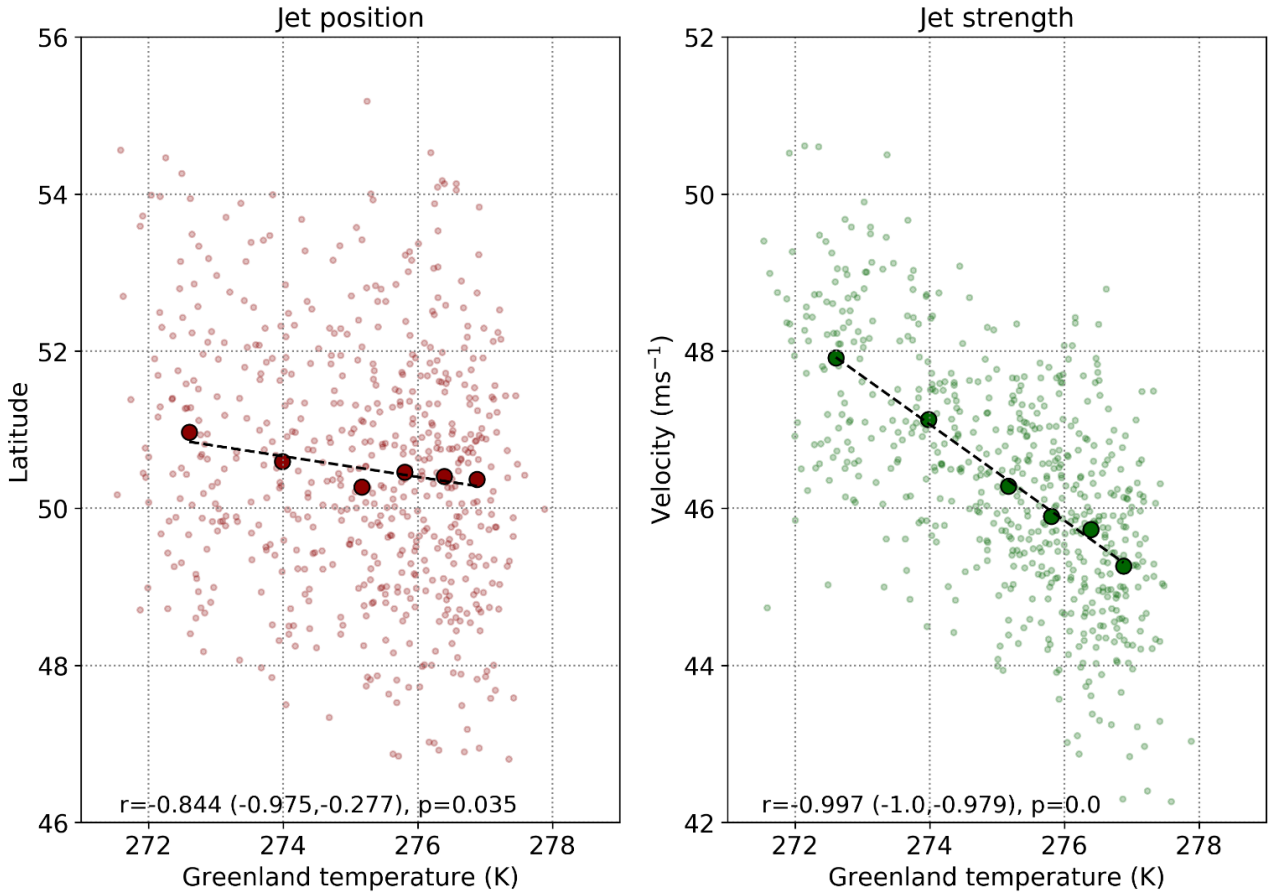

Figure 3-7. The relationships between the JJA-mean Greenland (55-85°N, 280-350°E) 2 m air temperature and the latitude (left) and magnitude (right) of maximum 300 hPa winds across the North Atlantic. As in Figure 3-4, correlations, best-fit lines, and *p* values are calculated with respect to the overall means of each time slice (indicated by large, outlined dots). The smaller dots represent the seasonal-mean values for each of the 100 years of each time slice.

3.3.4 Eddy-jet relationship

Notably, the region with the large couplet in EHF anomalies over western Europe and the Mediterranean (Fig. 3-3) corresponds approximately with the largest changes in jet stream wind strength (Fig. 3-6). Since the changes in EHF are dominated by the transient component, it is clear that the emergence of these anomalies is associated with a significantly altered North Atlantic storm track. A more baroclinically active JJA storm track across this region appears to be the consequence of the merged jet state, which is also consistent with the trapping of atmospheric waves equatorward of a merged jet (e.g., Nakamura and Sampe, 2002). Reduced baroclinic eddy activity on the poleward flank of the merged jet explains the existence of the opposite state (reduced EHF) across much of the open North Atlantic. The contrast is made clear by examining the 300 hPa wind (Fig. 3-6) and total eddy heat flux maps (Fig. 3-3). During 423-403 ka, large reductions in EHF are present across the central and North Atlantic in association with the weakened polar jet to varying degrees; in cooler-than-preindustrial 398 ka, these have been replaced by small positive anomalies in association with the return to a split-jet state.

Interestingly, correlations between EHF anomalies and jet characteristics fail to paint quite so clear a picture. While hints of a relationship between jet latitude and North Atlantic-mean EHF (mean over a box spanning

40-80°N and 70°W-0°E) exist, the correlation does not reach significance at the 95% confidence level (Fig. 3-8). However, EHF exhibits a strong positive correlation with boreal summer jet strength in the North Atlantic. Our simulations indicate that split-jet states are associated with higher absolute maximum jet strengths. Therefore, the strong positive correlation between higher maximum jet velocities and North Atlantic meridional EHF implies greater EHF during split-jet regimes, and reduced EHF during the prevailing merged-jet regime of MIS-11 boreal summers.

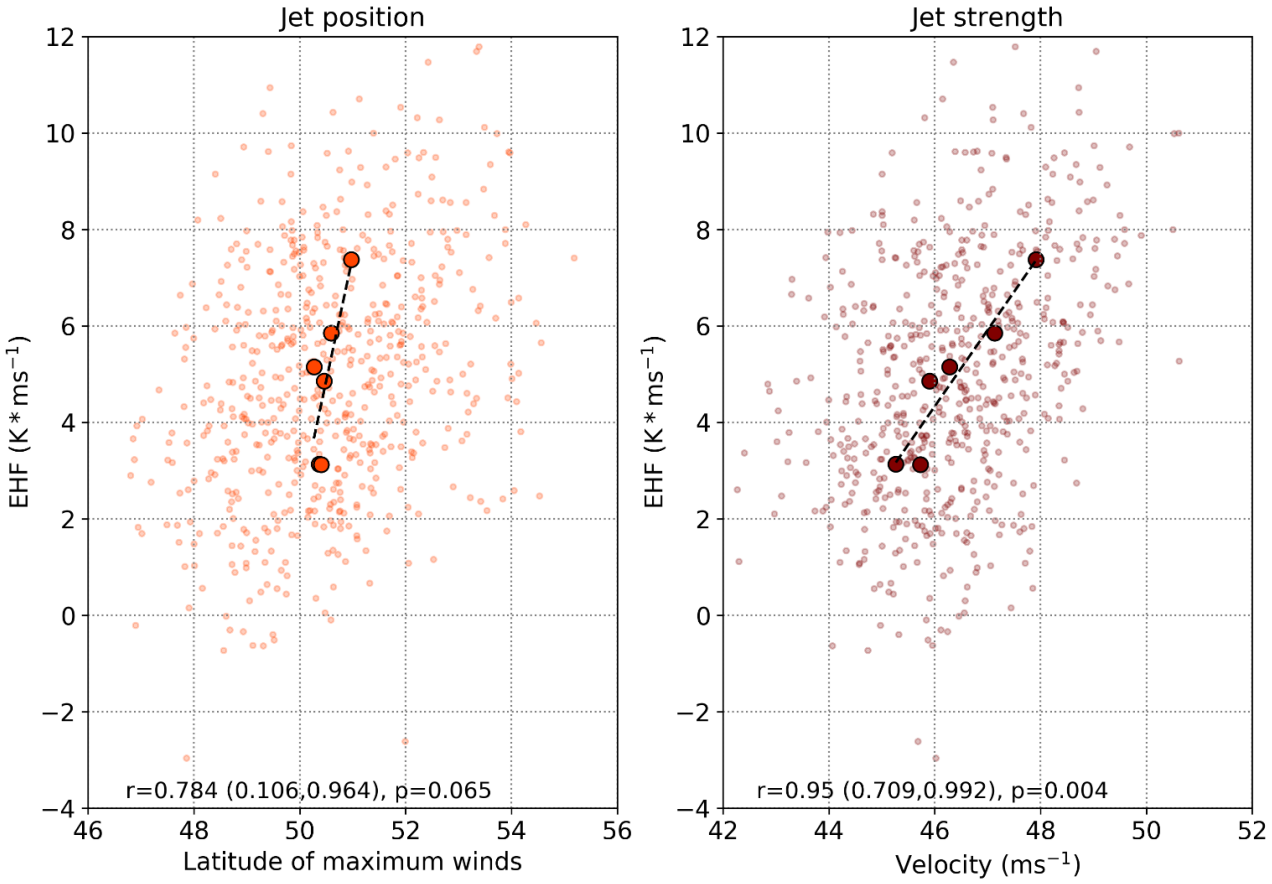

Figure 3-8. Correlations between summer mean seasonal values of the latitude of maximum 300 hPa winds (left panel), the magnitude of jet maximum winds (right panel), and total eddy heat flux over the North Atlantic (40-80°N, 290-0°E). Correlation does not reach 95% significance for jet position, but the correlation with jet strength is robust.

3.3.5 Precipitation and the storm track

Precipitation across the Greenland ice sheet is highly seasonal, predominantly driven by extratropical cyclones, and strongly enhanced along major orographic features, particularly in the southeast (Chen et al., 1997). With such a pronounced change in eddy behavior (extratropical cyclones) as a result of the shifted jet, a logical consequence would seem to be a positive correlation between jet strength and precipitation over Greenland. However, exactly the opposite appears to be the case (Fig. 3-9), with a significant but small negative trend in precipitation associated with higher North Atlantic wind maxima based on time slice means. A considerable amount of noise exists among the individual annual values, however, so this result should be treated with some caution. As is the case with the EHF correlations (Fig. 3-8), only the relationship between maximum jet velocity and precipitation obtains 95% significance.

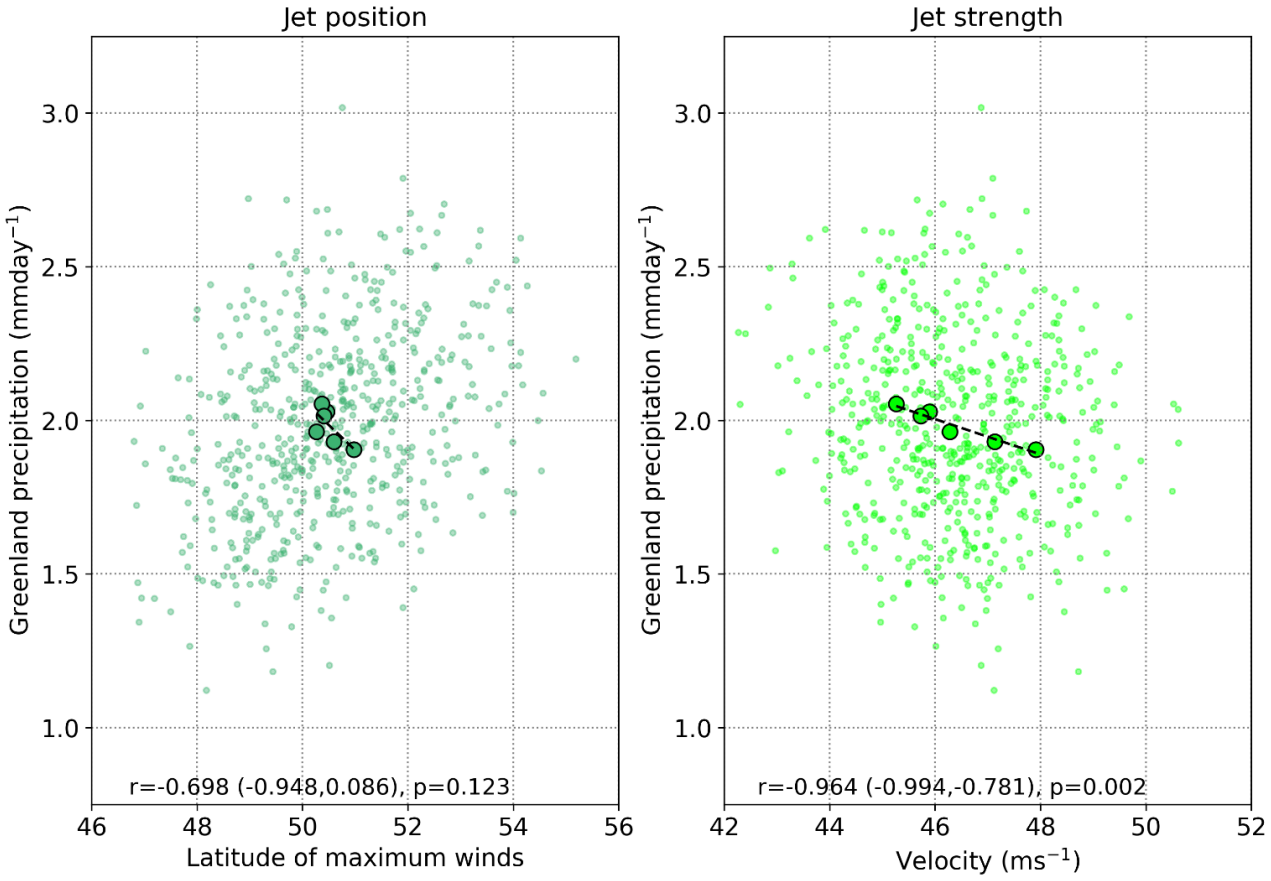

Figure 3-9. Relationships between JJA-mean latitude of maximum 300 hPa winds (left), the magnitude of the maximum jet wind (right), and seasonal-mean precipitation over Greenland (land-only). As with eddy heat fluxes, the correlation is only significant for jet strength.

Competing effects appear to be influencing precipitation over Greenland in these simulations: intuitively, increases in eddy heat flux should correspond to increases in eddy moisture flux (EMF). However, comparing the jet state to total EMF over the North Atlantic directly results only in a statistically insignificant correlation (not shown). On the other hand, we have demonstrated that warmer North Atlantic temperatures are associated with weaker jets, and lower-tropospheric air temperature places a strong cap on atmospheric moisture. The apparent negative correlation between maximum jet winds and precipitation over Greenland (Fig. 3-9) therefore appears to be overwhelmingly driven by the inverse relationship between temperatures over Greenland and jet strength. Behavioral changes in the jet and eddies exhibit only a secondary influence.

Spatially, the largest boreal summer precipitation changes across the analysis domain appear to be related to the strength of the African monsoon (Fig. 3-10). Specifically, a drying is noted across much of the midlatitude Atlantic and much of central and southern Europe, consistent with the general shift of the preferred storm track and suggestive of increased subsidence from the poleward flank of the Hadley cell. The magnitude of subtropical drying appears to be roughly proportional to the increase in precipitation over sub-Saharan Africa, strongly suggesting the influence of tropical convection on the altered jet state. Precipitation increases across west/central Africa associated with the increased monsoon are evident through the 423-403 ka periods, peaking at over 175% of preindustrial under 408 ka conditions. Attendant decreases of around 5-25% over Europe, 25-

50% for most of the Mediterranean, and 5-25% across the Caribbean and western subtropical Atlantic are also evident during 413 and 408 ka. The largest monsoon precipitation increases appear to occur at 418 ka and 408 ka, roughly corresponding with the periods of most negative precession (perihelion occurring near/during boreal summer).

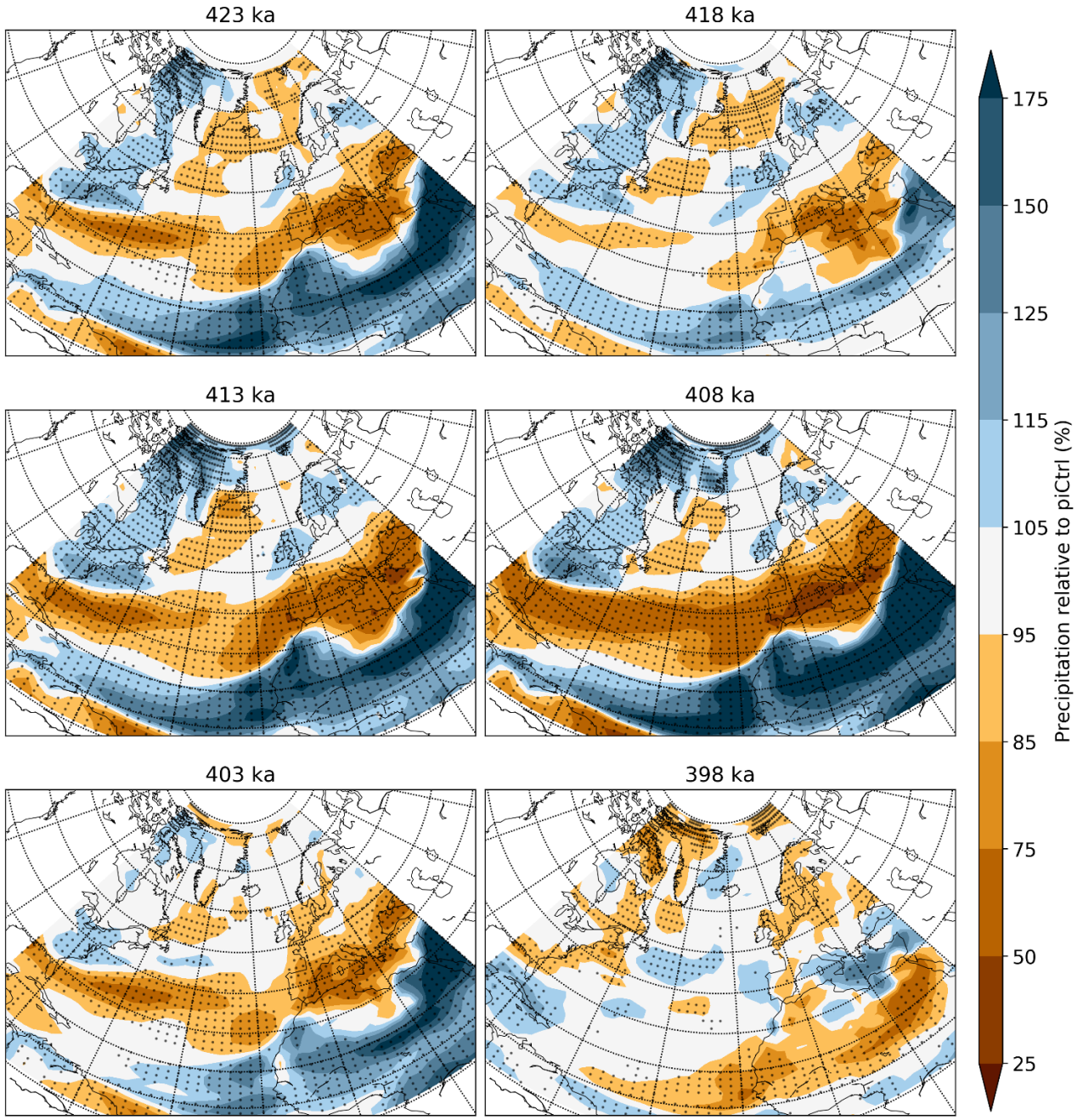

Figure 3-10. Time slice mean summer precipitation anomalies across the North Atlantic throughout MIS-11, indicating slight increases in precipitation on the western slope of Greenland with corresponding decreases in the southeast from 423 to 408 ka. Stippled regions correspond to grid points significantly different from the preindustrial control simulation at the 95% confidence level.

Over Greenland, boreal summer precipitation changes during the warm 423-408 ka period resemble that of orographic precipitation during dominant westerly/northwesterly wind regimes: positive precipitation anomalies along the western slopes and negative anomalies along and just off the southeastern coast. In absolute terms, these anomalies are relatively small, on the order of 0.1-0.3 mm day^{-1}, but constitute

statistically significant 5-25% increases. In the annual mean, however, a near-opposite pattern emerges in precipitation anomalies for southeastern Greenland (Fig. 3-11). Simulated annual average precipitation rates increase there by 5-15% for the 418-408 ka period. Since the bulk of the southeastern Greenland precipitation increase occurs in the cool season, it occurs overwhelmingly as snow (not shown but confirmed by model precipitation-type output), and therefore contributes to an increase in the mass balance of the ice sheet across southeastern regions.

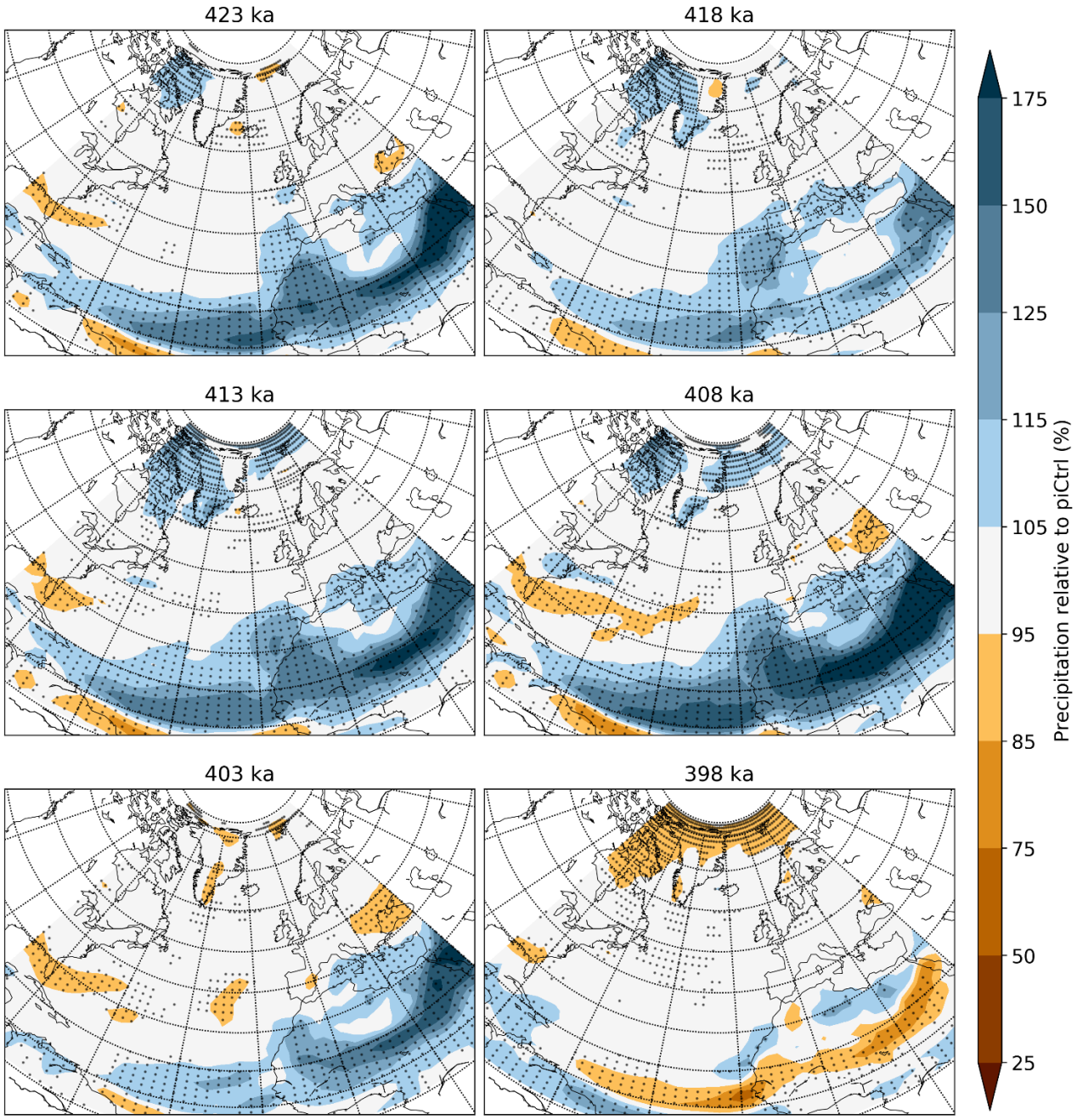

Figure 3-11. As in Figure 3-10, but for the annual mean period.

3.4 Discussion

Our results compare favorably with the limited previous modelling studies conducted to assess MIS-11 climate. The same pronounced high-latitude warming and narrow region of tropical cooling identified in our

study with CESM was also found by Kleinen et al. (2014) in both an EMIC (CLIMBER2) and an AOGCM (CCSM3), suggesting a signal robust to various climate models. Likewise, they identified the enhancement of the African monsoon and the migration and strengthening of tropical convection over the eastern Atlantic, albeit with a more limited spatial extent of increased precipitation than in our simulations. Further analysis of the same two CCSM3 time slices in Rachmayani et al. (2016) confirmed these temperature and precipitation relationships.

The consensus among recent climate modelling studies therefore indicates a robustly strengthened African monsoon during MIS-11 in boreal summer. Despite severe limitations in the availability and spatial coverage of reliable proxy records from this time period, the data that exist appear to support this. Decreased deposition of terrigenous iron in the deep ocean off the coast of northwestern Africa during the period 420-396 ka indicates a substantially less dusty (i.e., wetter) northwest African climate during this time (Helmke et al., 2008). Also coincident with this development was the occurrence of increased deposition of organic matter in the eastern Mediterranean (sapropel 11), approximately dated to 407 ka and likely the result of increased freshwater input from the Nile River as eastern African rainfall increased (Kroon et al., 1998; Lourens, 2004). Timing the African wet period to a resolution greater than a few thousand years or determining precisely the magnitude of the rainfall changes is still beyond the precision afforded by these records; however, they do offer some general verification of the signal produced by the model consensus.

Primary responsibility for the changes in both the African monsoon and the midlatitude baroclinicity naturally lies with the insolation changes. Both inter-hemispheric and intra-hemispheric changes to the insolation gradient have roles to play, with the relatively high obliquity conditions of the early-middle MIS-11 interglacial (ca. 423-408 ka) a chief contributor to the lower-tropospheric low-baroclinicity conditions in boreal summer. High obliquity conditions are responsible for increased high-latitude insolation in the summer hemisphere, thus driving the reduction in the meridional surface temperature gradient seen in our simulations (Mantsis et al., 2014). Furthermore, high obliquity enhances the inter-hemispheric temperature gradient, sustaining a stronger Hadley circulation and causing a poleward shift in the Hadley cell in the summer hemisphere (Mantsis et al., 2014). Climatic precession is known to have the dominant effect on the state of the north African monsoon (e.g., Bosmans et al., 2015), which is illustrated in our simulations by the emergence of the strongest monsoon conditions during 408 ka (and, conversely, the weakest monsoon precipitation anomalies nearest precession maxima at 418 and 398 ka). The favorable alignment of moderate-low precession and moderate-high obliquity throughout much of MIS-11 thus produces sustained Northern Hemisphere boreal summer warmth as well as monsoon and jet responses over an anomalously long period.

As others have noted, the changes in baroclinicity seen during MIS-11 will likely be mirrored to some extent by present and future GHG-induced global warming, suggesting the possibility of a strengthened African monsoon and northward-shifted Atlantic ITCZ in the not-so-distant future (Mohtadi et al., 2016, and references therein). In the present climate, it has been demonstrated that an improved understanding of western African convection can significantly improve weather forecast skill across Europe and the North Atlantic due to

teleconnection patterns (e.g., Pante and Knippertz, 2019). Long-term and large-scale mean circulation anomalies in the west African monsoon region thus have far-reaching implications for regional or global weather and climate patterns, including over Greenland. Improved understanding of the two-way dynamic linkages between patterns of tropical convection during boreal summer and changes in the North Atlantic circulation are necessary in order to optimize predictions of future Greenland ice sheet behavior.

It also remains to be determined to what extent the jet-eddy response identified here is robust to all models, given the variable degree to which the North Atlantic storm track tends to be southward-biased in Climate Model Intercomparison Project (CMIP) models (Harvey et al., 2020). Numerical models can also struggle to replicate the magnitude and latitudinal extent of the west African monsoon circulation, which, given the sensitivity of the midlatitude jet to tropical forcing in our simulations, suggests another potential bias of concern (e.g., Brierley et al., 2020). Our study also does not test the sensitivity of the jet-eddy response to varying levels of GHGs under identical orbital forcings, which are subject to some uncertainty for paleo-periods like MIS-11 given millennial-scale fluctuations and the relatively low temporal resolution of GHG records (variable between a few hundred and approximately 1000 years). Natural limitations on the availability of quality reconstructions will almost certainly continue to prevent true "validation" of modelling results as well.

The use of a fixed modern-day Greenland ice sheet in our climate simulations represents probably our most significant assumption, although the effects of this are less important in the summer than in the winter (Merz et al., 2014). Elevation reductions on the order of several hundred meters across the GrIS would result in 2 m air temperature increases of several degrees Celsius, further enhanced by albedo reductions due to the melting of the ice sheet and emergence of bare rock, soil, and vegetation across marginal regions. In fact, modelling sensitivity studies examining future scenarios have identified these factors as contributing to notably larger GrIS ablation areas and sea-level rise from Greenland melt when accounted for in a two-way coupled simulation (Le clec'h et al., 2019). Failure to account for the increased freshwater discharge from the ice sheet in periods of substantial melt may also affect local ocean circulations and sea-ice formation, which can in turn feed back into Greenland air temperatures and local atmospheric circulation (e.g., Merz et al., 2016). It is also possible that these feedback mechanisms may result in further reduced baroclinicity across the North Atlantic sector, possibly further reinforcing the unified-jet state and leading to additional reductions in eddy heat fluxes.

Competing effects on precipitation are also possible: increased atmospheric moisture content is expected over a warmer, lower-elevation Greenland surface; however, the diminished topography in large sections of Greenland would be expected to reduce the production of orographically induced precipitation. We plan to investigate the dynamic atmospheric response to a greatly reduced GrIS under MIS-11 climate conditions in a future sensitivity study, and thus hope to better assess the appropriateness of the fixed ice sheet assumption.

3.5 Conclusions

Using CESM time slice simulations of only insolation and GHG forcing conditions corresponding to the MIS-11 interglacial, we have uncovered a robust dynamic atmospheric response that includes negative feedbacks to further melting of the Greenland ice sheet. Increased high-latitude insolation due to a favorable alignment of high obliquity and relatively low-amplitude climatic precession variations across a time interval of around 20 kyr drives pronounced, sustained boreal summer surface warming across Greenland and the surrounding high-latitude oceanic regions. It remains a future task to determine if this insolation-driven surface warming alone is sufficient to produce GrIS melt of the magnitude proposed by previous studies (e.g., Alley et al., 2010; Reyes et al., 2014; Robinson et al., 2017). Resolving this question is complicated by the two negative feedback mechanisms we have identified in the atmospheric response to MIS-11 interglacial forcing: (i) a transition in preferred jet stream behavior leading to reductions in poleward eddy heat flux over the Greenland sector, and (ii) increased annual-mean precipitation over the ice sheet. The mass balance implications of these feedbacks will be explored in a planned future ice sheet modelling study.

The preferred boreal summer jet response to MIS-11 forcing identified here, driven by the combined effects of weakened midlatitude baroclinicity and enhanced tropical ascent over the Atlantic sector, is more consistent with the merged-jet state considered to be characteristic of glacials rather than interglacials (e.g., Andres and Tarasov, 2019; Merz et al., 2015). Further study, and comparison with other interglacial climate simulations, may clarify whether this is a unique feature of MIS-11 or typical of strong interglacials. Earlier studies utilizing medium-resolution CCSM3 simulations (Herold et al., 2012; Rachmayani et al., 2016) suggest that an enhanced African monsoon and warmer high-latitude temperatures are typical features of late-Quaternary interglacial states, indicating that at least the primary mechanisms behind the jet changes tend to be present. However, spatial patterns of warming and the degree and duration of monsoon enhancement appear to vary considerably between interglacials, and it therefore remains to be seen whether the dynamic conditions present in other interglacials favor the same northern summer jet configuration.

Data availability. Model data used in the analyses and figures have been uploaded to PANGAEA and will be available by the second half of 2022. Data can also be obtained by contacting the corresponding author.

Author contributions. This research was performed as part of the PhD studies of lead author BRC, advised by authors MP and MS. Both MP and MS provided guidance and feedback on experimental design, furnished computing resources, and extensively discussed the results.

Competing interests. The authors declare no competing interests that impacted the research process or the development of this manuscript.

Acknowledgements. The authors would like to thank the DFG and the ArcTrain program for furnishing funding and computing resources for the research undertaken. We are grateful to the Northern German

Supercomputing Alliance (HLRN) for providing access to their extensive computing resources, enabling the lengthy simulations performed for this research to be done in a timely fashion. Additionally, the lead author would like to thank the Geosystem Modelling group of the University of Bremen for helpful comments and feedback during various presentations of preliminary results. Additional helpful feedback and discussions were provided by Lev Tarasov and Heather Andres of Memorial University, Canada, as well as two anonymous reviewers.

Chapter 4

Uncertainties originating from GCM downscaling and bias correction with application to the MIS-11c Greenland Ice Sheet

Brian R. Crow[1], Lev Tarasov[2], Michael Schulz[1], Matthias Prange[1]

[1]MARUM (Center for Marine Environmental Sciences) and Faculty of Geosciences, University of Bremen, Bremen, 28359, Germany
[2]Department of Physics and Physical Oceanography, Memorial University of Newfoundland and Labrador, St. John's, A1B 3X7, Canada

Manuscript published in Climate of the Past, 2024, (20) 281-296, doi: 10.5194/cp-20-281-2024

Abstract. The Marine Isotope Stage 11c (MIS-11c) interglacial is an enigmatic period characterized by a long duration of relatively weak insolation forcing, but is thought to have been coincident with a large global sea-level rise of 6-13 m. The configuration of the Greenland Ice Sheet during the MIS-11c interglacial highstand is therefore of great interest. Given the constraints of limited data, model-based analysis may be of use but only if model uncertainties are adequately accounted for. A particularly under-addressed issue in coupled climate and ice-sheet modeling is the coupling of surface air temperatures to the ice model. Many studies apply a uniform "lapse rate" accounting for the temperature differences at different altitudes over the ice surface, but this uniformity neglects both regional and seasonal differences in near-surface temperature dependencies on altitude. Herein we provide the first such analysis for MIS-11c Greenland that addresses these uncertainties by comparing one-way coupled Community Earth System Model (CESM) and ice-sheet model results from several different downscaling methodologies.

In our study, a spatially and temporally varying temperature downscaling method produced the greatest success rate in matching the constraints of limited paleodata, and suggests a peak ice volume loss from Greenland during MIS-11c of approximately 50% compared to present day (~3.9 m contribution to sea-level rise). This result is on the lower bound of existing data- and model-based studies, partly as a consequence of the applied one-way coupling methodology that neglects some feedbacks. Additional uncertainties are examined by comparing two different present-day regional climate analyses for bias correction of temperatures and precipitation, a spread of initialization states and times, and different spatial configurations of precipitation bias corrections. No other factor exhibited greater influence over the simulated Greenland ice sheet than the choice of temperature downscaling scheme.

4.1 Introduction

Examining past interglacial climates offers the opportunity to conduct data-based tests of our understanding of ice-climate dynamics and the modeling thereof. With present and near-future warming expected to further accelerate ice loss from the Greenland and Antarctic ice sheets, maximizing our understanding of their behavior under past warm conditions is a necessity. The Marine Isotope Stage 11c (MIS-11c) interglacial, spanning approximately 430 to 395 ka, presents a particularly interesting test case for modelers given evidence of a robust sea-level highstand (i.e., large loss of land-ice mass) despite relatively weak insolation forcing (Dutton et al., 2015; Tzedakis et al., 2022).

The relative contributions of the Greenland and Antarctic ice sheets to sea-level rise during MIS-11c remain poorly constrained, but recent modeling work has proposed plausible peak Greenland-only contributions in the range of 3.9-7.0 m (Robinson et al., 2017). However, the relative importance of various forms of uncertainty are largely unaccounted for in many coupled ice-climate studies, particularly with regards to bias corrections and temperature downscaling. In this study, we therefore illustrate the dependence of a simulated MIS-11c Greenland ice sheet (GrIS) upon the key choices made with regards to the simulated climate forcing and its coupling to an ice model.

One approach for examining the ice-climate interactions through glacial-interglacial cycles is the two-way interactive coupling of Earth system models of intermediate complexity (EMICs) and ice-sheet models, enabling direct feedback of albedo, vegetation, land surface, and elevation changes on climate forcing (e.g., Ganopolski and Calov, 2011; Goelzer et al., 2016; Robinson et al., 2017; Bahadory and Tarasov, 2018). Such coupled setups benefit from being computationally efficient, enabling long runs and often large ensembles of numerous simulations. However, many model components are highly simplified, and they can therefore only reproduce large-scale features of glacial-interglacial cycles. In recent years, more sophisticated but computationally expensive atmosphere-ocean general circulation models (AOGCMs) have also been increasingly used in two-way coupled setups (e.g., Ridley et al., 2005; Helsen et al., 2013; Sommers et al., 2021). Asynchronous acceleration techniques, in which the ice component is run for multiple years to multiple millennia before updated ice and climate states are exchanged via the coupler, are able to reduce the overall simulation time for such setups (e.g., Herrington and Poulsen, 2011; Helsen et al., 2013; Sommers et al., 2021). While future studies should ideally strive towards more fully coupled simulations, AOGCM-based coupled simulations remain very computationally demanding at present, and this effectively precludes the possibility of conducting large ensemble simulations.

One common, computationally simpler alternative involves the one-way (offline) coupling of an AOGCM to an ice-sheet model. Climate forcing is typically calculated using a steady-state present day or other prescribed ice sheet, limiting the direct feedbacks that the melt or growth of the ice sheet would actually have on the climate system (see e.g., Fyke et al., 2018 for a comprehensive overview). For any given lengthier period of interest, a series of several shorter-duration simulations at conditions representative of selected critical time

steps can be run, with the forcing then interpolated to be continuous between these slices (Stone et al., 2013). Such an approach can be useful for simulating conditions spanning full interglacials (e.g., Stone et al., 2013; Milker et al., 2013) or for comparing various interglacials to each other (Herold et al., 2012; Rachmayani et al., 2016; Rachmayani et al., 2017). This time-slice approach is what we have opted for in our study on the basis that it enables us to test a variety of coupling methodologies in a computationally efficient manner.

Regardless of chosen modeling approach, the relatively low-resolution surface temperatures simulated by a climate model must then be downscaled to the higher-resolution ice surface. Dynamical downscaling, which involves running a regional climate model (RCM) over a more limited domain at higher resolution and/or shorter timescales, can help in achieving the spatial resolution necessary to better resolve surface processes critical to ice-sheet mass balance (e.g., Goelzer et al., 2017). Such simulations could even be paired with a time-slice or glacial index approach, enabling the development of continuous higher-resolution climate forcing over an extended period of time (Jouvet et al., 2023). However, this approach introduces significant additional computational expense and invites the specter of compounding biases across the AOGCM and RCM simulations.

The most common approach therefore remains scaling of temperatures to the ice model grid via a lapse rate, or rate of change in temperature with height. Typically this is a prescribed scalar value (e.g., Huybrechts and T'siobbel, 1997, Vizcaíno et al., 2008) or a tunable parametric value (Stone et al., 2010), but neither of these options has a justifiable physical basis. Both methods fail to capture the considerable seasonality and regional variation in lapse rates that has been demonstrated by both in situ measurements and model simulations of temperatures over glaciers and ice sheets (e.g., Gardner et al., 2009; Fausto et al., 2009; Erokhina et al., 2017). The high sensitivity of ice-sheet marginal ablation zones to temperature changes (e.g., Stone et al., 2010), and the control the lapse rate exhibits on the strength of the temperature-elevation feedback, implies a strong need to correctly implement this in model simulations.

The MIS-11c interglacial constitutes a particularly challenging target for a modeling study due to the relative lack of geological constraints on the extent of the ice sheets. Among the limited geological constraints on Greenland's extent dating back to MIS-11c are ice-core samples near Summit and DYE-3. Chemical analysis of silty basal ice and bedrock beneath it from the GISP2 core near Summit have suggested the possibility of some limited ice-free time over the past 2.7 million years (Schaefer et al., 2016), but it is likely that most or all of this time preceded the mid-Pleistocene transition (Bierman et al., 2014; Bierman et al., 2016; Yau et al., 2016a). Most recently, analysis of basal sediment from the Camp Century ice core suggests a complete deglaciation of NW Greenland in MIS-11, placing a lower bound on GrIS sea-level contribution of 1.4 meters (Christ et al., 2023).

Previous model simulations have suggested that the GISP2/Summit region would be among the last places in Greenland to deglaciate even during exceptionally warm stretches (Fyke et al., 2014), suggesting that disappearance of ice at this location would be tantamount to the virtual complete loss of the GrIS. The basal

ice at DYE-3, however, has been dated only to the end of the MIS-11 interglacial, albeit with considerable uncertainties arising from dating techniques and poorly constrained ice advection (Yau et al., 2016a). Thus, directly derived constraints for the minimum extent of the GrIS during MIS-11c include (1) the preservation of ice at Summit and (2) the disappearance of ice at DYE-3.

Additional indirect evidence of GrIS deglaciation in MIS-11c originates from marine sediment cores from a handful of locations off southern Greenland. Spruce pollen found in these samples, considered to be of local origin, indicates the emergence of boreal coniferous forest across at least the lower elevations of southern Greenland sometime around 400 ka. This is roughly during the later stages of MIS-11c and suggestive of considerable retreat of the GrIS ice margin compared to present (Willerslev et al., 2007; de Vernal and Hillaire-Marcel, 2008). Cessation of ice-rafted debris (IRD) deposition along the southern margin for several thousand years during MIS-11c is unprecedented compared to other late Pleistocene interglacials, and indicative of the disappearance of most or all marine-terminating ice in southern Greenland (Reyes et al., 2014). Collectively, this evidence suggests a drastic reduction in the extent of the GrIS but with rather poor constraints on the magnitude, spatial extent, and duration of retreat.

In this study, we present a number of one-way coupled ensemble simulations of the GrIS's evolution throughout its substantial melt event during the MIS-11c interglacial. Using constraints provided by reconstructions, we determine a likely range for the GrIS contribution to sea-level change during MIS-11c. We examine the sensitivity of the simulated GrIS to a range of options, including those that are more observationally and physically justifiable than what has generally been used to date. In particular, we demonstrate that commonly used scalar lapse rates for temperature downscaling perform poorly against our data-based constraints and produce the least GrIS melt in MIS-11c of any tested scheme. Our downscaling techniques, bias-correction schemes, initialization states, and chosen models are all detailed in the following section.

4.2 Methodology

The present study is centered on the one-way coupling of the climate forcing developed in the Community Earth System Model (CESM) v.1.2.2 with the ice dynamics of the Glacial Systems Model (GSM). A one-way coupling methodology (i.e., CESM forcing provided to GSM with no coupling back to CESM) was selected for computational efficiency reasons; namely, iterative CESM topographic corrections between time slices were judged too impractical to implement, some feedbacks would still be lacking compared to full two-way coupling, and running a large ensemble of simulations would not be feasible. Relevant descriptions of the two models and the selection and processing of key input variables follow. The purpose here is to overview the various techniques we utilized as they pertain to the treatment of climate forcing and their coupling to the ice model.

4.2.1 Climate simulations and selected forcing

Our configuration of CESM is a fully coupled general circulation model with atmosphere, ocean, sea ice, land, and runoff components (Hurrell et al., 2013). For the sake of computational feasibility, our climate forcing consists of time-slice simulations every 5 kyr from 423 ka to 398 ka (similar to the Stone et al., 2013 methodology), spanning the MIS-11 interglacial period, and utilizes fixed modern-day ice sheets. Each time slice simulation utilizes temporally appropriate CO_2, CH_4, and N_2O levels derived from ice-core records (Siegenthaler et al., 2005; Lüthi et al., 2008; Otto-Bliesner et al., 2017) along with characteristic orbital parameters calculated based on the orbital solution by Laskar (2004). We assume static modern-day topography and land ice for all simulations, which are conducted at a spatial resolution of 2.5° longitude by 1.9° latitude for the atmosphere. Further details regarding the CESM time-slice simulations can be found in the methodology section of Crow et al. (2022a). Bias corrections are calculated relative to climatologies from the final 100 years of a 400-year simulation under constant present-day (year 2000 CE) conditions.

Among the selected climate forcing variables are monthly mean and standard deviation of 2-meter air temperatures converted to sea level, the atmospheric temperature downscaling lapse rate (described in greater detail in the following sub-section), the mean and standard deviations of zonal (U) and meridional (V) components of wind at a height relevant to orographic precipitation (details follow), the total precipitation, the total surface evaporation and sublimation, and ocean temperatures through approximately the top 600 m. GSM has a much higher spatial resolution than CESM and therefore captures more terrain variation, and its elevation profile is constantly recalculated in accordance with the dynamic ice sheet and lithospheric deformation.

Arrays of U and V winds were constructed utilizing data from various heights in the atmosphere, depending on the terrain profile. The goal was to capture wind direction and velocity at heights that are relevant for the generation of orographic precipitation. Since the majority of moisture transport occurs in the atmospheric boundary layer, our formula considers the wind interpolated to the CESM modeled surface height plus 500 m. Where this altitude lies below the height of the simulated 850 hPa pressure surface (i.e., low-altitude/coastal regions), 850 hPa winds are simply used. The input precipitation field is then adjusted by assuming a proportionality with the vertical velocity that such a wind field would induce, given the slope of the terrain (Bahadory and Tarasov, 2018). This approximates the strong orographic forcing that steep slopes induce on precipitation and partly compensates for the mismatch in ice-sheet model topography and the orographic boundary condition used in the climate model.

Ocean temperatures are extracted at discrete levels through the top 600 m of the ocean column, roughly reflecting the present-day depth of waters along the continental shelf of Greenland. This depth also approximately corresponds to the depth of water that may have contact with marine-terminating outlet glaciers, thus exhibiting a strong influence on sub-shelf melt and calving. The spatial resolution of CESM severely limits its ability to resolve fjord-scale ocean processes, so these temperatures represent only an approximation of the near-ice ocean environment.

All input fields are then linearly interpolated between the MIS-11 time slices. We acknowledge that this is an imperfect method that could fail to capture true peaks and nadirs of surface temperatures as they evolved through the MIS-11 interglacial, as well as the possibility of abrupt and/or nonlinear climate transitions between the time slices. However, these time slices were chosen specifically to correspond to key points in the evolution of orbital forcing (precession minima and maxima, with strategically selected intermediate points), and the interpolation therefore should approximately capture the general evolution of climate through this period.

4.2.2 Temperature downscaling (lapse rate) methodologies

Since our climate simulations assume constant present-day ice and topography, there will be inherent contrasts between the land/ice surface heights in the climate and ice models. In order to address this discrepancy, a realistic vertical lapse rate must be utilized for correcting surface air temperatures to the appropriate elevation. We refer throughout this study to the surface slope lapse rate (henceforth simply "lapse rate"), which is a lapse rate representing the rate at which surface temperatures vary at different surface altitudes. This is distinct from the free-air lapse rate, which represents the change in air temperature with height through the atmosphere. The free-air lapse rate is thus more dependent on atmospheric dynamics and is often disconnected from the near-surface energy balance.

As addressed previously, many modeling studies employ a fixed scalar lapse rate, such as the EISMINT3 standard of 7 K km^{-1} (Huybrechts, 1997) or 6.5 K km^{-1} (e.g., Vizcaíno et al., 2008). Piecewise lapse rates (Huybrechts and de Wolde, 1999) or lapse rates as a tunable parameter (e.g., Stone et al., 2010) have also been used but have no direct physical basis in modeled or observed temperatures. Therefore a prescribed lapse rate introduces a considerable source of error when coupling climate forcing to an ice model. Below, we describe the several different methods we tested in our study (in addition to a standard fixed lapse rate of 6.5 K km^{-1}).

4.2.2.1 Seasonally varying

The next logical step in complexity beyond a spatially and temporally uniform fixed lapse rate is a spatially invariant, seasonally varying lapse rate. Erokhina et al. (2017) utilized AOGCM simulations under preindustrial, early Holocene, and Last Glacial Maximum (LGM) conditions to demonstrate the dependence of the mean surface lapse rate over Greenland on not only the seasonal cycle but also the large-scale climate forcing components (i.e., GHGs and orbital parameters). We adopt a similar methodology to Erokhina et al. (2017), utilizing least-squares regression of 2-meter climatological monthly air temperatures from CESM against the CESM surface elevation, excluding points at elevations of less than 100 meters to eliminate contamination from oceanic grid cells. The slope of the regression line produced by each month's analysis then serves as the lapse rate that applies everywhere in our spatial domain for the given month.

4.2.2.2 Spatially and temporally varying (STV)

Our most sophisticated method is the fully spatially and temporally varying (STV) slope lapse rate scheme, which is defined on a point-by-point basis by examining the surface temperatures at all adjacent grid points. For each of the eight neighboring grid points (N, S, E, W, NW, SW, NE, and SE), the temperature difference is calculated and divided by the elevation difference. For elevation differences of less than 100 m, the lapse rate is set to 7 K km^{-1}, a representative mean slope lapse rate value. This approach ensures that incidental temperature differences across a region with small elevation differences are not inordinately weighted compared to sites of more contrasting altitude. Points with effectively zero elevation difference (e.g., two adjacent sea-level grid cells) are not considered in the calculation. For each grid point, the STV slope lapse rate is the mean of all eligible surrounding slope lapse rates.

In addition, we utilize a version of this method that is spatially smoothed with a radius of three CESM grid points (approx. ~300 km at 70°N latitude). The purpose of the smoothing is to reduce the effects of the poor representation of terrain along the Greenland margin in CESM, minimizing any influence of abrupt gradients resulting from the exclusion of oceanic grid points and reducing the lapse rate gradient between different portions of the ice sheet.

4.2.2.3 Daytime-only STV

Finally, in an effort to account for diurnal cycle impacts, we calculated STV lapse rates based only on daytime 2 m air temperatures. Only a limited 5-year dataset of hourly values was available from each of the MIS-11c CESM simulations, and no hourly data were available from the present-day simulation. The temperature bias corrections utilized for these simulations are therefore based upon the all-hours STV lapse rates. Hourly values corresponding to 6:00 to 18:00 Greenland time were selected, approximately reflecting the window of maximum daily insolation. Differences in lapse rates, and therefore corrected sea-level air temperatures, are minimal during the darker and colder winter and spring months but are substantial during summer and early fall when most ablation is occurring (Stone et al., 2010 similarly utilized a lapse rate based only on summer temperatures).

4.2.3 GSM description

The GSM is a sophisticated thermomechanically coupled continental-scale ice-sheet model that is designed for large ensemble simulations of large ice sheets over glacial cycles (Tarasov et al., in prep.). It utilizes an evolved version of the shallow-shelf/shallow-ice dynamical core (SSA/SIA) from Pollard and DeConto (2012) and Pollard et al. (2015). Simulations herein were run at 0.5° longitude and 0.25° latitude grid resolution. Unique and/or noteworthy components of the GSM include the following:

- a 4 km deep permafrost-resolving bed thermodynamics model that also corrects for seasonal snow cover of ice-free land areas (Tarasov and Peltier, 2007);
- a global visco-elastic glacial isostatic adjustment (GIA) solver, updated from Tarasov and Peltier (1997);

- the orographic downscaling of precipitation using climatological wind fields (Bahadory and Tarasov, 2018);
- and a novel inclusion of shortwave radiation fluxes into a traditional positive degree day (PDD) scheme.

The GSM has been utilized extensively in coupled ice-climate simulations, most commonly in a coupled system involving the Earth system model of intermediate complexity LOVECLIM (Goosse et al., 2010; Bahadory and Tarasov, 2018; Bahadory et al., 2021). It has even been utilized previously to demonstrate the considerable spatial and temporal variability in near-surface lapse rates over large ice sheets and the related dependence of ice volume evolution this causes (Bahadory and Tarasov, 2018). It is therefore well-suited to the needs of this study.

Of further relevance is the recent completion of an approximate history matching (see Tarasov and Goldstein preprint in EGUsphere 2023 for an explanation of history matching) of the last glacial cycle Greenland ice sheet with the GSM (Tarasov et al., in prep.). This thereby provides a sample of GSM history-matched ensemble parameter vectors for which the non-climate forcing components thereof can be used herein.

4.2.4 GSM parameters and boundary conditions

The parameters utilized by GSM to represent the various physical processes within and at the interfaces of the ice, till, and bedrock of the domain are derived from an approximate history-matching routine. This glacial cycle history matching was against deglacial and present-day observed data constraints of the GrIS. This set included relative sea-level records, cosmogenic age constraints, present-day ice thickness and horizontal surface velocities, deep ice-core basal temperatures and the GRIP ice-core borehole temperature profile.

To partly address initialization uncertainties, the history matching simulations were run for two full glacial cycles (beginning around 240 ka). The history matching involved Markov Chain Monte Carlo sampling with Bayesian artificial neural network emulators along with over 10,000 full GSM simulations. A high-variance subset of history matched simulations provided not only the GSM parameter vectors but also the initialization state for the current simulations as described in the next section. Since our analysis uses a high-variance set of parameter vectors that were approximately history matched against deglacial and present-day observational constraints for the GrIS, a further examination of ice-sheet model parameter sensitivity is not conducted here.

With the simulation domain being limited to Greenland and its immediate surroundings, a prescribed eustatic sea level was a required boundary condition. The LR04 sea-level reconstruction (Lisiecki and Raymo, 2005) was employed for this purpose. Finally, GSM utilizes a handful of coupling parameters that modulate the degree to which temperature and precipitation inputs are bias-corrected. The values of these parameters were qualitatively tested to examine the effects of greater or lesser “blending” of input values, and ultimately were all set to utilize heavy bias correction.

4.2.5 Greenland ice sheet initialization

It has already been demonstrated that the ice volume derived from a given ice-climate simulation can be highly dependent on the initial ice topography and thermodynamic state (e.g., Rogozhina et al., 2011). We therefore opted to initialize our simulations from the previously described history-matched simulations of the past two full glacial cycles, which have bed thermal characteristics and bed deformation that are more representative than a steady-state integration from zero or from a present-day state. Our choice of selecting the 11.5 ka time slice from the history matched simulations as the initial state for our MIS 11 simulations was inspired by Raymo and Mitrovica (2012; their figure 1), who presented an overlay of the evolution of the LR04 benthic stack $\delta^{18}O$ (Lisiecki and Raymo, 2005) over 440 to 410 ka and over 30 ka to the present. There is apparent similarity in the timing and magnitude of the transition from glacial to interglacial conditions at the start of MIS-11c and the present interglacial, and on this basis, 11.5 ka was chosen as an analogous point in the most recent glacial-interglacial transition to 423 ka, the start of our available forcing data.

The selected 10-member high-variance history-matched subset already contains a spread in ice volume, distribution, and thermal states at the 11.5 ka point. The initial sea-level equivalent (SLE) ice volumes at 11.5 ka in these simulations have a mean value of 11.1 meters, with a range of 9.2-12.2 meters. For reference, these 10 parameter vectors produce a mean GrIS SLE of 7.7 m at present day, compared to the estimated actual present-day water content of 7.4 m (Morlighem et al., 2017). The slight overestimation of GrIS volume at present-day is a common issue in ice-sheet models. It stems in part from discretization (thus introducing some resolution dependency) and likely in part from uncertainties in subglacial bed topography and regional variations in bed roughness impacting basal drag.

Our initial states are integrated with constant 423 ka forcing for either 500 or 1500 years prior to the 423 ka begin date in order to avoid discontinuities from abrupt forcing changes in the period of interest. This “spinup time” is broadly similar to the approach taken by Mas e Braga and coauthors (2021) for their MIS-11c simulation of Antarctica. Each parameter vector is therefore represented twice in each ensemble, once with each spinup time. We therefore account for not only the inherent ice-state uncertainty in utilizing a variety of ice states associated with different ice model parameter sets but also the uncertainty associated with selecting an analog state from the present interglacial.

4.2.6 Bias correction

The version of CESM utilized in this study is understood to have a cold bias at high latitudes relative to observations and reanalyses, at least in present-day and preindustrial climates (e.g., Wang et al., 2019). This is also evident in our analysis of present-day boreal summer (JJA) mean temperatures adjusted to sea level from the present-day CESM simulation versus two present-day reanalysis datasets (Figure 4-1). Given that unrealistically cold temperatures would be detrimental to accurately capturing the extent of GrIS surface melt in MIS-11c, an anomaly forcing approach was selected. For each time slice, the relative change in simulated temperatures and precipitation between the CESM present-day simulation and each MIS-11 time slice were

calculated. Temperature anomalies are calculated as differences in sea-level-adjusted surface air temperatures, using the lapse rates calculated for each simulation in order to make the adjustment.

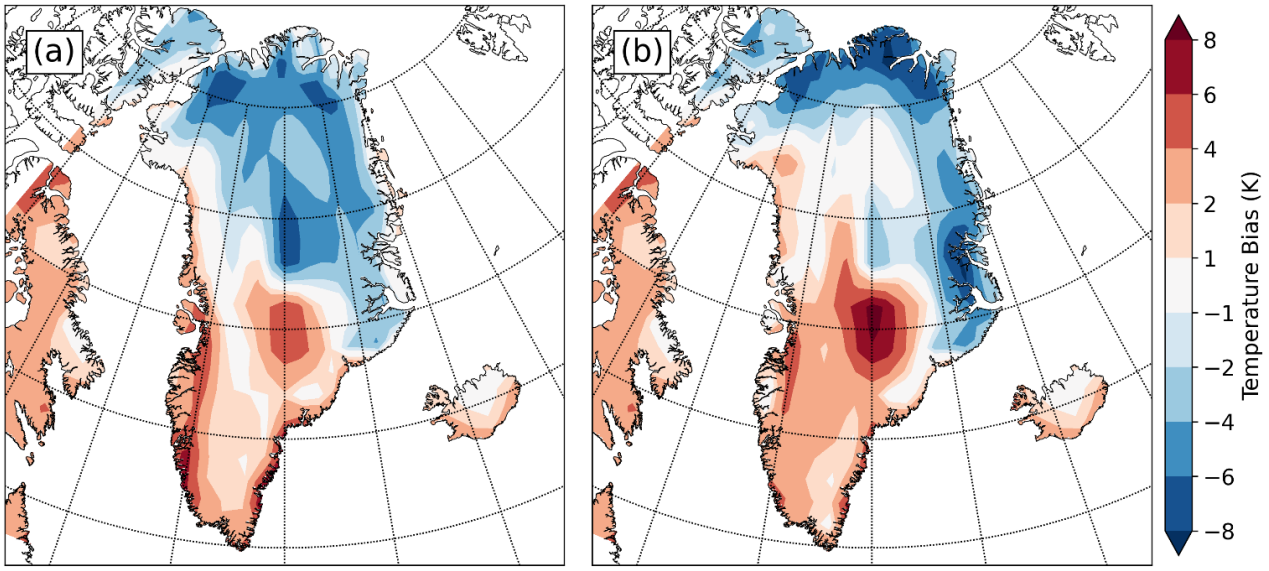

Figure 4-1. Mean June-July-August sea-level converted temperature difference (bias) between present-day CESM climatology and present-day RACMO (a) and between CESM and MAR (b). Red areas indicate where CESM is warmer than reanalyses and blue areas indicate where CESM is colder than reanalyses.

Precipitation bias correction is applied as a monthly varying scale factor over Greenland and the surrounding continental shelf, representing the ratio between the modeled precipitation for a given time slice versus the present-day value. Monthly precipitation climatologies from each time slice are area-weighted across the designated sector and divided by the same quantity from the present-day CESM simulation. By default, only one scaling factor is applied over the entire ice sheet. However, the GSM allows for defining sectors and calculating individual climatological scaling factors for each sector. We therefore tested the effects of using only one precipitation scaling factor against a two-sector north/south division that was established in an effort to address a consistent wet-bias pattern in southern Greenland. In general, the present-day CESM run is much wetter than both the reanalysis datasets around the perimeter of Greenland, and too dry in the center (Figure 4-2). However, south of 69°N, CESM has a large (25-75%) wet bias almost everywhere. This therefore serves as the dividing line in our two-sector precipitation tests. Given the high dependency of precipitation on atmospheric dynamics and the latter's potential sensitivity to changes in boundary conditions, we found the imposition of complete spatial (horizontal) dependence of the bias-correction field hard to justify. Instead, we rely on the orographic downscaling of the GSM to account for the majority of dependency on orography.

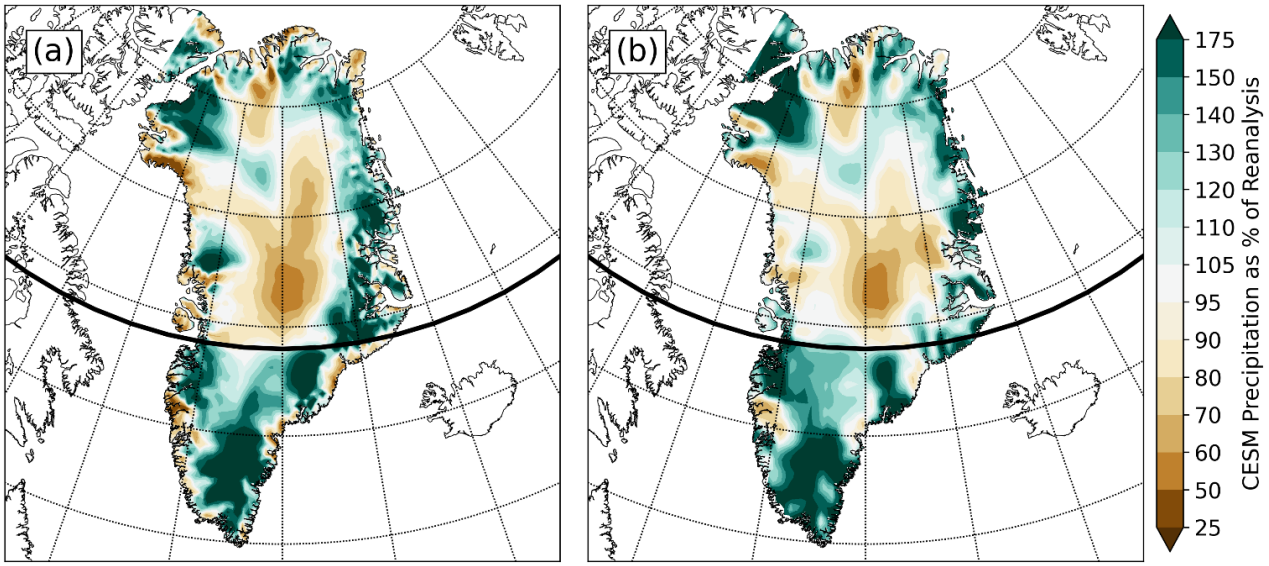

Figure 4-2. Mean annual total precipitation bias ratio of the present-day CESM climatology to RACMO (a) and CESM to MAR (b). Green areas show where CESM is wetter compared to the regional reanalyses, brown where CESM is drier. The bold line of latitude is at 69°N, where the dividing line for two-sector precipitation bias-correction simulations was placed.

Two different present-day regional climate model datasets were utilized as climatological baselines to which CESM anomaly forcing was applied: the Modèle Atmosphérique Régional v3.52 (MAR; Fettweis et al., 2017; Gallée and Schayes, 1994) and the Regional Atmospheric Climate Model v2.3p2 (RACMO; Noël et al., 2018). Both models have been developed specifically for use in polar regions and have been used extensively in ice-sheet modeling studies (e.g., Carter et al., 2022, and references therein). Over Greenland, RACMO is slightly warmer (Figure 4-1) and drier (Figure 4-2) than MAR, leading to notable differences in overall simulated ice volume.

4.3 Results

Numerous ensembles of simulations were conducted utilizing various combinations of the forcing methodologies described above. A summary table (Table 4-1) lists the present-day regional climate analyses to which the CESM anomalies were applied, the number of precipitation bias-correction sectors used, and the lapse rate method employed, as well as three key summary statistics. These are the fraction of ensemble members that preserve ice at the GSM grid cell corresponding to the Summit ice-core site throughout the entire simulation, the fraction of ensemble members that have zero ice depth at some point during the simulated period at the grid cell corresponding to the DYE-3 site, and the mean maximum SLE contribution from the melt of the simulated GrIS, averaged among all ensemble members.

No.	Temperature and precipitation	Precipitation sectors	Lapse rate method	Summit preservation	DYE-3 disappearance	Mean maximum SLE contribution
1	MAR	2	Seasonal	20 / 20	4 / 20	3.27 m
2	RACMO	2	Seasonal	6 / 20	0 / 20	5.07 m
3	MAR	1	STV	14 / 20	18 / 20	3.56 m
4	MAR	2	STV	15 / 20	20 / 20	3.86 m
5	RACMO	1	STV	12 / 20	0 / 20	4.50 m
6	RACMO	2	STV	10 / 20	0 / 20	4.67 m
7	MAR	2	Smoothed	6 / 20	4 / 20	5.60 m
8	RACMO	2	Smoothed	0 / 20	0 / 20	6.42 m
9	MAR	2	Daytime	17 / 20	0 / 20	4.29 m
10	RACMO	2	Daytime	5 / 20	0 / 20	5.00 m
11	MAR	2	Constant	20 / 20	0 / 20	2.20 m

Table 4-1. Summary of the selected forcing datasets and methodologies along with summary statistics for each ensemble. The "Summit preservation" and "DYE-3 disappearance" columns express the fraction of ensemble members (out of 20) that maintain >0 ice depth at Summit throughout the entire simulation and members that achieve ice depth = 0 m at DYE-3 at some point during the simulation, respectively.

The listed ensembles represent just a select subset of all the simulations that were conducted, which also included a number of sensitivity tests and cross-combinations of bias corrections (e.g., MAR temperatures with RACMO precipitation). The focus is primarily on simulations featuring two precipitation sectors (north and south Greenland, divided at 69°N) because these were more successful at meeting our selection criteria, except for ensembles 3 and 5, which were included to illustrate the contrast with ensembles 4 and 6, respectively. Ensemble 11 utilizes a spatially and temporally uniform 6.5 K km^{-1} lapse rate as a reference for the technique most commonly applied in other studies. The constant lapse rate simulations produce the least melt of the GrIS during MIS-11c and none of the 20 ensemble members meet both Summit and DYE-3 criteria.

Two trends are immediately apparent from the table: first, among ensembles utilizing identical lapse rate methodologies, runs forced with anomalies from RACMO data generally produce a greater peak sea-level contribution than those run with MAR (greater melting in MIS-11c associated with RACMO). This can be ascribed to the aforementioned slightly warmer and drier climatology in the RACMO dataset in comparison with MAR. Second, the dual "anchor point" criteria of Summit preservation and DYE-3 disappearance prove difficult to simultaneously replicate, with only a minority of all simulations achieving both. This is not unlike the difficulties Yau et al. (2016a) encountered in trying to simultaneously replicate temperatures at the NEEM and GISP2 core sites. Particularly problematic was achieving the complete melt of DYE-3, which retained ice in the overwhelming majority of all simulations outside of MAR-forced ensembles that utilized the STV lapse rates. This appears to be in part because of high accumulation rates across the South Dome region, causing it

to maintain positive mass balance throughout our simulated MIS-11c despite warmer-than-present temperatures.

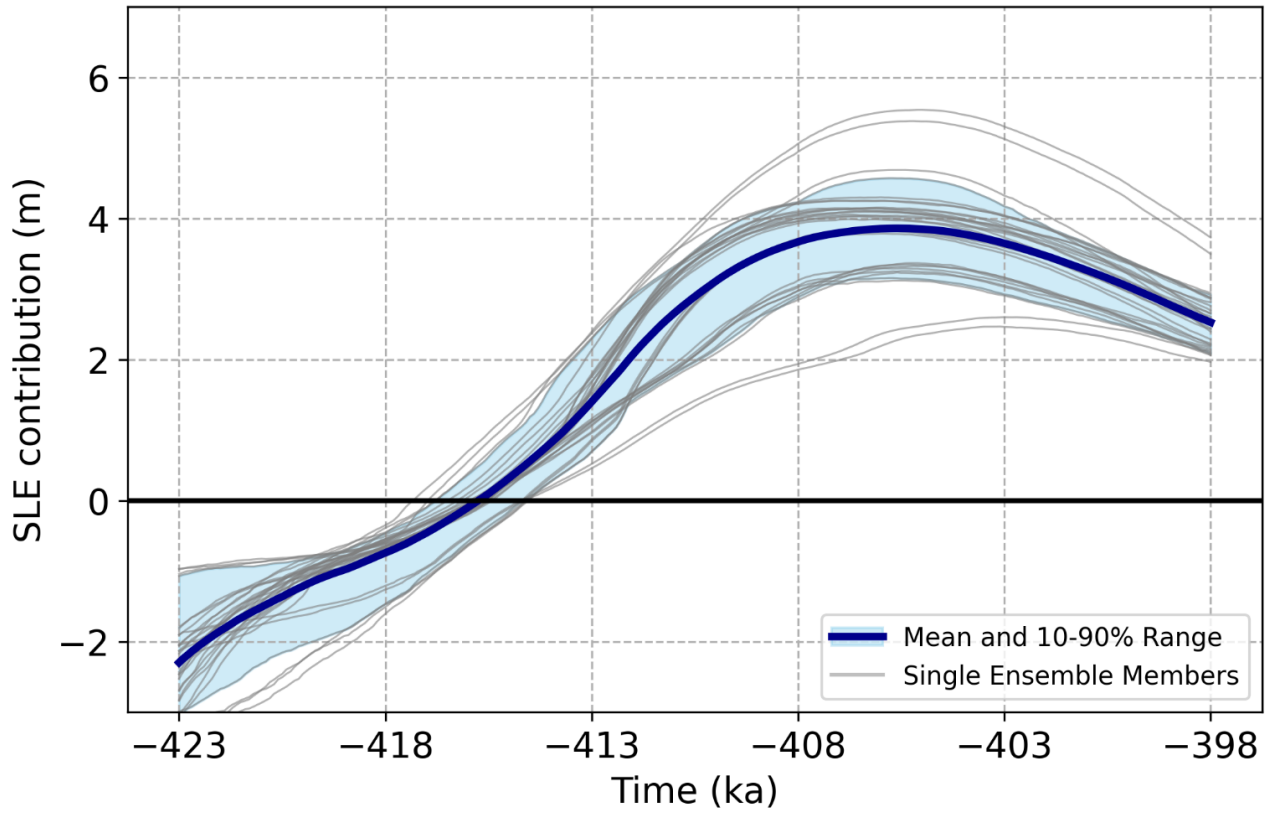

Figure 4-3. Evolution of GrIS contribution to sea level relative to present (0 m line) for all 31 simulations that matched both Summit and DYE-3 conditions through the course of MIS-11c. The thick blue line represents the mean time evolution of volume, while shading gives the 10th to 90th inter-quantile range. Light gray lines show each of the 31 individual member simulations comprising the average.

Across all the listed ensembles, a total of 31 simulations (14.1%) simultaneously met the Summit and DYE-3 criteria, all of which utilized MAR-based temperature and precipitation bias corrections and the large majority of which, 27 out of 31 (87%), used STV lapse rates. The remaining four matched simulations used the seasonally varying lapse rates. These fitting simulations produce a mean peak GrIS SLE contribution of 3.9 m (10-90% range of 3.2-4.6 m) at a mean date of 405.8 ka, the time evolution of which is illustrated in Figure 4-3. This is equivalent to melting approximately 51% (range 41-60%) of the present-day Greenland ice sheet, based on the volume of the ice sheet from the present-day calibration simulations conducted with identical parameter vectors.

In order to better understand the differences incurred by each altered forcing factor, select ensembles are compared directly below. The qualitative and statistical differences between them are discussed here in the context of each differentiating characteristic.

4.3.1 Initialization and spinup time differences

Assessed here are two forms of initialization uncertainty: different ice states stemming from the 11.5 ka realizations of the 10 selected GSM parameter vectors and the different relaxation times to account for the

subjectivity of the 11.5 ka selection. Differences in initialization state clearly have an effect as simulations with a larger beginning ice volume tend to maintain larger ice volumes at their MIS-11c minima (not explicitly shown here but partially recognizable among the individual members in Figure 4-3). The GSM parameters then appear to be the primary driver of the time evolution of volume through the remainder of the simulations, as identical parameter vectors with different spinup times tend to follow nearly identical trends in time.

On the whole, our ensembles exhibit minimal sensitivity to the imposed differences in spinup time. Figure 4-4 illustrates the evolution of two 10-member ensembles utilizing the same 10 GSM parameter vectors and MAR bias corrections. After an initial difference in mean and spread at 423 ka arising purely from the use of a 500-year (blue) or 1500-year (red) spinup time (i.e., constant 423 ka forcing from the beginning of the simulation through 423 ka and starting from either 422.5 or 421.5 ka), the two ensembles quickly converge. Only tiny differences between the ensembles can be observed after 419 ka. This pattern is robust to the choice of bias-correction dataset (MAR or RACMO) and to various lapse rate methodologies, and even holds when examining only our criteria-matched simulations.

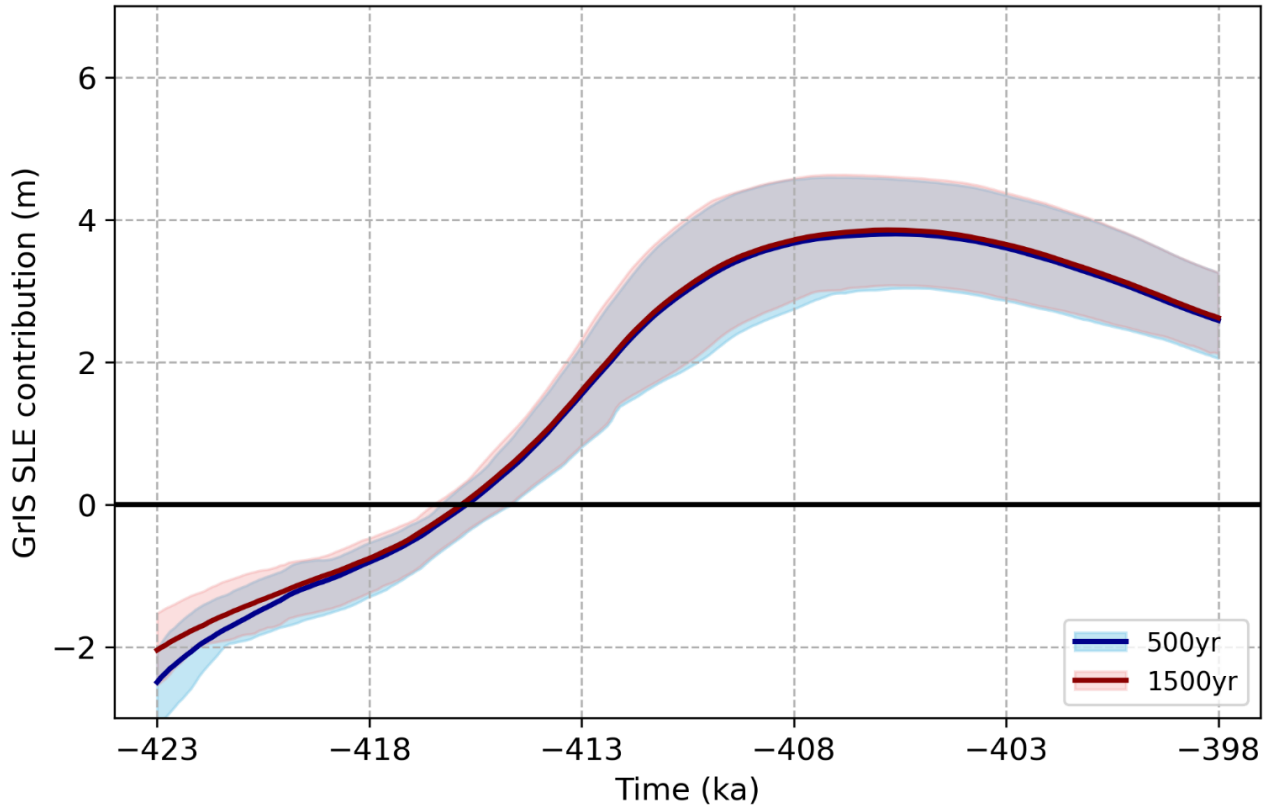

Figure 4-4. Time evolution of sea-level equivalent contribution from Greenland in two ensembles run with identical parameter vectors and forcing but comparing the 500-year (blue) with the 1500-year (red) spinup times. Ensemble means and spreads are practically indistinguishable after 418 ka.

4.3.2 Climate forcing bias corrections

Unlike what we observe with comparing ensembles of different relaxation times, the differences between ensembles using either MAR or RACMO bias corrections are rather stark. Figures 4-5 and 4-6 demonstrate the time evolution of the mean and range of ensembles utilizing the same lapse rate techniques and precipitation

bias-correction sectors, but differentiating in their use of MAR (blue) or RACMO (red) bias corrections. As expected, the differences can be ascribed to the combined effects of the precipitation and surface temperatures on the surface mass balance.

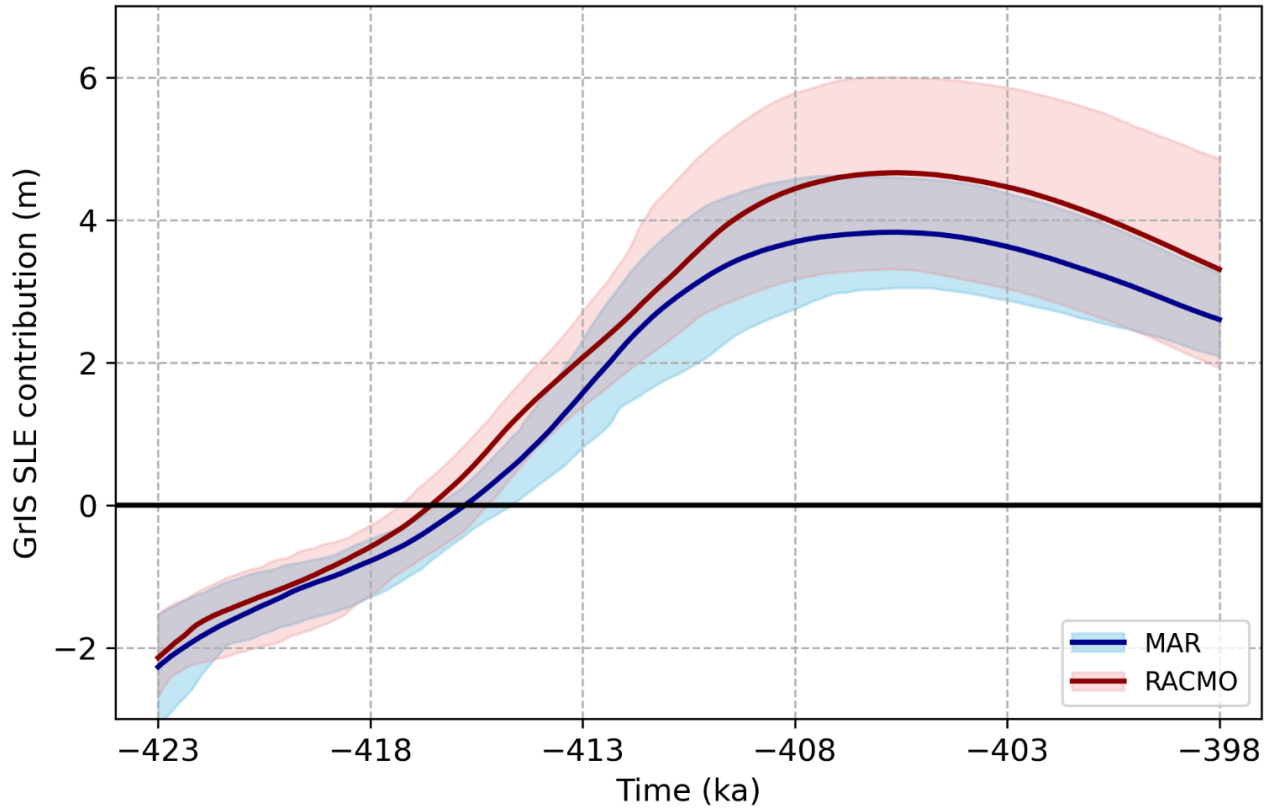

Figure 4-5. Comparison of GrIS sea-level contributions from MAR (blue) and RACMO (red) ensembles utilizing fully varying lapse rates and two precipitation bias-correction sectors. The shading represents the 10-90% range of each ensemble.

A key result is that the melt extent associated with each forcing type also exhibits different sensitivities to different lapse rate techniques. The effects of the different lapse rates will be elaborated on in Section 4.3.4, but here we note the apparent amplification of contrasts between the MAR and RACMO ensembles using seasonally varying lapse rates (Figure 4-6) as opposed to those using STV (Figure 4-5). This sensitivity is a product of multiple factors, including the following:

- the MAR dataset over Greenland is slightly cooler and wetter than RACMO and the spatial patterns of each are slightly different;
- the seasonal cycles of the MAR and RACMO datasets are slightly different;
- the original MAR and RACMO datasets were of slightly different spatial resolution, thus raising the possibility of interpolation differences when both datasets are interpolated to the GSM grid. This could be particularly the case along the steep marginal regions, which in turn exhibit the greatest influence on the size of the ablation zone.

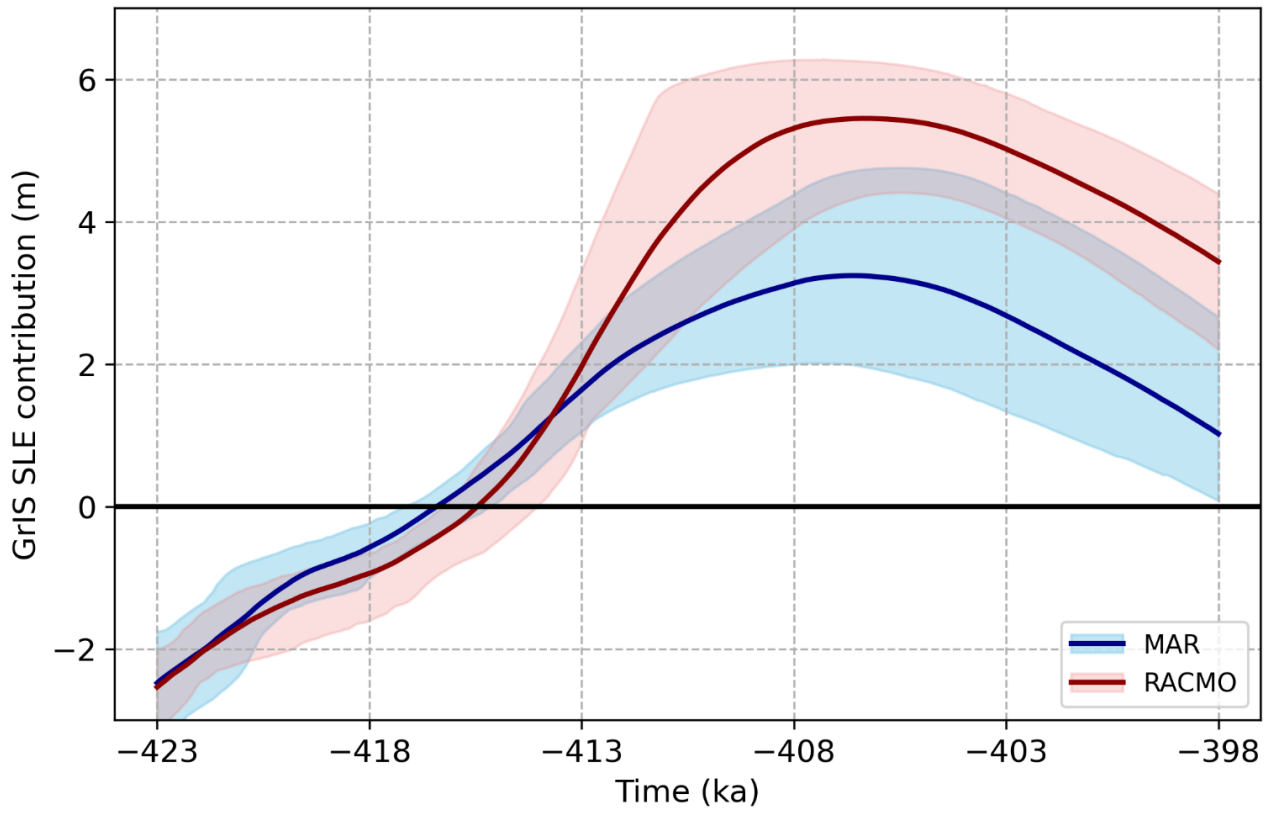

Figure 4-6. As in Figure 4-5 but for seasonally varying lapse rates.

As an example, consider the two simulations depicted in Figure 4-7, which are selected from the ensembles depicted in Figure 4-6. These runs utilize identical parameter vectors, initialization states, relaxation times, and the seasonally varying lapse rate method. Stark contrasts exist in the ice states due to the bias-correction differences, with the peak SLE contribution from the GrIS at around 5.5 m for the RACMO-corrected run and only 3.2 m for the MAR run. As expected, a substantial difference in the ablation zones is apparent; the ablation zone covers virtually the entire northern, western, and central portions of Greenland by 405 ka in the RACMO run, whereas only northern marginal regions and the ice streams in the greater Jakobshavn Isbrae Basin are net ablation zones in the MAR run. Looking at 415 ka surface ice velocities in the simulations offers insight into how this manifests in earlier stages of the ice evolution, with the RACMO run containing greater ice velocities and longer extensions of the ice streams into the interior regions of Greenland. The warmer surface temperatures in the RACMO analysis therefore contribute to a more thermodynamically imbalanced and deformable ice sheet in these simulations in comparison to those bias-corrected with MAR data.

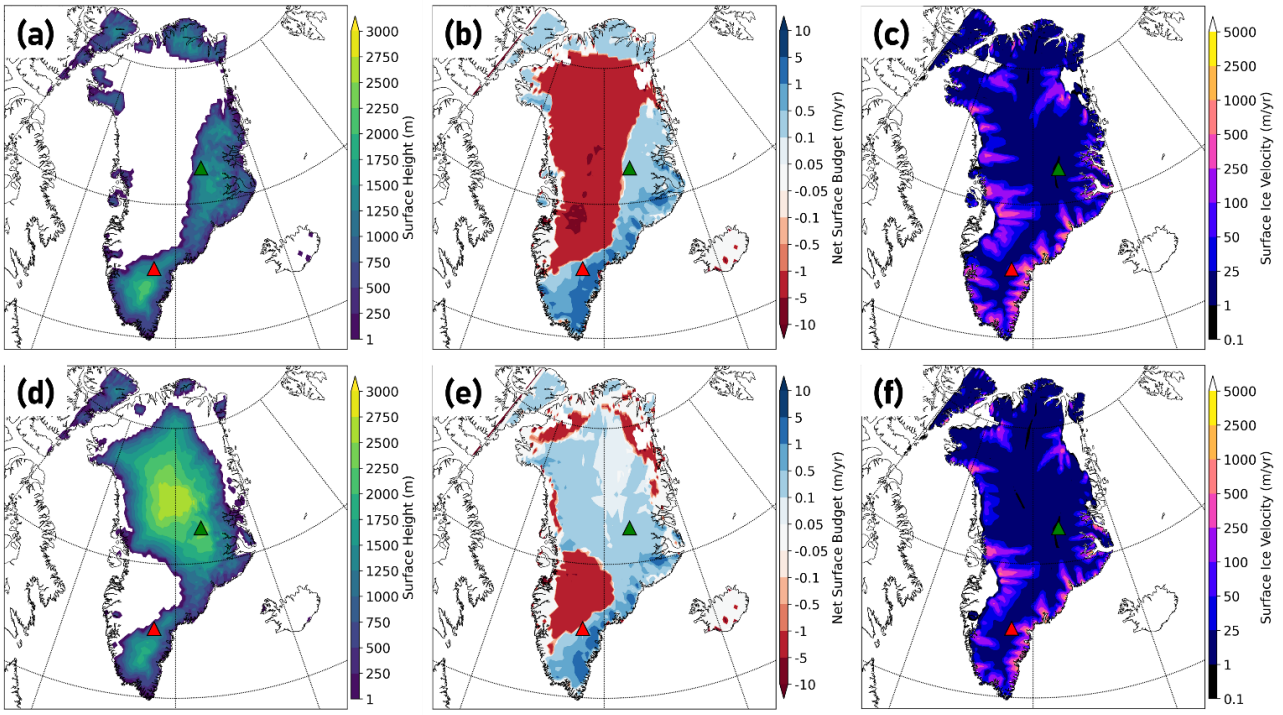

Figure 4-7. Comparison of one model run from each of the ensembles depicted in Figure 4-6 with identical parameter vectors. Top row (a-c): temperatures and precipitation bias-corrected with RACMO data. Bottom row (d-f): bias corrections utilize MAR data. Left column (a and d): ice surface height in meters at 405 ka of the simulation (near ice minimum). Center column (b and e): net surface budget at 405 ka of the simulation, given in net meters per year of surface accumulation (positive, blue shading) or melt (negative, red shading). Right column (c and f): ice surface velocities at 415 ka expressed in meters per year. The locations of the Summit (green triangle) and DYE-3 (red triangle) core sites are depicted in each panel for reference.

4.3.3 Precipitation scaling

The effects of using multiple precipitation bias-correction factors were also examined. As described in Section 4.2.6, the present-day CESM simulation is persistently wetter than both MAR and RACMO south of 69°N, so this division was utilized to enable the calculation of two separate monthly precipitation scaling factors. With all other variables kept constant (forcing type and lapse rate methodology), our simulations produce only minimal differences between the one-sector and two-sector forcing. Shown in Figure 4-8 is the difference between ensembles utilizing MAR forcing and STV lapse rates, with only a slight increase in mean melt contribution seen in the two-sector simulations. Comparisons made between ensembles utilizing RACMO forcing are nearly identical, and thus not shown here.

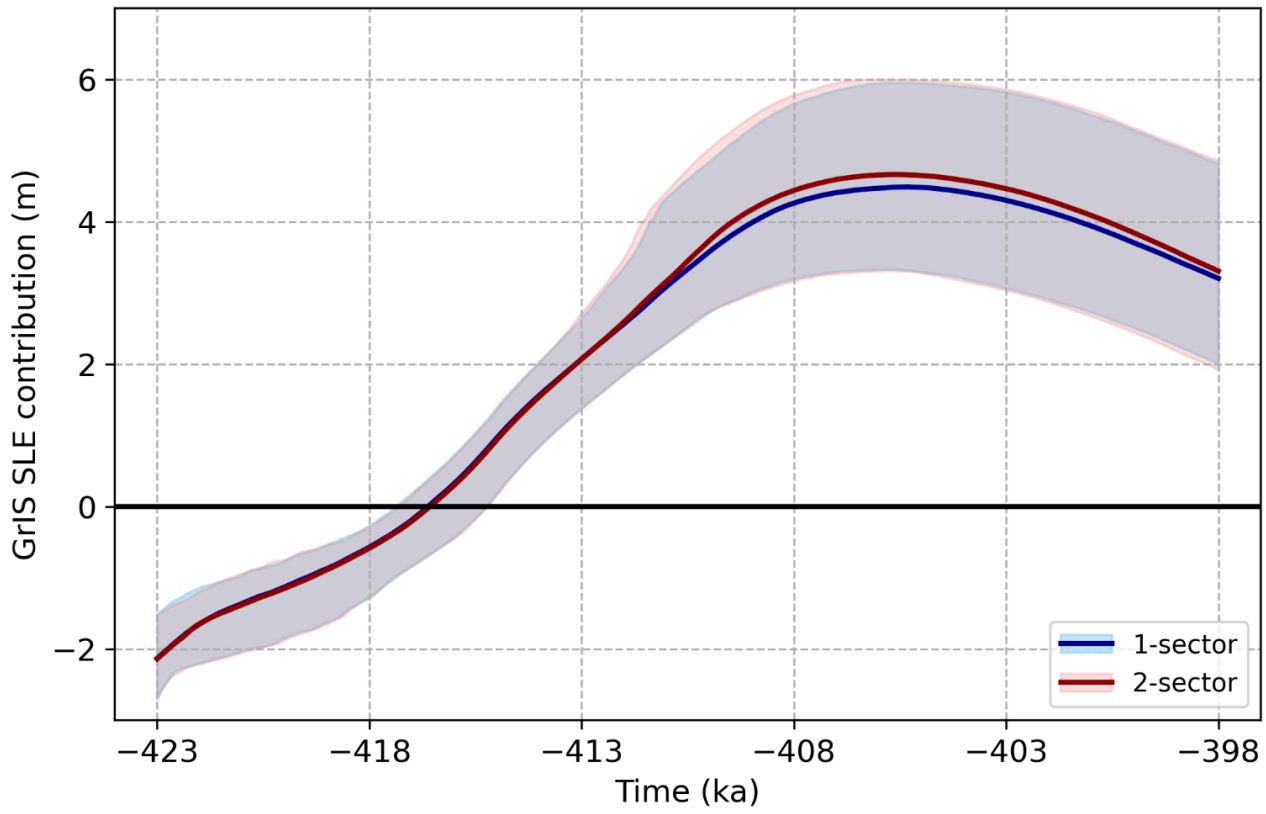

Figure 4-8. Time evolution of sea-level contribution from Greenland from two ensembles with MAR forcing and fully varying lapse rates but using one precipitation scaling factor for the whole GrIS (blue) versus two sectors (red), divided at 69°N.

This increase in sea-level contribution is a result of slightly less positive mass balance from reduced precipitation over the South Dome region. The change also slightly improves our Summit and DYE-3 match rates, improving from 14/20 to 15/20 members preserving Summit and from 18/20 to 20/20 melting DYE-3 when utilizing MAR forcing and STV lapse rates (Table 4-1). While the differences between corresponding simulations in the two ensembles are difficult to see spatially, the small localized changes in surface mass balance ultimately result in improved representations of our key ice-core locations.

4.3.4 Lapse rate methodology comparison

The most impactful forcing difference between simulations was the choice of lapse rate method. As illustrated in Figures 4-9 and 4-10, the resulting peak GrIS sea-level contribution for each lapse rate method is distinctly different, ranging from approximately 2.2 m SLE with a constant 6.5 K km^{-1} lapse rate to approximately 5.6 m SLE with the smoothed spatially and temporally varying method. The uncertainty ranges, characterized by the 10th to 90th percentile of individual members of each ensemble, also vary in magnitude. The STV method provides the narrowest uncertainty range, while the smoothed and daytime methods each span a range of over 3 m SLE around the time of minimum volume.

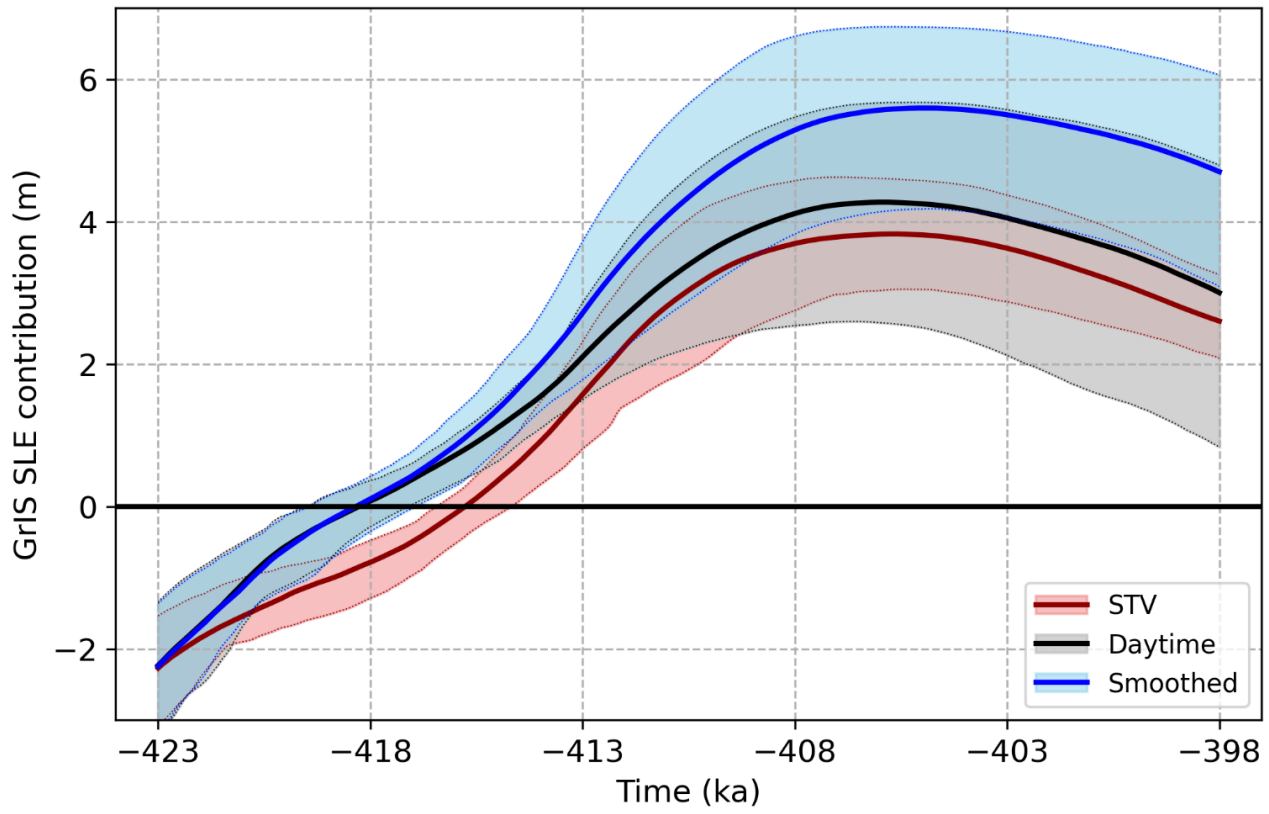

Figure 4-9. Time evolution of ensembles forced with MAR bias corrections, two precipitation sectors, and the STV (red), daytime-only (black/gray), and smoothed (blue) lapse rate methodologies. Shading represents the 10-90% range for each 20-member ensemble, and bold lines give the time-mean evolution of all members in each ensemble.

These differences can be primarily explained by the effect of the lapse rate on the surface mass balance. The fixed lapse rate method appears to result in an underestimation of the ablation zone and is not responsive to changes in orbital forcing, thus limiting the melt extent sharply. The seasonal lapse rate is spatially invariant and therefore has nearly the same limitation as using a fully fixed lapse rate: the higher vertical temperature gradients in coastal/marginal zones are not resolved, reducing the extent of the ablation area. Temperature inversions and persistent marine cloud cover also contribute to very low coastal lapse rates. Orographic flows also result in persistent windward cloudiness along steep terrain gradients, contributing to suppressed lower-atmospheric temperature gradients in these areas. The combined effects of these factors can be identified in the comparison of JJA lapse rates from the 413 ka simulation as calculated via the four methodologies (excluding fixed 6.5 K km^{-1}; Figure 4-11).

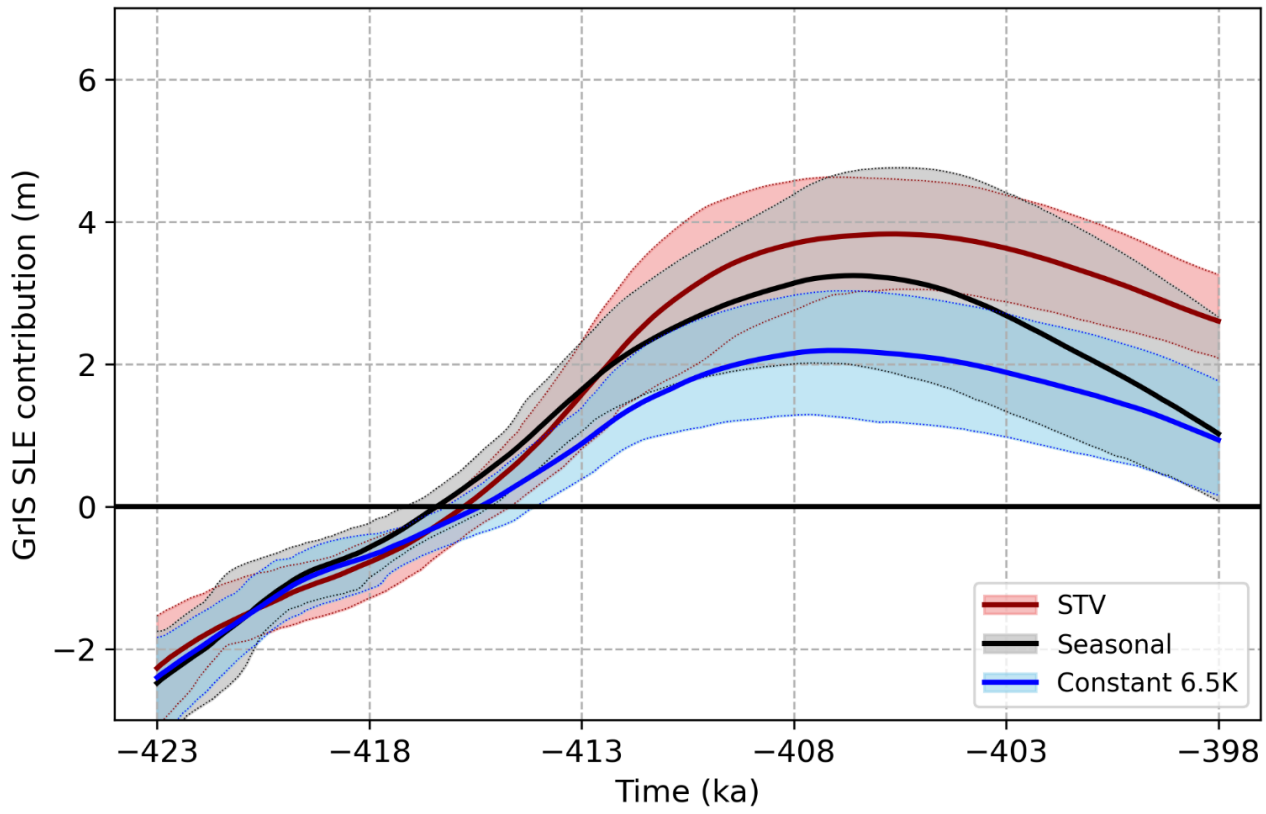

Figure 4-10. As in Figure 4-9 but for comparison of the STV, seasonally varying, and constant 6.5 K km^{-1} lapse rate methods.

On the other end of the spectrum, the smoothed lapse rates result in a likely overestimated ablation zone, as the large lapse rates that generally occur in inland portions of Greenland are artificially broadened into more marginal portions of the ice sheet. The daytime lapse rates are also smoothed in our case to eliminate overly large terrain artifacts and tend to result in greater melt than the standard STV method. Summer-mean daytime lapse rates are actually somewhat lower than all-hours lapse rates due to the exclusion of much more spatially contrasting nighttime temperatures (i.e., comparatively rapid cooling in the brief subarctic summer night over ice-covered regions steepening the vertical temperature contrast compared to neighboring ice-free areas). This has the effect, however, of enabling above-freezing temperatures at higher altitudes when the CESM forcing is downscaled, thus leading to a more expansive ablation zone.

Thus, higher lapse rates do not automatically translate into greater ablation, as increased lapse rates result in cooler simulated conditions over terrain that is higher on the GSM grid than on the CESM grid, helping to preserve high-altitude and central portions of the ice sheet. The interplay between the high, cold interior region and the low, warm marginal region explains much of the very large spread in volumes across individual members of the daytime and smoothed lapse rate ensembles. Small differences in initial ice extent and elevation are amplified throughout the simulations, resulting in the large spread seen in both the daytime and smoothed ensembles. Two sample comparisons of simulations that differ only in their lapse rate methodologies can be found in the supplementary materials (Figures 4-S1 and 4-S2).

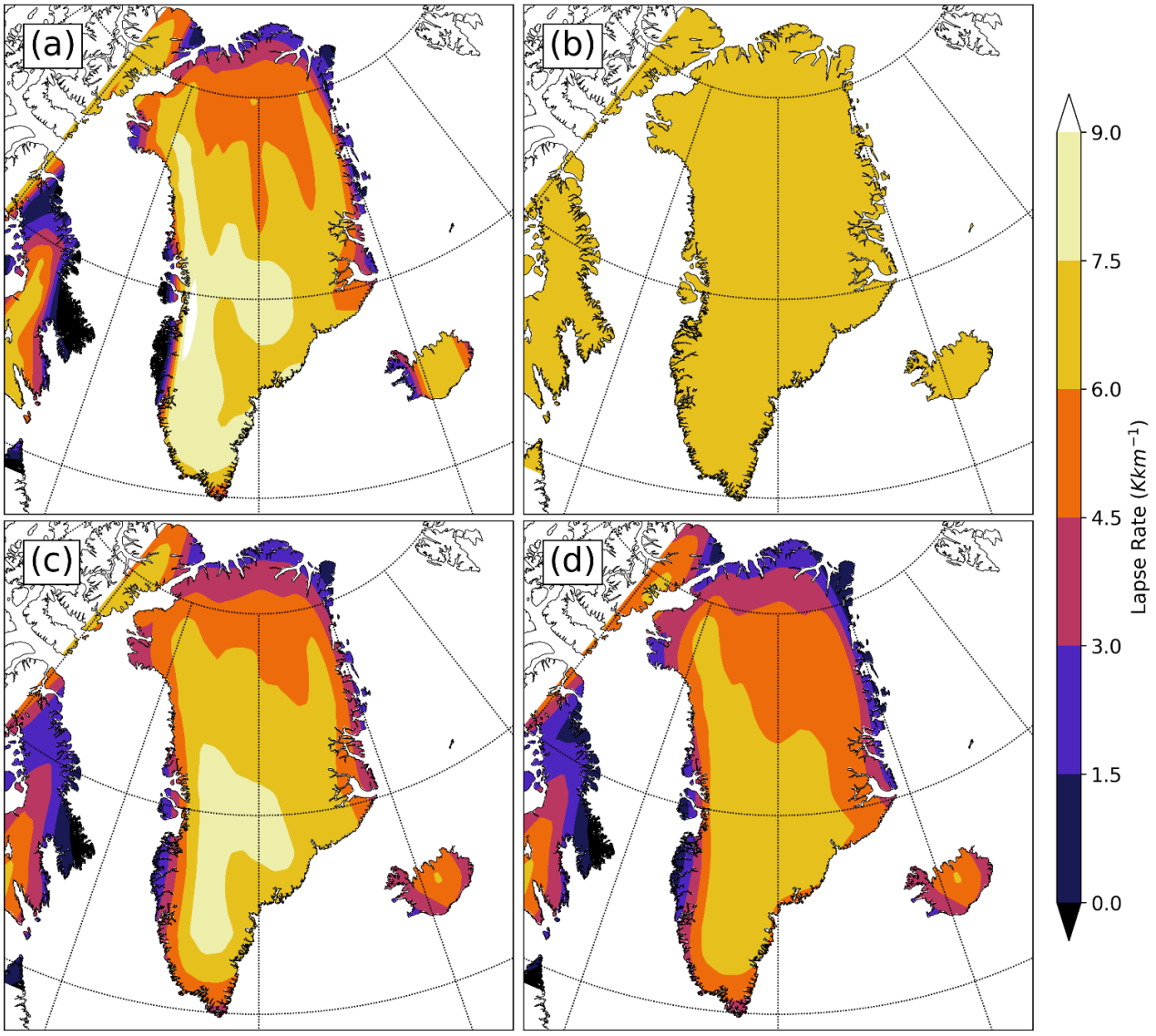

Figure 4-11. Mean June-July-August slope lapse rates calculated with the following techniques: (a) fully spatially and temporally varying, (b) seasonally varying, (c) smoothed STV, and (d) daytime-only STV. All plots are from the 413 ka time slice of CESM and interpolated to the GSM grid.

The STV lapse rate methodology produces the narrowest spread amongst ensemble members. The spatial pattern of the calculated lapse rate is broadly similar for each MIS-11c time slice, reflecting the constancy of the ice margins throughout the fixed-land-ice CESM simulations but with small variations dependent on the orbital forcing changes. This method is the most physically justifiable as it accounts for regional patterns of temperature and lapse rate driven not only by terrain differences but also by differences in regional climate regimes. Consider, for example, the very stormy and subarctic southern reaches of Greenland and the very dry Arctic northern slope of Greenland, which is often characterized by shallow polar high pressure and even temperature inversions (evident in the summer lapse rate plots as an inland extension of lower lapse rates, particularly in the N and NE). Accounting for the presence of such features enables a more physically consistent coupling of temperatures between CESM and the dynamic ice of GSM.

4.4 Discussion

In this study, we have presented an examination of the relative impacts of various sources of uncertainty in coupled ice-climate modeling with specific application to MIS-11c. Though uncertainties associated with numerically approximated ice processes remain and are not directly addressed here (e.g., Goelzer et al., 2017), we have demonstrated that climate forcing and its downscaling is overwhelmingly the dominant influence on our simulated GrIS. Ideally future studies should strive to use fully two-way coupled climate-ice-sheet simulations, thus reducing or eliminating many of these uncertainties. For the time being, however, large ensembles remain a useful tool for uncertainty assessment, and for computational practicality reasons this remains the domain of EMICs and one-way coupled simulations.

Our use of a full AOGCM for climate forcing offers the benefit of sophisticated, relatively high-resolution climate forcing but at the expense of non-interactive, prescribed ice. This in turn means that surface albedo and vegetation feedbacks are missing from our climate forcing, thus impacting the temperature forcing (and to a lesser extent precipitation). The effect of the missing feedbacks on temperature, for example, could be to underestimate the lapse-rate feedback effect (Pritchard et al., 2008). As ice retreats, particularly in marginal and low-elevation zones, the surface albedo will tend to decrease, and the emergence of silty layers and eventually bedrock will result in an altogether radiatively different surface. Additionally, the time-slice methodology allows for the possibility of missing peak climate forcing conditions, which, while unlikely to be very different from the conditions captured in our simulations, could have potentially occurred between chosen time slices. While our time slices were strategically selected to reflect precession minima, maxima, and intermediate points in the precession cycle, the fact that our forcing is not continuous allows for possible underestimation of peak interglacial warmth. The MIS-11c simulations presented here are therefore likely conservative and skew towards the lower bound of possible GrIS melt for this period.

Achieving both filtering criteria simultaneously with our simulations proved difficult, as generally high accumulation rates around DYE-3 often prevented complete melt and high ablation rates at Summit often resulted in elimination of ice there. That our simulations that produced the greatest overall melt of the GrIS in MIS-11 (those utilizing RACMO bias corrections and smoothed lapse rates) had zero success at meeting either criterion illustrates the highly uncertain retreat pattern of the GrIS. By utilizing two separate precipitation bias corrections, one applied to Summit and the other applied to DYE-3, we were able to achieve a modest improvement in meeting these criteria. The two-sector bias-correction factor, in combination with orographic downscaling, remains a simplistic approximation. However, it is unclear what would be an appropriate alternative and as such this is an important target for future work entailing comparisons against RCM results. To the authors' knowledge, no other studies have used such a variable bias correction in their investigations, but it clearly has utility when there are significant regional or sub-regional model biases, which is generally the case for all past and current climate models.

Furthermore, differences in initialization states had only minor impacts on the exact spatial ice distribution of the simulated GrIS but ultimately little impact on its estimated sea-level contribution during MIS-11c. A spinup time lead-in of 500 or 1500 years prior to the beginning of our climate forcing period was also of very minor significance, with runs utilizing identical parameter vectors quickly converging after a few thousand years. This may be contrary to reader expectations given that several studies (e.g., Rogozhina et al., 2011; Aschwanden et al., 2013) have identified initialization states as a key factor in modeled ice sheet outcomes. However, the short (500-year) versus long (1500-year) spinup times represent primarily the uncertainty due to the uncertain choice of simulation start time from the present-day spinup simulations. The other aspects of initialization uncertainty, e.g., differences in initial ice distribution and temperature, are inherently accounted for in the use of multiple parameter vectors and their corresponding initial states. The initial spread between different parameter vectors dominates any minor effects from the short versus long spinup times.

We have also demonstrated that proper coupling and bias correction of near-surface temperatures is of paramount importance to simulating the paleo-GrIS, as it exerts a critical control on surface mass balance. Bias corrections (against higher-quality or higher-resolution datasets) are an optional but very useful means of helping to constrain the uncertainties introduced by utilizing climate forcing from models with known temperature biases or other deficiencies (e.g., Fyke et al., 2011; Ridley et al., 2010). If opting for a bias-corrected or anomaly-forcing method, then selecting baseline datasets that are optimized for polar climates is also advisable (Carter et al., 2022).

Ultimately, nothing exhibited such a great influence over our GrIS simulations as the chosen slope lapse rate technique, for two primary reasons: (1) the dual manifestation of the lapse rate in both the actual temperature forcing applied and the bias corrections and (2) the overwhelming influence of temperatures upon the surface mass budget. The calculated lapse rates influence temperatures twice: first, in the correction of the surface temperatures from CESM to the appropriate ice-surface height as calculated by GSM, and second, in the magnitude of the applied temperature bias correction, as the MAR and RACMO temperatures were themselves converted to sea-level temperature for direct comparison with CESM. Furthermore, temperature downscaling methodology need not be a subjective and arbitrary choice of scalar lapse rate value; rather, we have demonstrated here that data-based and observationally supported alternatives are readily available. We have found a data-based spatially and temporally varying lapse rate to be the optimal solution.

4.5 Conclusions and outlook

This study was conducted with the dual goals of (1) offering additional constraints on the GrIS contribution to sea-level rise during the MIS-11c interglacial and (2) addressing the previously under-examined influence of bias correction and coupling of climate forcing on simulated ice sheets. In particular, we have emphasized the impact of the choice of methodology by which surface temperatures are downscaled from the climate model to the dynamic ice surface in the ice model, demonstrating that it has a dominant effect on the simulated ice sheet.

To the first point, we have found that the minimum volume of the GrIS during MIS-11c was likely slightly less than half of its present-day value. Our simulations matching the criteria of (1) Summit preservation and (2) DYE-3 melt resulted in a mean maximum contribution to the MIS-11c sea-level highstand of 3.9 m from the GrIS, peaking around 405.8 ka. The uncertainty range defined by the middle 80% of matched simulations is an SLE contribution of 3.2-4.6 m. This estimate, which is likely somewhat conservative, is on the low side of existing estimates. Qualitative estimates based on paleodata have suggested a GrIS contribution of 4.5 to 6.0 m of sea-level rise in MIS-11c (Reyes et al., 2014).

Somewhat more comparable is the modeling study of Robinson et al. (2017), which utilized the same two constraining criteria for filtering simulations (preservation of ice at Summit and complete melt at DYE-3). However, their REMBO climate model is a vertically integrated energy balance model (Robinson et al., 2010) and therefore lacks any atmospheric dynamics. Furthermore, they use a scalar 6.5 K km^{-1} lapse rate for temperature-elevation corrections (Robinson et al., 2010). Their ensemble simulations produced a contribution estimate of 3.9 to 7.0 m of sea-level rise but without accounting for the potential uncertainties introduced by the scalar lapse rate or those from the highly simplified climate model. Some of the discrepancy can likely be explained by the fact that their simulations produce a greater duration of melt conditions, with the peak mean SLE contribution occurring approximately 3 kyr later than ours (402.8 ka). While the overall temperature anomalies around Greenland are similar between the studies (Figure 1d in Crow et al., 2022a), the temperatures interpolated between CESM runs appear to be somewhat lower than those from REMBO in the Robinson study in the 408-398 ka period, thus enabling more late-interglacial melt in the latter.

The strong dependence of the Greenland ice sheet produced by each simulation on the chosen lapse rate methodology for vertical downscaling of 2 m air temperature highlights the importance of this often-neglected source of uncertainty in coupled ice-climate modeling. Our simulations utilizing the common but observationally and physically unjustifiable choice of a scalar lapse rate (in our case 6.5 K km^{-1}) produce the least melt of any of the temperature downscaling methodologies presented here. Constant lapse rates, and even seasonally varying but spatially uniform lapse rates, fail to capture critical differences in regional climate conditions and therefore underestimate the extent of marginal ablation regions. In contrast, a spatially and temporally varying lapse rate, calculated from the climate model temperature and elevation data, can capture the seasonal cycle and regional climate differences in a physically realistic (albeit subject to model biases) way. Further improvements to the scheme presented here could be made by utilizing climate simulations with fully interactive ice sheets (whether via online or offline asynchronous coupling). Future modeling studies should strongly consider implementation of similar coupling methodologies in order to avoid further compounding errors inherent to climate models.

Data availability. Data and analysis code can be obtained by contacting the corresponding author, and an upload of related data is planned for early 2024.

Author contributions. This research was performed as part of the PhD studies of lead author Brian Crow, who is advised by authors Matthias Prange, Michael Schulz, and Lev Tarasov. BC carried out climate model simulations with advice and code contributions from MP and experimental design input from MP and MS. The experimental design for ice-sheet model simulations was developed by LT and BC. Ice-sheet model simulations were carried out by LT. All analysis and figure creation were conducted by BC.

Competing interests. Authors L. Tarasov and M. Prange are members of the editorial board of the Icy Landscapes of the Past special joint issue of Climate of the Past, The Cryosphere, Earth System Science Data, and Earth Surface Dynamics. The peer-review process was guided by an independent editor, and the authors have no other competing interests to disclose.

Acknowledgements. The authors would like to thank the Deutsche Forschungsgemeinschaft (DFG) and the Natural Sciences and Engineering Research Council of Canada (NSERC) for furnishing funding for this research via the ArcTrain International Research Training Group. For providing climatological outputs from the present-day CESM run referenced in this study, we wish to express our gratitude to Ute Merkel of the University of Bremen. We are grateful to both the Northern German Supercomputing Alliance (HLRN) and Digital Research Alliance of Canada/ACENET for access to their computing resources for the climate and ice simulations in this study, respectively. This study also contributes to the DFG Cluster of Excellence EXC-2077 – 390741603 and the PalMod German Climate Modeling Initiative. Thanks are also due to our two anonymous reviewers, whose suggestions improved the article materially.

4.6 Supplement to Chapter 4

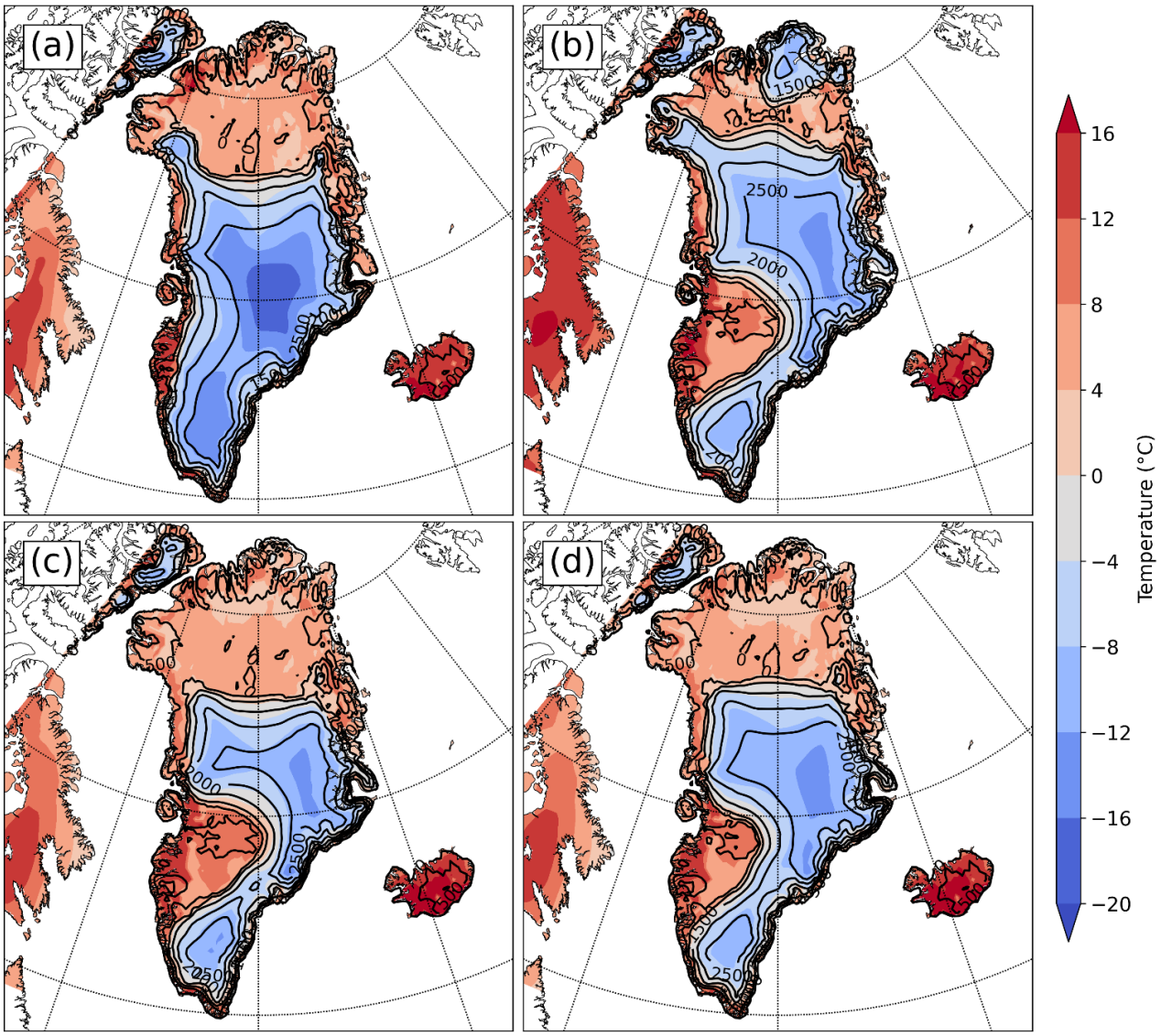

Figure 4-S1. Comparison of 2-meter JJA mean air temperatures at 413 ka for four different GSM simulations with the RACMO temperature baseline. The simulations utilize identical parameters and forcing, except for the choice of surface slope-lapse rate technique. Methodologies utilized are as follows: (a) fully spatially and temporally varying (STV), (b) seasonally varying but spatially fixed, (c) spatially smoothed STV, and (d) daytime-only STV. Surface elevation (bed elevation plus ice surface height) in 500-meter increments is shown in black contours.

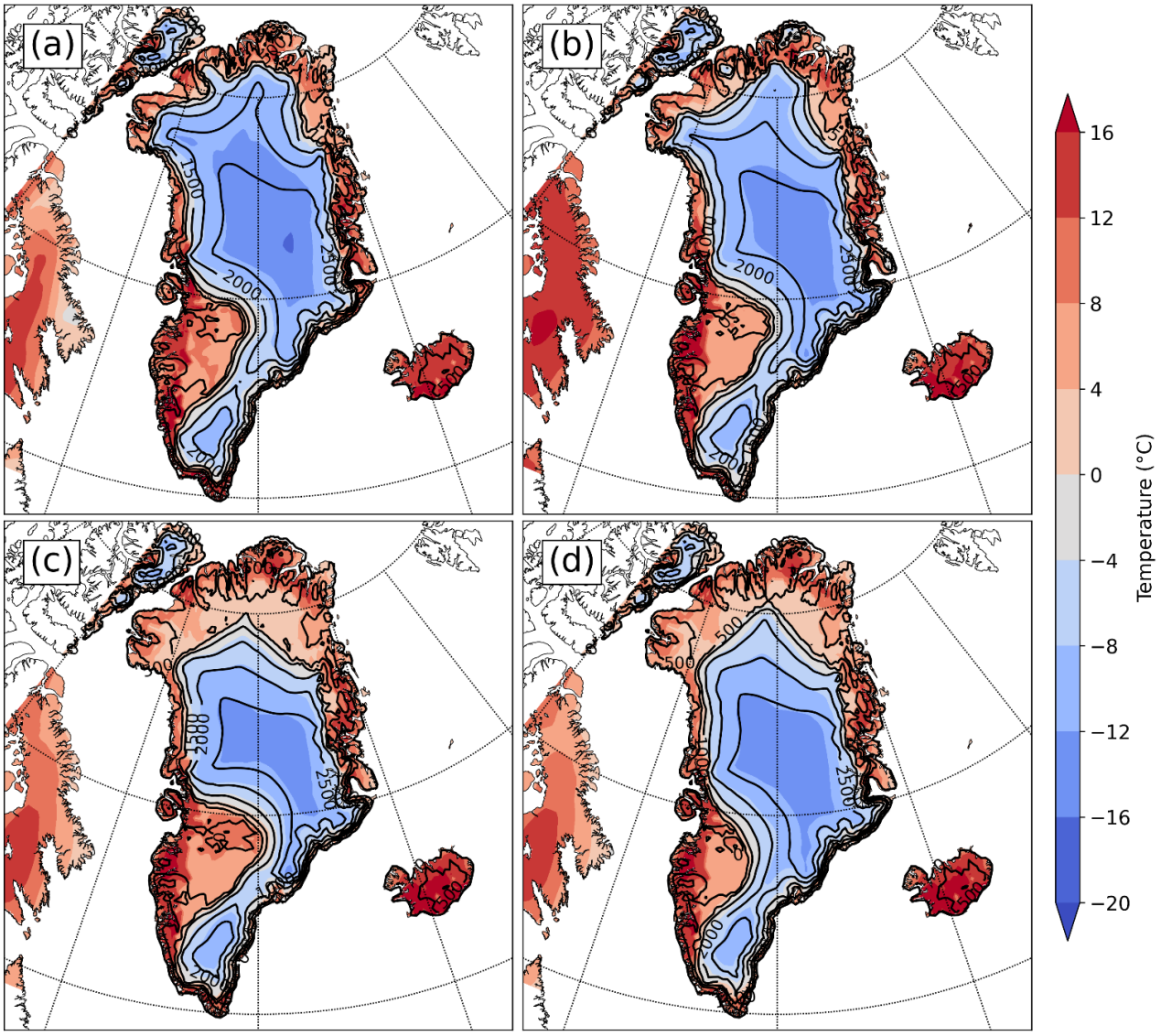

Figure 4-S2. As in Figure 4-S1, but utilizing four different simulations utilizing temperatures based on the MAR dataset.

The supplementary figures here serve to illustrate how strongly dependent our GSM simulations were on the choice of lapse rate methodology. Each set of simulations shown in Figures 4-S1 and 4-S2 utilize identical GSM parameter sets and precipitation data with bias corrections. However, each of the four displayed simulations uses one of the different lapse rate methodologies defined in the main manuscript. Each lapse rate has an effect on the outcome in two ways: firstly, it is used for the calculation of temperature biases between CESM and the choice of present-day baseline (RACMO or MAR), as both datasets are converted to sea level for a one-to-one comparison. Secondly, the same lapse rate is used to correct the input temperature field to the height of the land/ice surface as it appears in the GSM. The choice of lapse rate alone leads to amplifications in the simulated melt pattern of the Greenland ice sheet and can even affect which regions become completely ice-free.

Chapter 5

Arctic sea-ice cover during the Last Interglacial and MIS-11: Long-term and short-term variability

Brian R. Crow[1] and Matthias Prange[1]

[1]MARUM (Center for Marine Environmental Sciences) and Faculty of Geosciences, University of Bremen, Bremen, 28359, Germany

Manuscript in preparation for publication.

Abstract. Sea-ice free summers in the Arctic are expected within the next few decades as a consequence of anthropogenic global warming. While probably unprecedented in the current interglacial, examining past interglacials with warmer-than-present conditions can provide insights into how the Arctic climate system behaves under such a regime. Here we employ CESM simulations of the MIS-5e and MIS-11c interglacials, both of which had peak temperatures and sea levels above those of the preindustrial. Summer Arctic sea-ice levels throughout both interglacials are driven overwhelmingly by an inverse relationship with integrated summer energy, which is very high in early MIS-5e (127 ka) and decreases rapidly, while varying more modestly around a peak near 413 ka in MIS-11c. Simulations of MIS-5e are in general agreement with limited biomarker proxy data from Arctic sediment cores that a brief period of seasonally ice-free conditions occurred across virtually the entire Arctic in MIS-5e, most likely around 127 ka. Summer sea-ice area in MIS-11c decreased more modestly but was still well below preindustrial levels, particularly from 413 to 408 ka, again strongly related to ISE and with no apparent relationship with the Atlantic Meridional Overturning Circulation. Furthermore, it is established that the interannual variability in summer sea ice has a strong relationship with the sea-ice area itself. Intermediate levels of summer sea ice are associated with the highest levels of interannual variability due to the distribution of low to moderate concentrations of ice across the open Arctic. In contrast, both very high and very low levels of summer ice are geographically constrained and therefore exhibit the least interannual variability. Understanding these intermediate- and low-Arctic sea-ice regimes is of great importance as the Arctic transitions toward similar states in the immediate future.

5.1 Introduction

Sea ice is a crucial component of the Arctic climate system, exerting a highly dynamic and highly seasonal influence over the energy balance, atmospheric and oceanic circulation patterns as well as biological and biogeochemical processes. In the present day, the rapid reduction in summer sea-ice area and the associated positive feedbacks are a source of tremendous concern. In particular, sea-ice loss plays a key role in "Arctic amplification" through its effects on surface albedo, surface heat fluxes and longwave radiation (e.g., Serreze and Francis, 2006; Dai et al., 2019). However, such feedback processes are certainly not unique to the present day. Previous interglacial periods, characterized by relative warmth and low global land ice volume compared to the glacial periods that have dominated the past 800,000 years, likely also saw corresponding reductions in global sea-ice area. Due to the limited quality and quantity of proxy records, it remains difficult to assess the magnitude or timing of any such changes in Earth's history. Given persistent indications from both proxies and models that summer Arctic temperatures were considerably warmer than present day for at least brief periods during the Last Interglacial (ca. 130,000-115,000 years ago; also referred to as Marine Isotope Stage 5e, or MIS-5e) and the MIS-11c interglacial (ca. 425,000-395,000 years ago), it is very likely that large reductions in Arctic sea-ice extent also occurred during these periods. Noteworthy is also the fact that idealized modeling and some marine sediment core evidence suggests a role for sea-ice changes in helping to constrain the timing of glacial/interglacial transitions (e.g., Gildor and Tziperman, 2001; Allen et al., 2011), lending an element of criticality to understanding sea-ice changes in these periods.

The primary control mechanisms for the warmth and duration of the MIS-5e and MIS-11c interglacials include differences in greenhouse gas (GHG) levels and the Earth's orbital parameters. MIS-5e was characterized by a highly eccentric orbit, leading to an amplified seasonal cycle featuring a shortened but intensified boreal summer compared to preindustrial. MIS-11c, on the other hand, had much lower-amplitude insolation changes and maintained relatively warm conditions across almost two precessional cycles, something which appears to be unique among the last eight glacial-interglacial cycles (e.g., PAGES, 2015; Tzedakis et al., 2022). Consistently high GHG levels helped maintain warm conditions throughout a long period of this interglacial (e.g., Rachmayani et al., 2017; Tzedakis et al., 2022).

The specifics of the climate forcing mechanisms at work during the MIS-5e and MIS-11c interglacials notwithstanding, the overall dominant driver of Arctic climate is expected to be insolation levels. A frequently used metric for the intensity of insolation forcing between glacial cycles is 21 June (summer solstice) top-of-atmosphere insolation at 65°N, which is representative for high northern latitudes. However, this fails to consider the relation between seasonal intensity and length. According to Kepler's second law, the Earth's distance from the sun is inversely proportional to its angular velocity, which implies that summer intensity and duration counterbalance one another (Huybers, 2006). A more all-encompassing metric for insolation forcing is the integrated summer energy (ISE; Huybers, 2006; Huybers and Tziperman, 2008), a metric which integrates the insolation over all days exceeding a given insolation threshold throughout the year. This concept has thus far seen limited application to Arctic sea-ice levels, with Hillaire-Marcel et al. (2021) using it to

suggest some interglacials may have achieved sufficient whole-summer insolation levels for ice-free summers, and others not (among them MIS-11c).

Evidence for a nearly sea ice-free summer in the Arctic is, as suggested by Hillaire-Marcel et al. (2021), quite limited for the MIS-11c interglacial, despite evidence that a higher sea level was achieved (e.g., Dutton et al., 2015) and that a much greater portion of the Greenland ice sheet melted (e.g., Reyes et al., 2014; Rachmayani et al., 2017). In contrast, the earlier study of Cronin et al. (2013) argued for MIS-11 likely being the last interglacial period in which seasonal sea-ice conditions predominated before becoming fully perennial in the central Arctic for the remainder of the Pleistocene. Thus, the limited sea-ice proxy data available for the Arctic dating back to MIS-11c is still highly uncertain and open to interpretation.

Somewhat better understood are the Arctic sea-ice conditions that predominated during MIS-5e. Multiple LIG simulations from the Climate Model Intercomparison Project 6 (CMIP6) suggest large reductions in summer Arctic sea ice. The multi-model mean minimum simulated sea ice area reduces from 6.46 x 10^6 km^2 in the preindustrial climate to 3.20 x 10^6 km^2 during the LIG, with a few models indicating a near-complete loss of summer sea ice (Kageyama et al., 2021). Another model-proxy data comparison study correlated the modeled Arctic summer temperature and ice area changes across numerous models and compared those that best match the proxy temperature estimates (approx. 4.5 +/- 1.7 K compared to preindustrial), suggesting an approximately three-quarters loss of summer Arctic sea ice in MIS-5e compared to preindustrial (Sime et al., 2023). Examination of biomarkers contained within sediment cores from the high Arctic Ocean also suggest that spring/summer sea-ice concentrations of less than 20% were likely for a timespan during MIS-5e, though limited temporal resolution hinders assigning an exact timeframe (Stein et al., 2017).

The present paper investigates Arctic sea-ice variability on long-term (multi-millennial) and short-term (interannual) time scales during the interglacials of MIS-5e and MIS-11c as simulated by the coupled climate model CESM1.2. In particular, the following questions are addressed: If MIS-5e and/or MIS-11c did experience seasonally ice-free conditions, when and for how long might they have occurred? What is the main driver of multi-millennial sea-ice variability during the interglacials? How does interannual variability of the Arctic sea-ice cover depend on the mean state? In addressing these questions, we attempt to take steps towards understanding the various sea-ice regimes that can emerge under different forcing conditions in the Arctic.

5.2 Methodology

The basis of this study is the analysis of several CESM v1.2.2 time-slice simulations (Hurrell et al., 2013), described extensively already in the Methodology chapter of this dissertation and in the publication constituting Chapter 3 (Crow et al., 2022a). Briefly summarized, the time-slice methodology is employed, utilizing 1000-year long simulations at constant forcing conditions defined by representative greenhouse gas and orbital forcing for the selected time. All presented results are climatologies or time series produced from the final 100 years of these simulations, enabling quasi-equilibrium of all elements of the climate system except for the deep oceans. Given anomalies are presented relative to a preindustrial control simulation, run to PMIP4

standards for 1850 CE conditions (Otto-Bliesner et al., 2017). However, direct comparison with preindustrial climatologies becomes problematic for the very different orbital configurations experienced during MIS-5e. MIS-11c bears some notable similarities to present, with relatively low eccentricity and similarly distributed seasons. In contrast, MIS-5e's highly eccentric orbit skews the relative lengths of seasons in comparison to today. Calendar-adjustments of output data are therefore necessary, and will be described in section 5.2.1.

Perhaps the most limiting assumption employed in our simulations is the use of present-day topography, sea level, and ice-sheet configurations. Meltwater from the Greenland ice sheet is not considered either. However, this model configuration does utilize the sea-ice model CICE4, which contains an explicit melt-pond scheme. In multi-model and proxy comparison studies, this has been shown to produce much greater loss of sea ice than for models that lack this feature (e.g., Diamond et al., 2021; Sime et al., 2023) and is arguably more realistic due to the degree of summer sea-ice melt that is driven by melt ponds (e.g., Perovich et al., 2002).

5.2.1 Calendar-correction of MIS-5 data

The calendar problem for comparing monthly or seasonal climatologies from paleo-datasets or model simulations has long been recognized (e.g., Joussaume and Braconnot, 1997; Bartlein and Shafer, 2019). As described more extensively in the Methods chapter, an angular calendar is a more appropriate choice for comparing climatologies across eras in which orbital arrangements significantly differed. We therefore utilize for this purpose the PaleoCalAdjust Fortran program published by Bartlein and Shafer (2019).

This program recalculates the new start and end dates of all months in today's calendar based on the orbital conditions of the past. As an example, "January" from the 127 ka simulation is calculated as the orbital equivalent of 27 December-27 January based on today's calendar. The monthly data from the simulation is by default naively timestamped using an invariable modern 365-day calendar. It therefore must be deconstructed into quasi-daily values, interpolated, and re-aggregated to reflect the appropriate date range. All MIS-5e simulations are therefore subjected to this treatment to remove prominent "calendar effects" that would otherwise contaminate seasonal averages (e.g., Pollard and Reusch, 2002; Bartlein and Shafer, 2019).

5.3 Results

5.3.1 Sea-ice area seasonality in the two interglacials

The climatological annual cycles in total Arctic sea-ice area for the various time slices of MIS-5e and MIS-11c are shown in Figure 5-1. Particularly large variations in sea-ice area are apparent during the minimum ice-area months of August-September-October. With a total sea-ice area of much less than 1 million square kilometers, September reaches ice-free conditions at 127 ka. At 124 ka, the sea-ice area remains much lower than during preindustrial. All later time slices of MIS-5e show summer ice areas larger than preindustrial. For MIS-11c, minimum ice conditions of ~1.8 million square kilometers are reached at 413 ka, but only the latest time slice (403 ka) shows a larger-than-preindustrial Arctic sea-ice area.

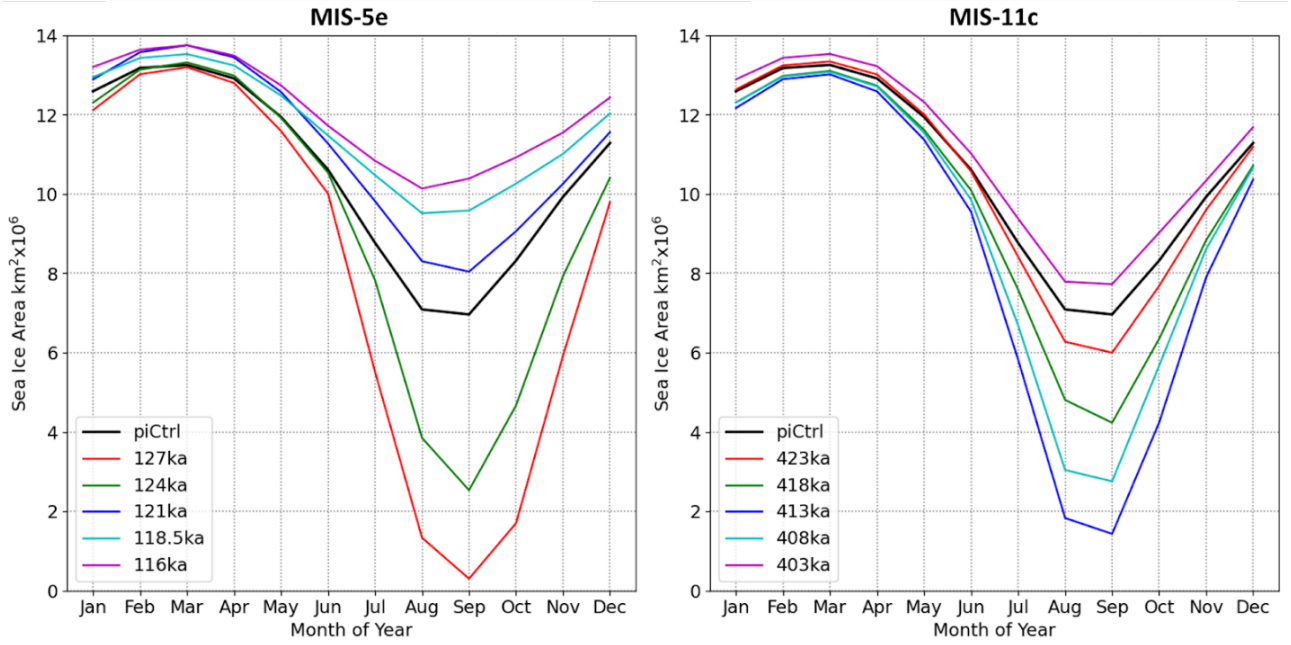

Figure 5-1. Comparison of the climatological seasonal cycles of Northern Hemisphere ice cover by timeslice, with MIS-5e simulation periods on the left and MIS-11c on the right. The black curve in both panels is the climatology from the preindustrial simulation.

Also very apparent is the rapid nature of change between time slices in MIS-5e as compared to those in MIS-11c. Despite having shorter time intervals between the simulations, the MIS-5e simulations rapidly progress from a high-amplitude seasonal cycle with virtually no September sea ice at 127 ka to a low-amplitude seasonal cycle with greater ice coverage than preindustrial in all months already by 121 ka. MIS-11c, on the other hand, begins with similar ice evolution to preindustrial at 423 ka, gradually evolves towards a higher-amplitude cycle with low September sea-ice minima at 413 ka, then rapidly shifts from a low summer sea-ice regime at 408 ka to having greater sea-ice area than preindustrial by 403 ka. There are, however, no drastic alterations of the seasonal cycle between the two sets of interglacial simulations, with the seasonal-cycle amplitude and rate of change between time slices standing out as the primary differences.

A closer examination of the time series of September months across the simulations shows the trend in sea-ice area between simulations even more clearly. Figure 5-2 is constructed by stitching together the time series of the final 100 years of each time-slice simulation, with spacing between the time series proportional to the length of time between the simulations. Therefore, while the time series themselves are not to scale with the times indicated on the abscissa, they proportionally show the evolution of September sea ice throughout each interglacial as well as the interannual variability in September ice area. The extremely low sea-ice area levels previously discussed in 127 ka are clear to see, as well as the broad similarities between 124 ka and the 413-408 ka period in MIS-11c. Also evident is the rapid recovery of September sea-ice levels in MIS-5e and the drastically shorter duration of full-interglacial conditions compared to MIS-11c.

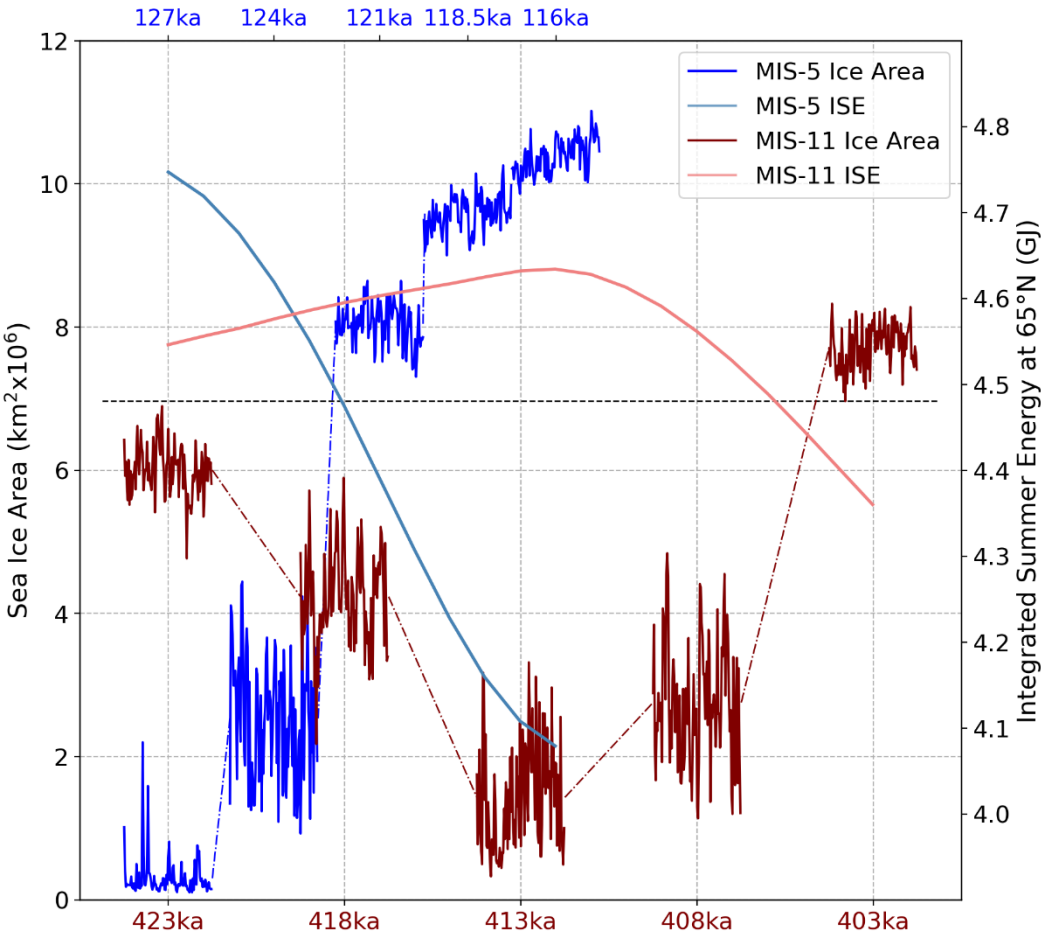

Figure 5-2. Pseudo-time series of Northern Hemisphere sea-ice area for the month of September (left axis) and integrated summer energy (ISE) at 65°N from Huybers (2006). Sea-ice area time series consist of the final 100 years (quasi-equilibrated time) of each time-slice simulation, used here to represent each period designated on the abscissa. While time series are not proportional, the spacing between the time slices does correspond to the interval between forcing conditions, and thus the MIS-5e time series (dark blue, top axis) is shorter than the MIS-11c one (dark red, bottom axis). The dashed black line shows the mean September sea-ice area from the preindustrial control simulation.

To investigate the forcing of the long-term sea-ice evolution, the high-latitude ISE throughout MIS-5e and MIS-11c is plotted in Figure 5-2. Following Huybers (2006), the values of ISE are defined as the integrated energy flux of all days in which the top-of-atmosphere insolation exceeds a given threshold at a given latitude (in this case, 325 W m^{-2} at 65°N). It is obvious that the sea-ice area in both interglacials is inversely correlated with the ISE, which undergoes a rapid transition from very high levels at 127 ka to much lower than present-day beyond 121 ka (present-day value approximately 4.42 GJ) and peaks at around 412 ka during MIS-11c. While the magnitude of the insolation decrease throughout MIS-5e is much higher, both interglacials see a sharp increase in September sea-ice area to above-preindustrial levels (dashed black line in Figure 5-2) as ISE decreases towards and below preindustrial levels, suggesting the possibility of threshold behavior as simulated in Yin et al. (2021). While the ISE appears to be a good metric to explain the multi-millennial sea-ice evolution in the Arctic, the summer solstice (21 June) maximum insolation is poorly correlated with the total sea-ice area during MIS-11c (Supplementary Figure 5-S1), and hence cannot explain the long-term sea-ice behavior.

Periods of particularly low ice levels are confined to the early stages of MIS-5e (127 and 124 ka) and the latter-middle stages of MIS-11c (413 and 408 ka). The spatial contrasts in the September ice area for these periods

are therefore comparatively illustrated in Figure 5-3. At 127 ka, the simulated ice of at least 15% concentration has retreated to a small cluster along the coasts of northern Greenland and the northern reaches of the Canadian Arctic Archipelago. By 124 ka, however, the September mean sea-ice extent is already substantially recovered towards preindustrial levels (given by the bold red line), extending across the entire Arctic from Greenland and the Canadian Arctic Archipelago to the central Siberian coast.

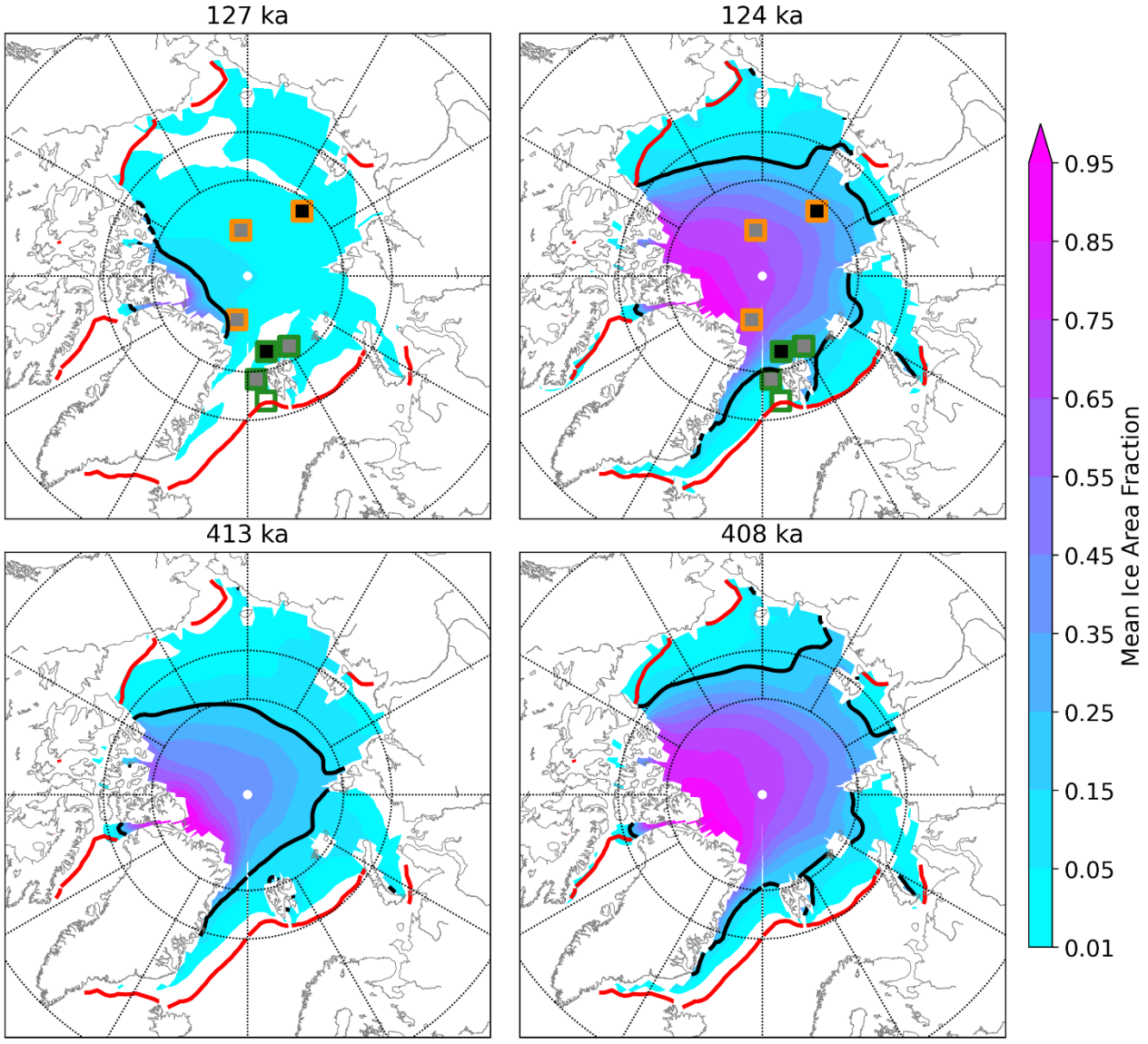

Figure 5-3. A comparison of mean September sea-ice concentration for the final 100 years of each indicated time slice simulation: 127 ka (top-left), 124 ka (top-right), 413 ka (bottom-left), and 408 ka (bottom-right). The bold black line indicates the 15% ice concentration contour, below which conditions are regarded as "open water." The red contour shows the 15% ice concentration contour for the preindustrial simulation. Colored icons in the MIS-5e simulation panels correspond to selected sediment core locations from other studies. Black filling indicates that sea-ice cover likely stayed year-round through the LIG, gray filling indicating partial seasonal coverage, and white indicates open-water conditions. Green frames denote well-dated points, while orange frames indicate cores with poor chronology.

A number of LIG high Arctic sediment core records of various origins were compiled for comparison with PMIP models by Kageyama et al. (2021), a selection of which have also been plotted in the MIS-5e panels of Figure 5-3. Among these are three poorly-dated biomarker records from approximately the MIS-6 to MIS-5 period, which can provide insights into the probable presence or absence of sea ice on the basis of biological

productivity of a number of species (Stein et al., 2017). The lack of quality timing information limits the utility of the cores to providing semi-quantitative estimates of consistently closed (black marker fillings) or seasonally open water conditions (gray marker fillings for seasonal cover, white for fully ice-free) within the general MIS-6 to MIS-5 timespan. These poorly dated records have orange symbol borders in Figure 5-3. Two of these poorly dated cores are PS2200 (just north of Greenland) and PS51/038 (central Arctic), and both are suggestive of predominant perennial sea-ice conditions. The presence of foraminifera in these samples indicates that some limited phases of open-water conditions must have been present (Stein et al., 2017). Our simulations could therefore be interpreted as consistent with this explanation, with predominantly open-water conditions simulated at 127 ka and ice concentrations of 55-85% by 124 ka (and therefore a return to predominantly perennial ice conditions).

A third and more puzzling result among the poorly-dated cores is provided by core PS2757, located just poleward of the Laptev Sea. Despite our simulations suggesting near ice-free conditions here at 127 ka and ice concentrations of 25-45% at 124 ka, biomarkers from this core indicate primary productivity remained near zero throughout MIS-5e and thus suggest completely closed ice conditions. This result is particularly difficult to explain given that this site already experiences ice-edge or ice-free conditions in modern summers. However, given that the proxies in question are analyzed on the basis of trace biomarkers, caution should be exercised in their interpretation, and it is possible that alternative explanations exist for the lack of open-water indicators during MIS-5e (Sime et al., 2023).

Among the better-dated core locations (indicated by green square frames in Figure 5-3) are the PS2138 cores, both located north of Svalbard (Stein et al., 2017; Matthiessen et al., 2001). These rely on dinocysts and the IP25 ice proxy, can both be dated to MIS-5e, and are indicative of seasonally ice-free conditions during MIS-5e. This region is characterized by June-to-August-mean sea-ice concentrations of less than 5% in our 127 ka simulation and approximately 15-35% in our 124 ka simulation, providing ample opportunity for open-water phytoplankton species to be productive and thus in strong agreement with these proxies. Additional well-dated core proxies using dinocysts and IP25 from around Svalbard present a similar picture, cores PS93/006-1 and PS92/039-2 potentially indicative of seasonally ice-free conditions (Kremer et al., 2018). The southernmost record considered here is M23455 and indicates year-round ice-free conditions in MIS-5e (Van Nieuwenhove et al., 2011). It therefore appears probable that the peak forcing conditions of early MIS-5e were sufficient to cause some largely ice-free summers in the Arctic, but these were likely in part enabled by internal variability (cf. Stein et al., 2017) and constrained to a short period of no more than a few thousand years. Regional confidence in ice-free conditions also varies considerably, with the well-dated proxies from around Svalbard and the Fram Strait providing a much clearer picture than the poorly-dated cores of the high Arctic.

As expected, the selected MIS-11c time slices demonstrate a less extreme evolution of sea ice, with 413 ka ice extent (15% boundary) slightly smaller than that at 124 ka, but with notably lower ice concentrations across the central Arctic basin. The 413 ka mean September ice area also broadly resembles the low ice pack of recent warmer summers since the year 2000, with ice fractions of 15-50% across much of the central Arctic and a

primary ice center surviving near Greenland and the Canadian Arctic Archipelago. September sea ice in the 408 ka simulation already shows a recovery to higher sea-ice concentrations and bears a very strong resemblance to the simulated 124 ka ice pack.

Without reliably dated paleoproxy records for MIS-11c, it is difficult to further evaluate the MIS-11c simulations except in comparison to the MIS-5e simulations. However, an examination of other sea-ice characteristics, such as its variability, age, and thickness, can yield additional insights into the different sea-ice regimes between the two interglacials.

5.3.2 Interannual sea-ice variability and characteristics

Examinations of the mean state for end-of-summer Arctic sea-ice conditions across the selected simulations have so far revealed similar patterns for 124 ka, 413 ka, and 408 ka, but does interannual variability within the simulations manifest similarly? To find out, a standard deviation of the time series of monthly September ice area fraction from the 100 simulation years per time slice was calculated and is captured in Figure 5-4. Unsurprisingly, the 127 ka simulation stands out as having the least overall interannual variability, driven by the very low ice concentrations across virtually the entire Arctic. In this case, the highest variability is actually concentrated along the northern coasts of Greenland and Ellesmere Island.

The opposite pattern emerges for the other three time slices examined in Figure 5-4: all of 124 ka, 413 ka, and 408 ka have local standard deviation minima in the Nares Strait and surrounding coastal regions, corresponding to the most stable remaining area of summer ice in these simulations. Instead, maximum interannual variability occurs along and within the mean 15% sea ice concentration contour, highlighting that the ice margin, particularly when it is located in open seas rather than coastal waters, contains the most responsive ice. The pattern at 413 ka is slightly different, with a center of variability directly over the central Arctic, suggestive of increased melt sensitivity here near the MIS-11c peak in ISE. The overall pattern that emerges is that regions with moderate levels of ice concentration (approximately 20-60%) experience the greatest interannual variability, while areas of very low (<20%) or very high (>60%) ice concentration are the least variable.

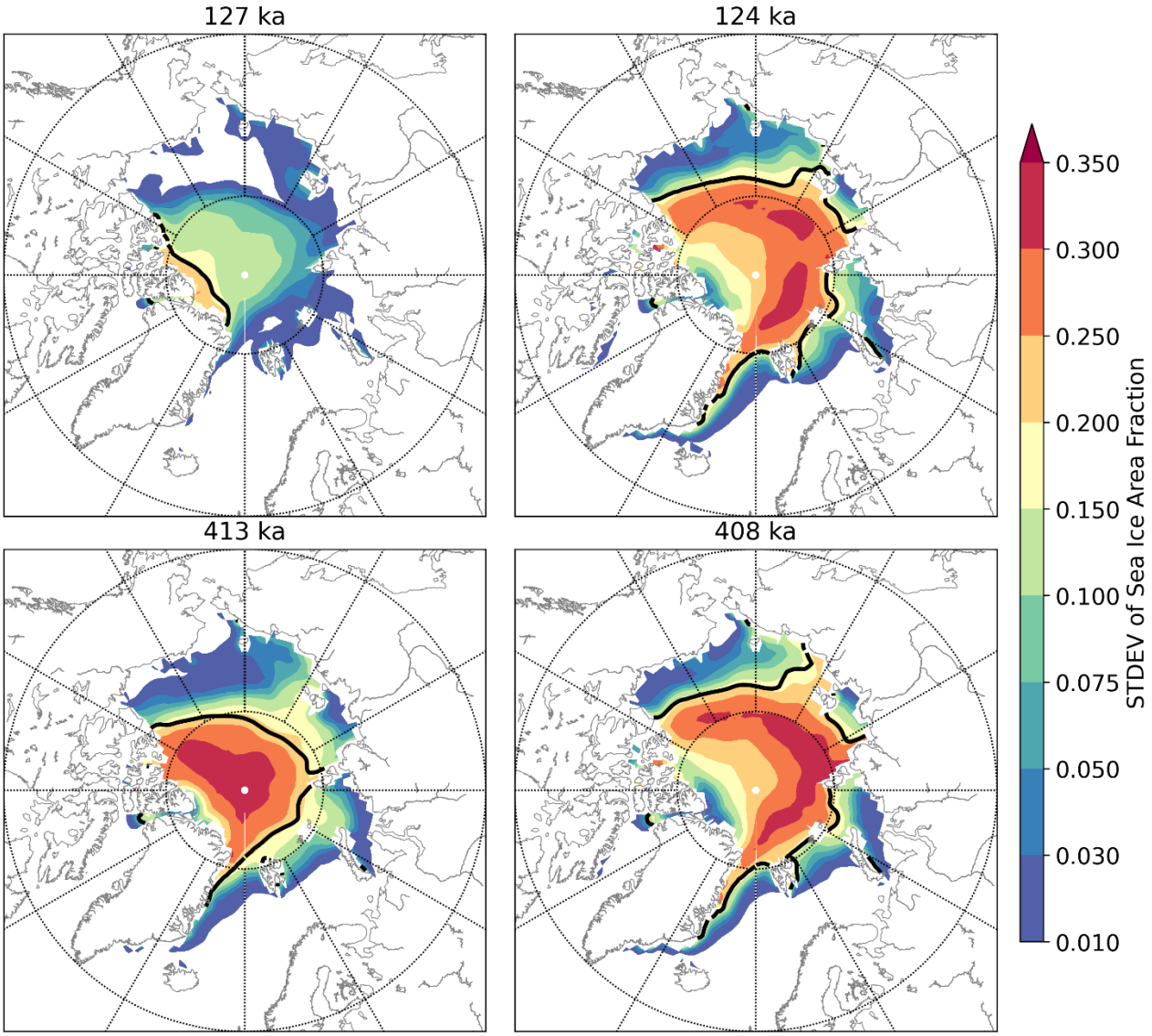

Figure 5-4. Spatial comparison of the standard deviation (unitless) of September sea ice fraction across the selected time slice simulations. The black contour represents the 15% sea ice area boundary as in Figure 5-3.

This relation is also reflected in a comparison of the sea-ice area means and standard deviations from entire time slices to each other (Figure 5-5). Depicted is the mean September sea-ice area per time slice simulation against the standard deviation of that 100-year time series from each simulation. Although we have only one data point in the low-area, low-variability bottom-left of the plot (127 ka), the relationship bears strong resemblance to a skewed bell curve with a long right tail. The greatest sea-ice standard deviations occur with a mean ice area of around 3.0 million km^2 (the 124 ka and 408 ka time slices), tailing off quickly at higher and lower mean areas. Such a pattern can be both physically and mathematically explained: the cluster of simulations with sea-ice levels greater than the preindustrial simulation are characterized by sea ice across the entire central Arctic, extending to both the Siberian and Canadian coasts, and are thus geographically constrained. The very low-ice state at 127 ka simply does not have enough ice cover to produce a high standard deviation, which is partly due to the effects of self-reinforcing Arctic amplification helping to maintain consistently low ice levels year after year. The intermediate states, however, have moderate concentrations of sea ice across the open Arctic, which are subject to rapid export, breakup, or melting, depending on the dominant weather patterns of a given summer. On the other hand, Arctic summers that skew cold, cloudy, or

relatively stable could provide for less favorable melt conditions across a wide expanse of these "vulnerable" ice regions.

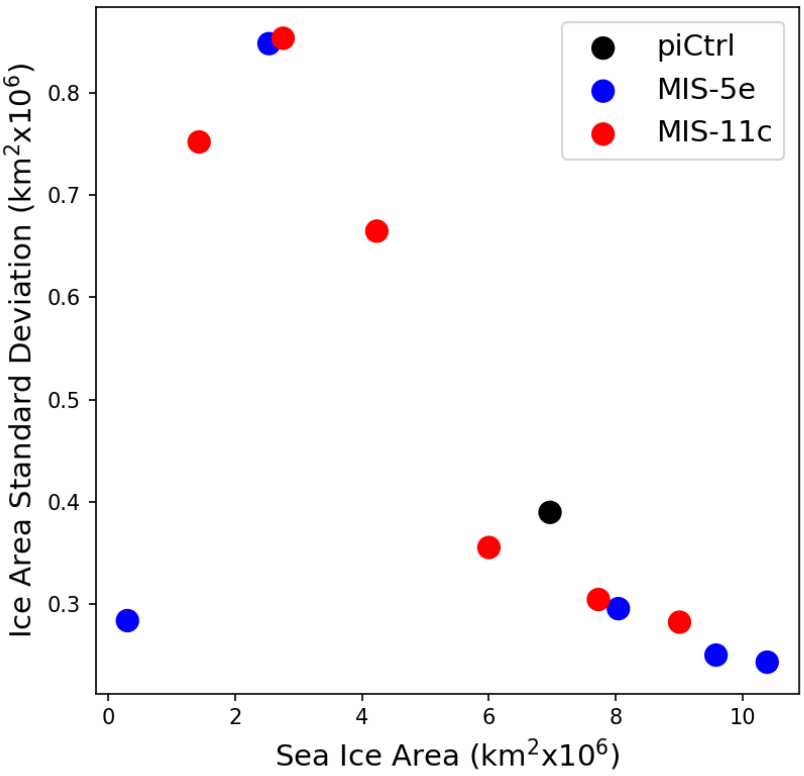

Figure 5-5. Scatterplot of mean September sea ice area against the standard deviation for each time slice, including the preindustrial control.

Multi-year ice has practically vanished in the 127 ka simulation outside of small pockets in the Nares Strait and Canadian Arctic Archipelago, meaning the sea-ice regime is completely dominated by annual ice (Figure 5-6). As a result, lower September sea-ice variability is present in this simulation (Figure 5-4 and 5-5), but a much higher-amplitude seasonal cycle occurs compared to all other simulations (Figure 5-1). In contrast, the 413 ka simulation exhibits much greater survival of multi-year ice and contains a large swath of ~2-year ice in an arc from the Canadian Arctic Archipelago through the Beaufort Sea and towards the East Siberian Seas. Summer ice concentrations in this region are generally low (Figure 5-3), but what survives is tendentially thicker and capable of further thickening by new basal ice growth the following winter.

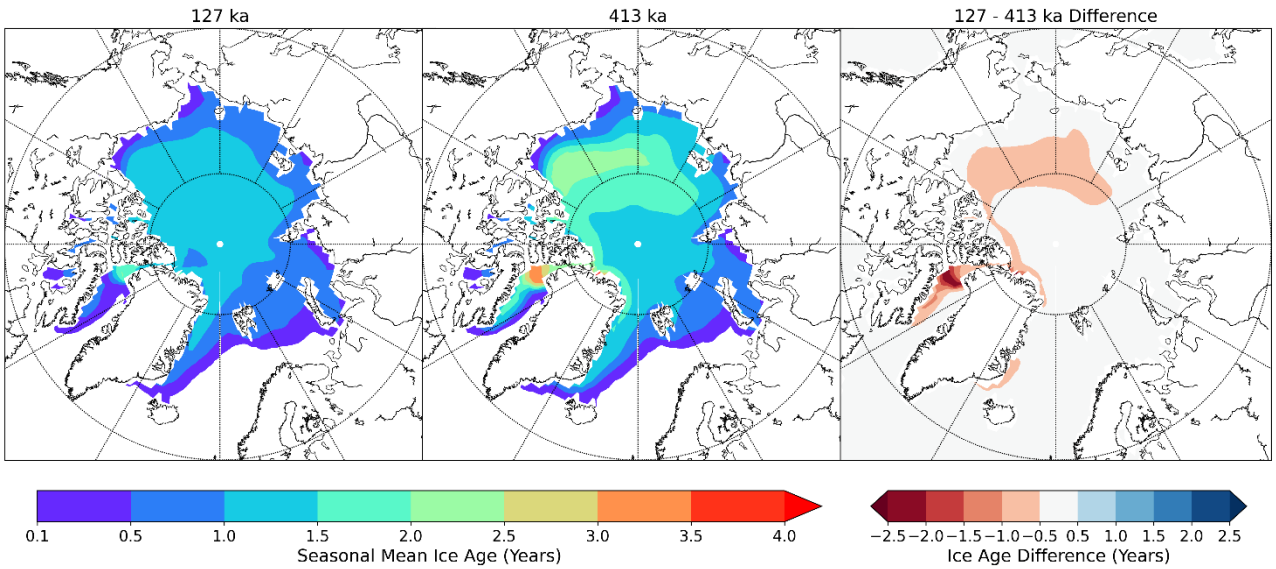

Figure 5-6. Comparison of the mean sea-ice age in September in years between the 127 ka MIS-5e simulation (left panel) and the 413 ka MIS-11c simulation (center panel). The difference is illustrated in the right panel, with negative numbers corresponding to 413 ka sea ice being older than in 127 ka.

The relative summer melt vulnerability of first-year ice lies primarily in its thinness, which is also related to how favorable ice-growth conditions are in the colder seasons. Purely based on the distribution of insolation, which is higher for boreal winters in MIS-11c than in MIS-5e, it might be expected that MIS-5e winters actually feature thicker ice cover than MIS-11c winters. In fact, this appears to be overpowered by the extra heat introduced to the Arctic Ocean during the more extensive open-water conditions during boreal summer and fall. Figure 5-7 compares the mean boreal winter ice thickness of the 127 ka and 413 ka simulations, which correspond to the minimum simulated summer ice cover for each interglacial. The right panel clearly shows thicker winter sea ice during MIS-11c despite higher winter insolation. The differences span the entire Arctic basin, with ice even +0.5 m or more thicker along the northern and eastern coasts of Greenland during MIS-11c.

The mean sea-ice thicknesses converge across the central Arctic by boreal spring (March-April-May; not shown), but thicknesses remain 0.2-0.5 m greater along the Canadian Arctic Archipelago and the Greenland coastal regions. Sea-ice production in the 127 ka simulation therefore “catches up” to that of the MIS-11c simulation throughout winter and spring due to lower insolation forcing, but the much higher ISE during 127 ka summers results in a thinner overall ice pack throughout the year.

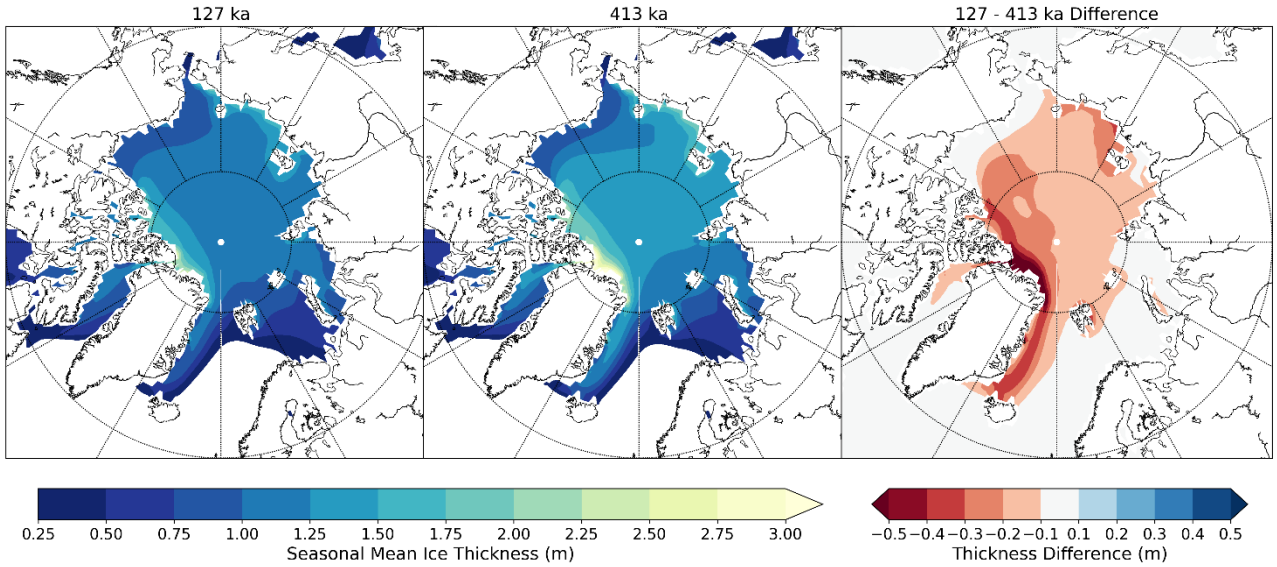

Figure 5-7. Comparison of the mean seasonal sea-ice thickness for December-January-February. The left panel shows winter averages from the 127 ka (MIS-5e) simulation, the middle panel shows the winter average for 413 ka (MIS-11c), and the right panel is the difference (127 ka minus 413 ka), demonstrating that winter sea ice was thinner in 127 ka.

While we have attempted to explain the differences in sea-ice evolution during the two interglacials by means of insolation (ISE), previous work has suggested that the LIG Arctic sea-ice cover might also be sensitive to changes in poleward ocean heat transport by the Atlantic Meridional Overturning Circulation (AMOC; Stein et al., 2017). A stronger AMOC transporting more heat poleward has also been suggested to explain the long-lasting and anomalous (relative to insolation forcing) high-latitude warmth of the MIS-11c interglacial (Rachmayani et al., 2017). An expected consequence would therefore be an inversely correlated AMOC strength and Arctic sea-ice area. As depicted in Figure 5-8, however, this does not appear to be the case in our simulations. Though the variations in the strength of the AMOC between time slices are relatively small and the interannual variability relatively large, the depicted trends would actually suggest a weak positive correlation between the AMOC and sea-ice area. During the minimum ice periods at 127 ka and 413 ka, the AMOC is at its weakest (and least variable) in our simulations. The high-ice periods in the latter stages of MIS-5e are also characterized by a generally strong but highly variable AMOC. While it is true that the AMOC in early MIS-11c (423 ka) appears marginally stronger than in the early stages of MIS-5e (127-124 ka), there is considerable overlap in their interannual variability. These observations come with the notable caveat that our simulations utilize a static Greenland ice sheet, and therefore the only meltwater or runoff contributed by Greenland in the model is from precipitation and seasonal snowpack. However, it appears that establishing a clear link between AMOC strength and sea-ice levels would require substantially more investigation.

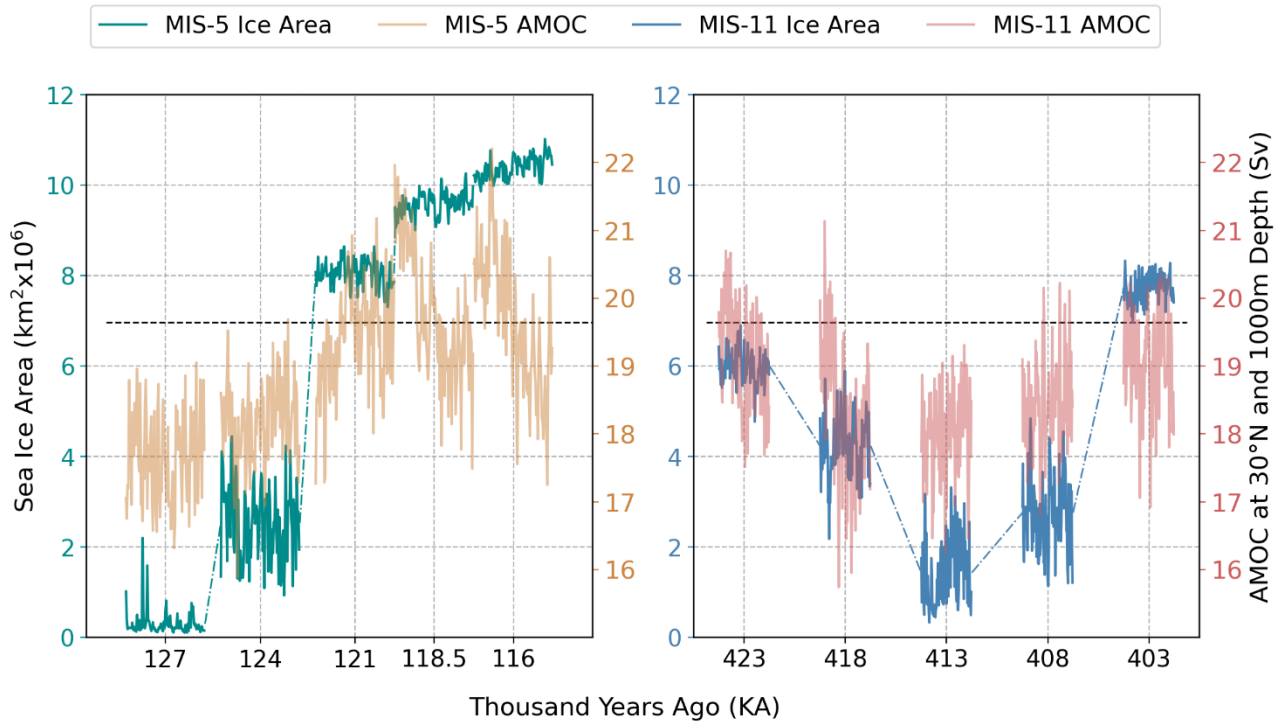

Figure 5-8. Pseudo-time series comparing the September sea-ice area (as in Figure 5-2) for the MIS-5e (left) and MIS-11c (right) simulations, but including a comparison to the mean annual strength of the AMOC.

5.3.3 Surface temperature response

Disentangling external forcing and feedback from one another is notoriously difficult, but the robust seasonal temperature anomaly patterns in our simulations grant us some insight into the effects of the orbital forcing versus sea-ice feedbacks. The favorable alignment of precession and obliquity early in MIS-5e results in very high boreal summer insolation and thus, high ISE. Analysis of calendar-corrected mean 2-meter air temperatures for all four seasons from our 127 ka simulation show the response to be a somewhat uniform increase in temperatures of 2-5°C during the boreal summer season (June-July-August; bottom-left panel of Figure 5-9). Over the central Arctic Ocean, anomalies are capped by the large uptake of latent heat from melting sea ice and the heat capacity of open waters and are generally in the 2-3°C range. However, far more extreme temperature anomalies emerge in the boreal fall, with +7-10°C anomalies spanning the entire Arctic Ocean and much more modest warm anomalies dominate the adjacent land regions.

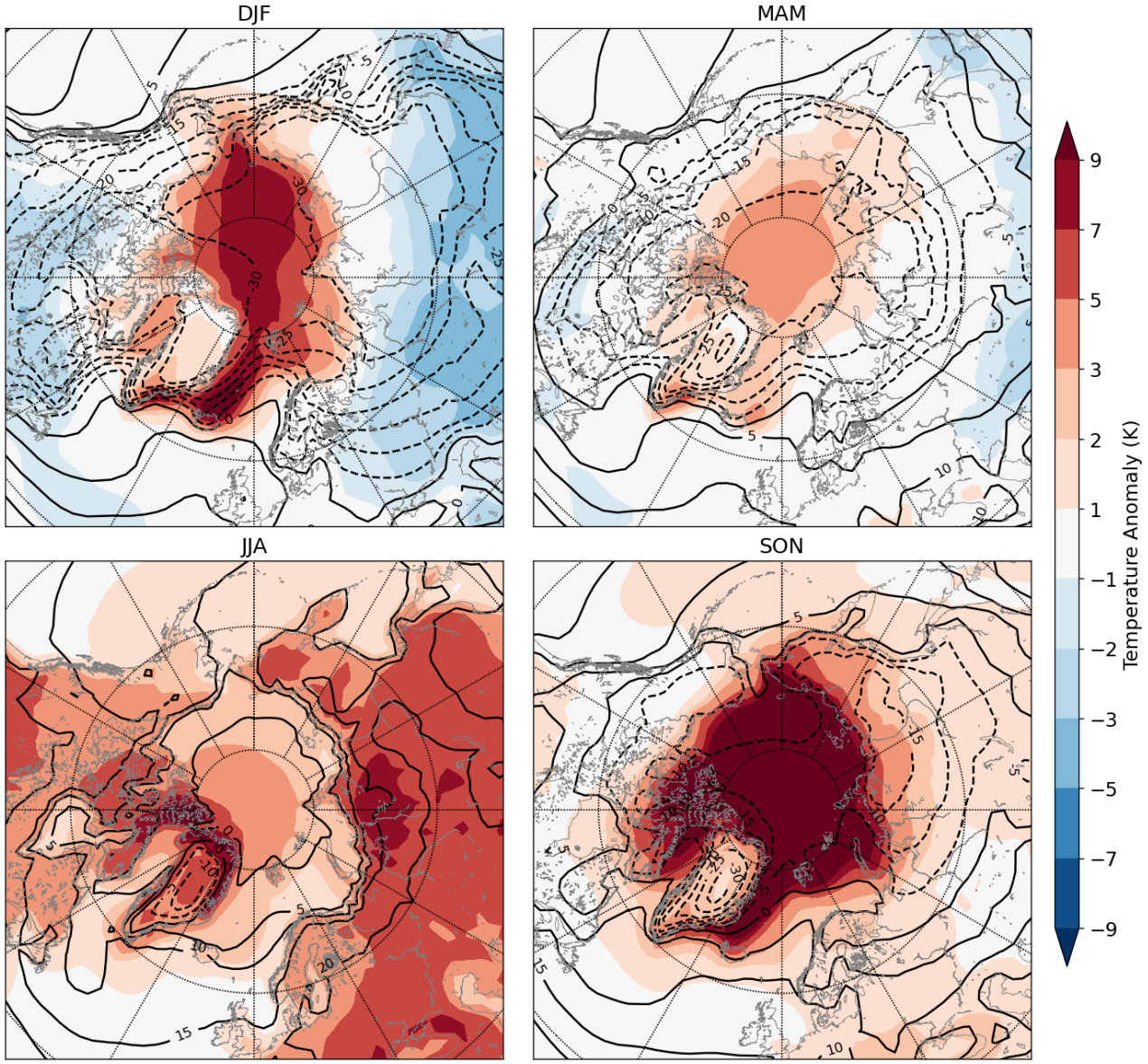

Figure 5-9. Seasonal-mean 2 meter air temperature anomalies over the final 100 years of the 127 ka simulation. Absolute temperatures are depicted by the solid (>=0°C) and dashed (<0°C) black contours, while anomalies relative to the preindustrial control simulation are given by shading, with red depicting where interglacial temperatures were warmer than preindustrial and blue colder.

Comparison of the fall temperature anomaly pattern with that from the 413 ka simulation (MIS-11c; Figure 5-10) suggests that the extreme fall anomalies in both 127 ka and 413 ka are largely a result of sea-ice feedbacks in the Arctic. Whereas fall temperatures over Greenland and Eurasia at 127 ka are generally 1-3°C above preindustrial, they are at-or-below present day levels over nearly all Northern Hemisphere land areas for the 413 ka fall season. We suggest that the extreme warmth over the Arctic Ocean largely results from heat released back to the atmosphere from an ocean that, in preindustrial and modern times, is already covered by early-winter sea ice for much of the season. This is consistent with previous analysis of the seasonal Arctic energy budget for MIS-5e, in which the largest Arctic temperature anomaly occurs in fall due to the anomalously-warmed Arctic Ocean returning stored summer heat and releasing water vapor to the atmosphere, which leads to a positive longwave cloud radiative feedback (Sicard et al., 2022).

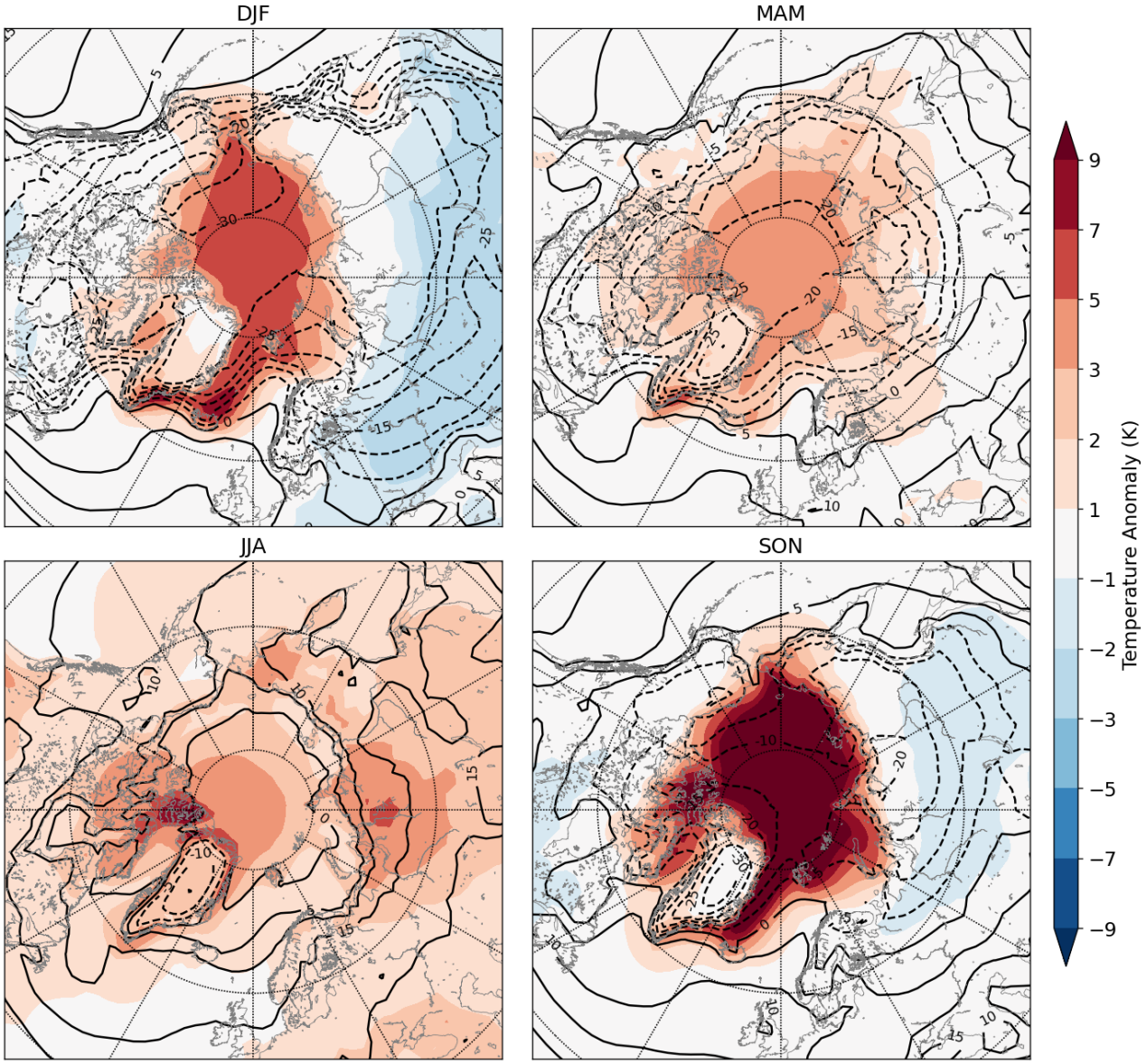

Figure 5-10. As in Figure 5-9, but for the 413 ka simulation.

In both interglacial periods, the impacts of the thinner, younger, and less extensive sea ice continue to manifest in substantial winter surface air temperature anomalies of generally 1-5°C over the Arctic, despite the absence of insolation during the polar night. This effect even lingers into the following spring, with Arctic air temperatures remaining slightly warmer than preindustrial, potentially portending an earlier onset to the sea-ice melt season. Simulations of the Holocene climate optimum (ca. 6 ka) suggest that this pattern is consistent across interglacial insolation maxima, with summer sea-ice losses proving persistent through fall and winter and driving warm anomalies in high latitudes (e.g., Park et al., 2019). Both interglacials therefore exhibit obvious signs of a sea-ice loss driven Arctic amplification, with remote consequences likely due to atmospheric teleconnections and increased high-latitude moisture fluxes.

5.4 Discussion

In the interglacial time-slice simulations presented here are numerous noteworthy features that correspond to other simulations of past warm interglacial conditions or hypothesized features of ice-free Arctic summers in the near future. The large increases in sea-ice levels between some consecutive interglacial time slices

(especially 124 to 121 ka and 408 to 403 ka) despite relatively modest ISE changes seem to indicate that Arctic climate may be susceptible to abrupt changes at insolation forcing thresholds. It is unclear if a similar sea ice collapse threshold exists early in interglacials (cf. Thomas et al., 2020), as our time-slice simulations do not extend far enough back into early MIS-5e and MIS-11c to avoid effects from the presence of remnant ice sheets at these times.

Seeking to understand the response of the Arctic sea ice to warmer-than-present interglacial conditions is of course motivated by comparisons to the present and near-future, in which sea ice is projected to rapidly decrease. MIS-5e in particular has been identified by some as a key case study for ice-free summers in the Arctic, with apparent "Atlantification" of central Arctic waters paralleling trends already observed in the present-day (Vermassen et al., 2023). Indeed, our 124 ka and 408 ka summer sea ice simulations already bear a strong resemblance to recent record-low sea ice summers such as 2007 and 2012, suggesting a regime shift is already in progress. The 127 ka simulation gives us an idea of the future state of the Arctic sea ice after this regime shift is complete: the disappearance of multi-year sea ice, a transition towards a high-amplitude seasonal cycle of ice cover, and very low levels of late-summer sea ice with low interannual variability for virtually the entire high Arctic.

Our chosen modeling methodology employs time-slice simulations with prescribed present-day topography, bathymetry, and land cover. Freshwater input from melting land ice was neglected, as were local geographic features like the Eemian Sea and Karelian seaway (e.g. Miettinen et al., 2014). Pfeiffer and Lohmann (2016) found that alteration of Greenland's topography alone in MIS-5e simulations would lead to additional warming across most of the high latitudes, although primarily in winter and as a secondary effect to insolation forcing. O'ishi et al. (2021) highlighted the role of vegetation feedbacks in reproducing annual warming at high northern latitudes in simulations of the LIG. It is therefore likely that the robust Arctic warmth in our simulations would be even more enhanced in simulations with an interactive ice sheet and vegetation. On the other hand, substantial meltwater input could produce a counteracting local cooling effect, likely playing a role in enhancing sea-ice levels and affecting variability in favored runoff regions.

In a larger context, Arctic sea-ice loss and the atmospheric circulation changes that it induces can significantly impact the degree to which the Greenland ice sheet experiences surface melt. The increased presence of open water on the Greenland coast enables increased oceanic heat flux and increasing melt area, particularly over western portions of the ice sheet in August and September (Rennermalm et al., 2009). These satellite-based observations of the modern era are further supported by analysis of an ensemble of CMIP5 models, which indicate that although the effect is mostly localized and minor compared to overall atmospheric warming trends, loss of sea ice in the Baffin Bay and the Greenland Sea do indeed result in greater melt extent (Pedersen and Christensen, 2019). Idealized simulation experiments also indicate the potential for anomalous mid-tropospheric ridging to emerge over the Baffin Bay and western Greenland with sea ice loss, potentially raising the frequency of blocking episodes over Greenland and enhancing the onshore flow of heat in specific regions (Sellevold et al., 2022). The present balance of evidence would therefore indicate that continued Arctic sea-

ice loss likely contributed to enhanced ice-sheet melting in the MIS-5e and MIS-11c interglacials and will do so again in the near future.

5.5 Conclusions

Here we have sought to evaluate the relationship between Arctic sea ice, its interannual variability, and the ISE in two of the most critical interglacials of the late Pleistocene, MIS-5e and MIS-11c. This has been done primarily via a comparative time-slice modeling approach, although comparison with some sea-ice proxy reconstructions did provide indications that our MIS-5e simulations show what is likely a realistic scenario for the summer sea-ice state in MIS-5e. A similarly direct evaluation of the model performance during MIS-11c was not possible due to the lack of suitable proxy data.

The two interglacials were subject to very different orbital forcing conditions, resulting in different patterns of sea-ice retreat that were strongly related to the ISE. The early stages of MIS-5e experienced extreme warmth resulting from very high ISE and a consequent near-collapse of summer Arctic sea ice in our 127 ka simulation. However, a combination of (1) the rapid recovery of sea-ice levels as ISE dropped by the 124 ka simulation and (2) the relatively weak and inconclusive indications of seasonally ice-free conditions from the proxy data would suggest that any phase of ice-free summers during MIS-5e must have been confined to a brief period of a few thousand years or less. Such a period would have been characterized by the survival of virtually no multi-year ice, a high-amplitude seasonal cycle of sea ice cover, and relatively low interannual variability in summer sea-ice cover.

MIS-11c, on the other hand, did not achieve the same minimum summer ice area, but may have had 15,000 years or more (ca. 423-408 ka) with summer sea-ice levels below preindustrial levels, and without a highly pronounced insolation maximum. The evolution of sea-ice cover in MIS-11c is also suggestive of a high degree of sensitivity to the ISE rather than the absolute maximum insolation forcing, which is much lower in MIS-11c compared to MIS-5e. The extremely rapid increase of September sea-ice area from 124 to 121 ka and from 408 to 403 ka as ISE decreases below present-day values is also suggestive of a threshold response in summer sea-ice melt. In our simulations, the evolution of ISE would seem to explain virtually all of the sea-ice behavior, as ice cover conditions are very similar between simulations from different interglacials with very similar levels of ISE. Any additional contributions to Arctic sea-ice loss from AMOC changes appear to have been minor.

Finally, our simulations indicate a clear relationship between Arctic sea-ice area and its variability. Interannual variability in summer sea-ice levels maximizes for intermediate levels of ice cover, with very high and very low ice-cover states being geographically constrained. Intermediate levels of ice cover, however, are characterized by the presence of fractional ice cover across the open Arctic, where it is subject to export, mechanical breakup, and weather anomalies. On long time scales, these more volatile summer sea-ice regimes are likely to signify transitions between relatively stable high-ice summers and low-ice summers, a transition which appears to be underway in the modern Arctic.

5.6 Supplement to Chapter 5

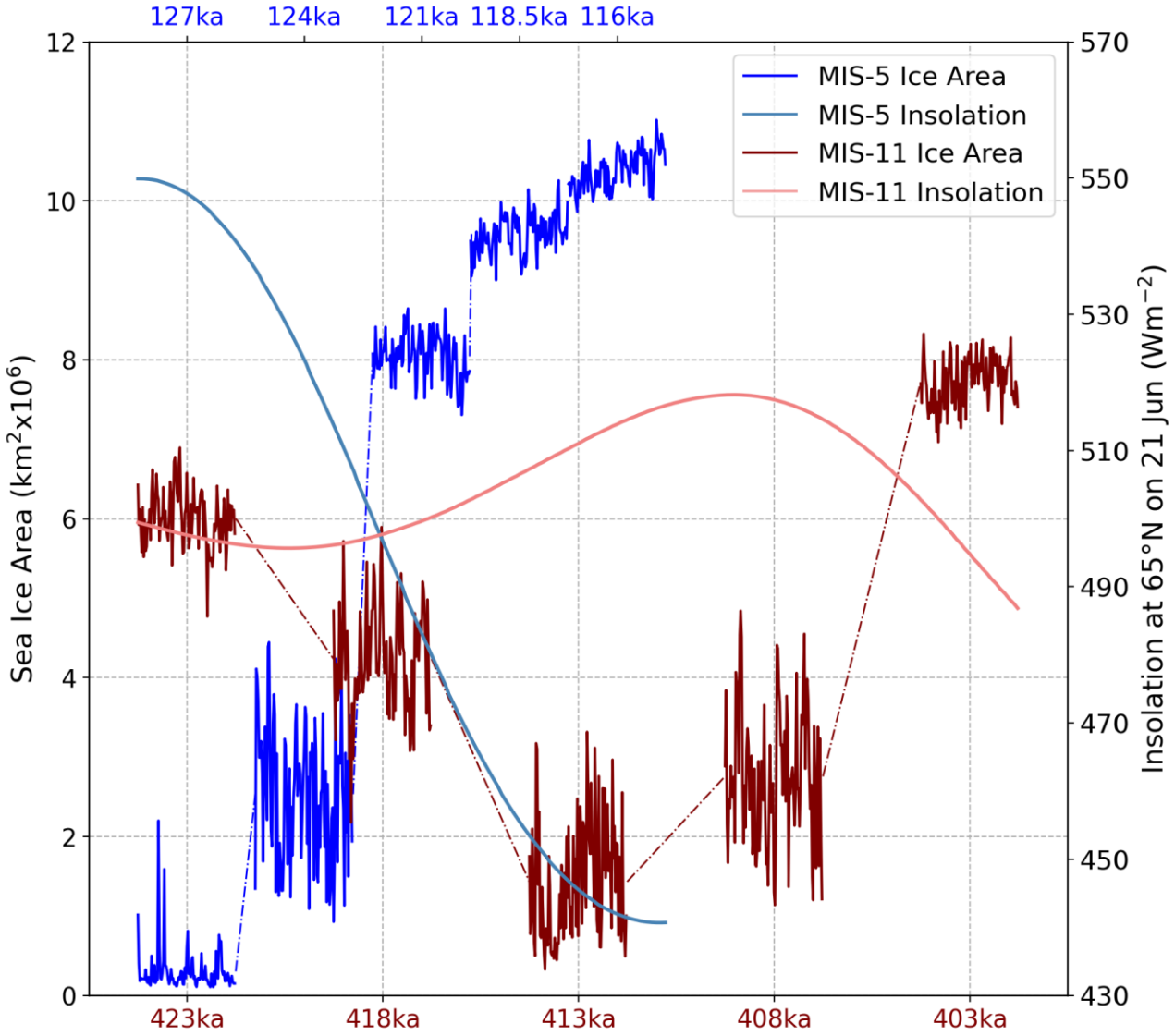

Figure 5-S3. Pseudo-time series of September sea ice area from the MIS-5e simulations (dark blue) and MIS-11c simulations (dark red). The time series consist of the final 100 years of each time slice simulation and are therefore disproportionate to the time axes on top and bottom. The length of the complete pseudo-time series including gaps are approximately proportional to the length of the time periods represented by the simulations. The continuous curves represent the 65°N insolation on 21 Jun as calculated after Laskar et al. (2004); MIS-5e is in light blue and MIS-11c is in light red.

Chapter 6

Conclusions and Outlook

6.1 Conclusions

The studies assembled in this dissertation have sought to answer numerous questions regarding the climate and its influence on the melt of the GrIS during past warm interglacials. In particular, the focus has been on MIS-11c, long regarded as an unusual interglacial and one whose relative high-latitude warmth has proven difficult to fully explain (e.g., Rachmayani et al., 2017; Tzedakis et al., 2022). We therefore hypothesized that the orbital forcing conditions during MIS-11c may have induced atmospheric circulation feedbacks that helped transport additional heat polewards, increasing the vulnerability of the Greenland ice sheet to summer melt episodes and helping to sustain the anomalous high-latitude warmth. However, investigation of our time slice simulations did not locate such a feedback, and instead indicated that at least over the North Atlantic sector, the jet stream tends towards a weakened, unified, and equatorward-shifted state. This transition correlates with surface air temperatures around Greenland: the warmer Greenland becomes, the more the jet shifts equatorward, and the weaker poleward eddy heat fluxes in the region become, particularly in the summer season. When combined with statistically significant annual-mean precipitation increases over much of the GrIS, it is concluded that feedbacks in the atmospheric circulation were not responsible for the substantial melt volume that the ice sheet experienced in MIS-11c.

In Chapter 4, we more explicitly examined the melt sensitivity of the GrIS during MIS-11c by interpolating continuous climate forcing from our time slice simulations and coupling them to the Glacial Systems Model (GSM) ice-sheet model. Using a calibrated ensemble of parameter vectors that accurately reproduces the evolution of the GrIS from the Last Glacial Maximum through today, we focused our experiments on the uncertainties around bias correction and coupling of the climate forcing to the ice-sheet model. We found that the typical means of coupling climate model temperatures to an ice-sheet model, which is to use a fixed lapse rate that is spatially invariant, is inferior to lapse rates calculated based on the model climatology. Monthly-mean lapse rates, fully varying (spatially and temporally) lapse rates, and daytime-only lapse rates all represent an improvement in matching the constraints given by ice-core data, and the fully varying lapse rates had by far the greatest match rate. Results were also sensitive to the choice of a present-day baseline climatology used for bias correction and whether precipitation bias correction was applied differently in different regions of the GrIS. Our simulations that best-matched ice-core criteria indicate a mean GrIS contribution to sea-level rise in MIS-11c of 3.9 m (middle 80% range 3.2 to 4.6 m). Given the neglected feedbacks from basing our climate simulations on a fixed modern-day ice sheet configuration, this represents a reasonable lower bound for MIS-11c.

Finally, our model-based investigation of past interglacials was expanded to encompass the Last Interglacial (MIS-5e) and the behavior of Arctic sea ice. Our simulations of MIS-5e conditions are in general agreement with limited proxy data and other recent modeling studies in suggesting that summers largely free of sea ice in the Arctic Ocean were possible for a brief period in the early stages of MIS-5e at peak integrated summer energy (ISE) forcing (ca. 127 ka). While ice levels increased again by 124 ka, they are still considerably reduced compared to the preindustrial period, and similarly low levels of sea ice may have been achieved during a long stretch of MIS-11c (ca. 418 to 408 ka based on our simulations), again driven by ISE higher than present day. Interestingly, interannual sea-ice variability in our simulations exhibits a clear but nonlinear relationship with sea ice area: at moderate sea ice areas, the variability is maximized, a consequence of having widespread low to medium ice concentrations across the central Arctic Ocean. There, the ice is subject to varying degrees of melt and export depending on the dominant weather patterns of a given summer. On the other hand, geographical constraints limit the variability of summer ice pack when ice area is very high (ice spread from the Canadian Arctic to the Siberian coast) or very low (as at 127 ka, when significant ice only remains along Ellesmere Island and the northern Greenland coast). This result suggests the intermediate stage between regimes of high and low summer Arctic sea ice are characterized by high volatility, something that we may be beginning to observe in the present climate.

6.2 Outlook

In these studies, we have opted for a focus on the atmospheric and cryospheric signals that emerge during the key MIS-5e and MIS-11c interglacials and how they may be most realistically utilized in simulating their effects on the Greenland ice sheet. Each of the studies presented here could be furthered with additional sensitivity experiments, particularly those that address the methodological shortcomings of our simulations. For example, utilizing a representative GrIS topography in the time slice simulations would enable direct comparison of the effects of the ice loss on regional warming (e.g., Pfeiffer and Lohmann, 2016) or the effects on atmospheric circulation. Explicitly accounting for the meltwater input of the GrIS into the ocean would also enable insights into, for example, whether our simulations produce too much interglacial sea-ice loss or whether the hypothesized strengthening of the AMOC in MIS-11c (e.g., Rachmayani et al., 2017) would be counteracted.

Accounting for these additional elements is increasingly possible as the paleoclimate modeling community continues to strive towards fully interactive coupling of ice and climate models on glacial timescales. This is even the case with complex AOGCMs in recent years due to robust improvements in computing power (e.g., Sommers et al., 2021). However, appropriate coupling methodologies remain critical to obtaining sound results, and we demonstrated in Chapter 4 that implementing techniques that are more physically sound need not require additional data or computationally expensive procedures.

There remain many challenges to reckon within the field of paleoclimate modeling, but so long as climatic proxy data from the ancient past remains spatially limited and difficult to accurately date, climate models will

remain an incredibly useful tool for understanding the dynamics that drove past climate changes. The Paleoclimate Model Intercomparison Project remains an excellent initiative for furthering our understanding of crucial aspects of the climate system such as its sensitivity to different forcings, and will soon include MIS-11c simulations in the hope of more fully understanding what made this interglacial so unique. Our studies here provide a springboard for future efforts in this direction and as such, contribute to our ability to better predict the complexities of our ever-evolving climate system.

References

Abe-Ouchi, A., Saito, F., Kawamura, K., Raymo, M. E., Okuno, J., Takahashi, K., and Blatter, H.: Insolation-driven 100,000-year glacial cycles and hysteresis of ice-sheet volume, Nature, 500, 190–193, https://doi.org/10.1038/nature12374, 2013.

Agassiz, L: Upon glaciers, moraines, and erratic blocks; delivered at the opening of the Helvetic Natural History Society, at Neuchatel, 24 July 1837. Edinburgh New Philosophical Journal, 24, 364-383, 1838.

Albrecht, T., Winkelmann, R., and Levermann, A.: Glacial-cycle simulations of the Antarctic Ice Sheet with the Parallel Ice Sheet Model (PISM) – Part 1: Boundary conditions and climatic forcing, The Cryosphere, 14, 599–632, https://doi.org/10.5194/tc-14-599-2020, 2020.

Allen, C. S., Pike, J., and Pudsey, C. J.: Last glacial–interglacial sea-ice cover in the SW Atlantic and its potential role in global deglaciation, Quaternary Science Reviews, 30, 2446–2458, https://doi.org/10.1016/j.quascirev.2011.04.002, 2011.

Alley, R. B., Andrews, J. T., Brigham-Grette, J., Clarke, G. K. C., Cuffey, K. M., Fitzpatrick, J. J., Funder, S., Marshall, S. J., Miller, G. H., Mitrovica, J. X., Muhs, D. R., Otto-Bliesner, B. L., Polyak, L., and White, J. W. C.: History of the Greenland Ice Sheet: paleoclimatic insights, Quaternary Science Reviews, 29, 1728–1756, https://doi.org/10.1016/j.quascirev.2010.02.007, 2010.

Andres, H. J. and Tarasov, L.: Towards understanding potential atmospheric contributions to abrupt climate changes: characterizing changes to the North Atlantic eddy-driven jet over the last deglaciation, Clim. Past, 15, 1621–1646, https://doi.org/10.5194/cp-15-1621-2019, 2019.

Applegate, P. J., Kirchner, N., Stone, E. J., Keller, K., and Greve, R.: An assessment of key model parametric uncertainties in projections of Greenland Ice Sheet behavior, The Cryosphere, 6, 589–606, https://doi.org/10.5194/tc-6-589-2012, 2012.

Aschwanden, A., Aðalgeirsdóttir, G., and Khroulev, C.: Hindcasting to measure ice sheet model sensitivity to initial states, The Cryosphere, 7, 1083–1093, https://doi.org/10.5194/tc-7-1083-2013, 2013.

Aschwanden, A., Fahnestock, M. A., Truffer, M., Brinkerhoff, D. J., Hock, R., Khroulev, C., Mottram, R., and Khan, S. A.: Contribution of the Greenland Ice Sheet to sea level over the next millennium, Sci. Adv., 5, eaav9396, https://doi.org/10.1126/sciadv.aav9396, 2019.

Axford, Y., Losee, S., Briner, J. P., Francis, D. R., Langdon, P. G., and Walker, I. R.: Holocene temperature history at the western Greenland Ice Sheet margin reconstructed from lake sediments, Quaternary Science Reviews, 59, 87–100, https://doi.org/10.1016/j.quascirev.2012.10.024, 2013.

Bahadory, T. and Tarasov, L.: LCice 1.0 – a generalized Ice Sheet System Model coupler for LOVECLIM version 1.3: description, sensitivities, and validation with the Glacial Systems Model (GSM version D2017.aug17), Geoscientific Model Development, 11, 3883–3902, https://doi.org/10.5194/gmd-11-3883-2018, 2018.

Bahadory, T., Tarasov, L., and Andres, H.: Last glacial inception trajectories for the Northern Hemisphere from coupled ice and climate modelling, Climate of the Past, 17, 397–418, https://doi.org/10.5194/cp-17-397-2021, 2021.

Bartlein, P. J. and Shafer, S. L.: Paleo calendar-effect adjustments in time-slice and transient climate-model simulations (PaleoCalAdjust v1.0): impact and strategies for data analysis, Geosci. Model Dev., 12, 3889–3913, https://doi.org/10.5194/gmd-12-3889-2019, 2019.

Bazin, L., Landais, A., Lemieux-Dudon, B., Toyé Mahamadou Kele, H., Veres, D., Parrenin, F., Martinerie, P., Ritz, C., Capron, E., Lipenkov, V., Loutre, M.-F., Raynaud, D., Vinther, B., Svensson, A., Rasmussen, S. O., Severi, M., Blunier, T., Leuenberger, M., Fischer, H., Masson-Delmotte, V., Chappellaz, J., and Wolff, E.: An optimized multi-proxy, multi-site Antarctic ice and gas orbital chronology (AICC2012): 120-800 ka, Climate of the Past, 9, 1715–1731, https://doi.org/10.5194/cp-9-1715-2013, 2013.

Beckmann, J., Perrette, M., Beyer, S., Calov, R., Willeit, M., and Ganopolski, A.: Modeling the response of Greenland outlet glaciers to global warming using a coupled flow line–plume model, The Cryosphere, 13, 2281–2301, https://doi.org/10.5194/tc-13-2281-2019, 2019.

Bereiter, B., Eggleston, S., Schmitt, J., Nehrbass-Ahles, C., Stocker, T. F., Fischer, H., Kipfstuhl, S., and Chappellaz, J.: Revision of the EPICA Dome C CO 2 record from 800 to 600 kyr before present: Analytical bias in the EDC CO2 record, Geophys. Res. Lett., 42, 542–549, https://doi.org/10.1002/2014GL061957, 2015.

Berger, A. and Loutre, M.-F.: Climate 400,000 years ago, a key to the future?, in: Earth's Climate and Orbital Eccentricity: The Marine Isotope Stage 11 Question, American Geophysical Union (AGU), 17–26, https://doi.org/10.1029/137GM02, 2003.

Berger, W. H. and Wefer, G.: On the Dynamics of The Ice Ages: Stage-11 Paradox, Mid-Brunhes Climate Shift, and 100-Ky Cycle, in: Earth's Climate and Orbital Eccentricity: The Marine Isotope Stage 11 Question, American Geophysical Union (AGU), 41–59, https://doi.org/10.1029/137GM04, 2003.

Bierman, P. R., Corbett, L. B., Graly, J. A., Neumann, T. A., Lini, A., Crosby, B. T., and Rood, D. H.: Preservation of a Preglacial Landscape Under the Center of the Greenland Ice Sheet, Science, 344, 402–405, https://doi.org/10.1126/science.1249047, 2014.

Bierman, P. R., Shakun, J. D., Corbett, L. B., Zimmerman, S. R., and Rood, D. H.: A persistent and dynamic East Greenland Ice Sheet over the past 7.5 million years, Nature, 540, 256–260, https://doi.org/10.1038/nature20147, 2016.

Bindschadler, R. A., Nowicki, S., Abe-Ouchi, A., Aschwanden, A., Choi, H., Fastook, J., Granzow, G., Greve, R., Gutowski, G., Herzfeld, U., Jackson, C., Johnson, J., Khroulev, C., Levermann, A., Lipscomb, W. H., Martin, M. A., Morlighem, M., Parizek, B. R., Pollard, D., Price, S. F., Ren, D., Saito, F., Sato, T., Seddik, H., Seroussi, H., Takahashi, K., Walker, R., and Wang, W. L.: Ice-sheet model sensitivities to environmental forcing and their use in projecting future sea level (the SeaRISE project), Journal of Glaciology, 59, 195–224, https://doi.org/10.3189/2013JoG12J125, 2013.

Born, A. and Nisancioglu, K. H.: Melting of Northern Greenland during the last interglaciation, The Cryosphere, 6, 1239–1250, https://doi.org/10.5194/tc-6-1239-2012, 2012.

Bosmans, J. H. C., Drijfhout, S. S., Tuenter, E., Hilgen, F. J., and Lourens, L. J.: Response of the North African summer monsoon to precession and obliquity forcings in the EC-Earth GCM, Clim. Dyn., 44, 279–297, https://doi.org/10.1007/s00382-014-2260-z, 2015.

Braconnot, P., Harrison, S. P., Kageyama, M., Bartlein, P. J., Masson-Delmotte, V., Abe-Ouchi, A., Otto-Bliesner, B., and Zhao, Y.: Evaluation of climate models using palaeoclimatic data, Nature Clim Change, 2, 417–424, https://doi.org/10.1038/nclimate1456, 2012.

Braconnot, P., Otto-Bliesner, B., Harrison, S., Joussaume, S., Peterchmitt, J.-Y., Abe-Ouchi, A., Crucifix, M., Driesschaert, E., Fichefet, T., Hewitt, C. D., Kageyama, M., Kitoh, A., Laîné, A., Loutre, M.-F., Marti, O., Merkel, U., Ramstein, G., Valdes, P., Weber, S. L., Yu, Y., and Zhao, Y.: Results of PMIP2 coupled simulations of the Mid-Holocene and Last Glacial Maximum - Part 1: experiments and large-scale features, Climate of the Past, 3, 261–277, https://doi.org/10.5194/cp-3-261-2007, 2007a.

Braconnot, P., Otto-Bliesner, B., Harrison, S., Joussaume, S., Peterchmitt, J.-Y., Abe-Ouchi, A., Crucifix, M., Driesschaert, E., Fichefet, T., Hewitt, C. D., Kageyama, M., Kitoh, A., Loutre, M.-F., Marti, O., Merkel, U., Ramstein, G., Valdes, P., Weber, L., Yu, Y., and Zhao, Y.: Results of PMIP2 coupled simulations of the Mid-Holocene and Last Glacial Maximum - Part 2: feedbacks with emphasis on the location of the ITCZ and mid- and high latitudes heat budget, Climate of the Past, 3, 279–296, https://doi.org/10.5194/cp-3-279-2007, 2007b.

Brierley, C. M., Zhao, A., Harrison, S. P., Braconnot, P., Williams, C. J. R., Thornalley, D. J. R., Shi, X., Peterschmitt, J.-Y., Ohgaito, R., Kaufman, D. S., Kageyama, M., Hargreaves, J. C., Erb, M. P., Emile-Geay, J., D'Agostino, R., Chandan, D., Carré, M., Bartlein, P. J., Zheng, W., Zhang, Z., Zhang, Q., Yang, H., Volodin, E. M., Tomas, R. A., Routson, C., Peltier, W. R., Otto-Bliesner, B., Morozova, P. A., McKay, N. P., Lohmann, G., Legrande, A. N., Guo, C., Cao, J., Brady, E., Annan, J. D., and Abe-Ouchi, A.: Large-scale features and evaluation of the PMIP4-CMIP6 midHolocene simulations, Clim. Past, 16, 1847–1872, https://doi.org/10.5194/cp-16-1847-2020, 2020.

Briner, J. P., Walcott, C. K., Schaefer, J. M., Young, N. E., MacGregor, J. A., Poinar, K., Keisling, B. A., Anandakrishnan, S., Albert, M. R., Kuhl, T., and Boeckmann, G.: Drill-site selection for cosmogenic-nuclide

exposure dating of the bed of the Greenland Ice Sheet, The Cryosphere, 16, 3933–3948, https://doi.org/10.5194/tc-16-3933-2022, 2022.

Calov, R., Robinson, A., Perrette, M., and Ganopolski, A.: Simulating the Greenland ice sheet under present-day and palaeo constraints including a new discharge parameterization, The Cryosphere, 9, 179–196, https://doi.org/10.5194/tc-9-179-2015, 2015.

Candy, I., Schreve, D. C., Sherriff, J., and Tye, G. J.: Marine Isotope Stage 11: Palaeoclimates, palaeoenvironments and its role as an analogue for the current interglacial, Earth-Science Reviews, 128, 18–51, https://doi.org/10.1016/j.earscirev.2013.09.006, 2014.

CAPE-Last Interglacial Project Members: Last Interglacial Arctic warmth confirms polar amplification of climate change, Quaternary Sci. Rev., 25, 1383–1400, 2006.

Capron, E., Rovere, A., Austermann, J., Axford, Y., Barlow, N. L. M., Carlson, A. E., de Vernal, A., Dutton, A., Kopp, R. E., McManus, J. F., Menviel, L., Otto-Bliesner, B. L., Robinson, A., Shakun, J. D., Tzedakis, P. C., and Wolff, E. W.: Challenges and research priorities to understand interactions between climate, ice sheets and global mean sea level during past interglacials, Quaternary Science Reviews, 219, 308–311, https://doi.org/10.1016/j.quascirev.2019.06.030, 2019.

Carter, J., Leeson, A., Orr, A., Kittel, C., and van Wessem, J. M.: Variability in Antarctic surface climatology across regional climate models and reanalysis datasets, The Cryosphere, 16, 3815–3841, https://doi.org/10.5194/tc-16-3815-2022, 2022.

Chen, Q.-S., Bromwich, D. H., and Bai, L.: Precipitation over Greenland retrieved by a dynamic method and its relation to cyclonic activity, J. Climate, 10, 839-870, https://doi.org/10.1175/1520-0442(1997)010%3C0839:POGRBA%3E2.0.CO;2, 1997.

Christ, A., Rittenour, T., Bierman, P., Keisling, B., Knutz, P., Thomsen, T., Keulen, N., Fosdick, J., Hemming, S., Tison, J.-L., Blard, P.-H., Steffensen, J., Caffee, M., Corbett, L., Dahl-Jensen, D., Dethier, D., Hidy, A., Perdrial, N., Peteet, D., and Thomas, E.: Deglaciation of northwestern Greenland during Marine Isotope Stage 11, Science (New York, N.Y.), 381, 330–335, https://doi.org/10.1126/science.ade4248, 2023.

Claussen, M., Mysak, L., Weaver, A., Crucifix, M., Fichefet, T., Loutre, M.-F., Weber, S., Alcamo, J., Alexeev, V., Berger, A., Calov, R., Ganopolski, A., Goosse, H., Lohmann, G., Lunkeit, F., Mokhov, I., Petoukhov, V., Stone, P., and Wang, Z.: Earth system models of intermediate complexity: closing the gap in the spectrum of climate system models, Climate Dynamics, 18, 579–586, https://doi.org/10.1007/s00382-001-0200-1, 2002.

Claussen, M.: Late Quaternary vegetation-climate feedbacks, Climate of the Past, 5, 203–216, https://doi.org/10.5194/cp-5-203-2009, 2009.

Coletti, A. J., DeConto, R. M., Brigham-Grette, J., and Melles, M.: A GCM comparison of Pleistocene super-interglacial periods in relation to Lake El'gygytgyn, NE Arctic Russia, Clim. Past, 11, 979–989, https://doi.org/10.5194/cp-11-979-2015, 2015.

Cronin, T. M., Polyak, L., Reed, D., Kandiano, E. S., Marzen, R. E., and Council, E. A.: A 600-ka Arctic sea-ice record from Mendeleev Ridge based on ostracodes, Quaternary Science Reviews, 79, 157–167, https://doi.org/10.1016/j.quascirev.2012.12.010, 2013.

Crow, B. R., Prange, M., and Schulz, M.: Dynamic boreal summer atmospheric circulation response as negative feedback to Greenland melt during the MIS-11 interglacial, Climate of the Past, 18, 775–792, https://doi.org/10.5194/cp-18-775-2022, 2022a.

Crow, B. R., Prange, M., and Schulz, M.: Exploring dynamic shifts in North Atlantic climate using CESMv1.2 time slice simulations of MIS-11c. PANGAEA, https://doi.org/10.1594/PANGAEA.942092, 2022b.

Crow, B. R., Tarasov, L., Schulz, M., and Prange, M.: Uncertainties originating from GCM downscaling and bias correction with application to the MIS-11c Greenland Ice Sheet, Climate of the Past, 20, 281-296, https://doi.org/10.5194/cp-20-281-2024, 2024.

Crucifix, M., Braconnot, P., Harrison, S. P., and Otto-Bliesner, B.: Second phase of paleoclimate modelling intercomparison project, Eos, Transactions American Geophysical Union, 86, 264–264, https://doi.org/10.1029/2005EO280003, 2005.

Dai, A., Luo, D., Song, M., and Liu, J.: Arctic amplification is caused by sea-ice loss under increasing CO2, Nat Commun, 10, 121, https://doi.org/10.1038/s41467-018-07954-9, 2019.

de Vernal, A. and Hillaire-Marcel, C.: Natural variability of Greenland climate, vegetation, and ice volume during the past million years, Science, 320, 1622–1625, https://doi.org/10.1126/science.1153929, 2008.

Decremer, D., Chung, C. E., Ekman, A. M. L., and Brandefelt, J.: Which significance test performs the best in climate simulations?, Tellus A: Dynamic Meteorology and Oceanography, 66, 23139, https://doi.org/10.3402/tellusa.v66.23139, 2014.

Diamond, R., Sime, L. C., Schroeder, D., and Guarino, M.-V.: The contribution of melt ponds to enhanced Arctic sea-ice melt during the Last Interglacial, The Cryosphere, 15, 5099–5114, https://doi.org/10.5194/tc-15-5099-2021, 2021.

Dickson, A. J., Beer, C. J., Dempsey, C., Maslin, M. A., Bendle, J. A., McClymont, E. L., and Pancost, R. D.: Oceanic forcing of the Marine Isotope Stage 11 interglacial, Nature Geosci, 2, 428–433, https://doi.org/10.1038/ngeo527, 2009.

Driesschaert, E., Fichefet, T., Goosse, H., Huybrechts, P., Janssens, I., Mouchet, A., Munhoven, G., Brovkin, V., and Weber, S. L.: Modeling the influence of Greenland ice sheet melting on the Atlantic meridional overturning circulation during the next millennia, Geophysical Research Letters, 34, https://doi.org/10.1029/2007GL029516, 2007.

Dutton, A., Carlson, A. E., Long, A. J., Milne, G. A., Clark, P. U., DeConto, R., Horton, B. P., Rahmstorf, S., and Raymo, M. E.: Sea-level rise due to polar ice-sheet mass loss during past warm periods, Science, 349, aaa4019, https://doi.org/10.1126/science.aaa4019, 2015.

(EPICA Community Members) Augustin, L., Barbante, C., Barnes, P. R. F., Marc Barnola, J., Bigler, M., Castellano, E., Cattani, O., Chappellaz, J., Dahl-Jensen, D., Delmonte, B., Dreyfus, G., Durand, G., Falourd, S., Fischer, H., Flückiger, J., Hansson, M. E., Huybrechts, P., Jugie, G., Johnsen, S. J., Jouzel, J., Kaufmann, P., Kipfstuhl, J., Lambert, F., Lipenkov, V. Y., Littot, G. C., Longinelli, A., Lorrain, R., Maggi, V., Masson-Delmotte, V., Miller, H., Mulvaney, R., Oerlemans, J., Oerter, H., Orombelli, G., Parrenin, F., Peel, D. A., Petit, J.-R., Raynaud, D., Ritz, C., Ruth, U., Schwander, J., Siegenthaler, U., Souchez, R., Stauffer, B., Peder Steffensen, J., Stenni, B., Stocker, T. F., Tabacco, I. E., Udisti, R., van de Wal, R. S. W., van den Broeke, M., Weiss, J., Wilhelms, F., Winther, J.-G., Wolff, E. W., Zucchelli, M., and EPICA community members:: Eight glacial cycles from an Antarctic ice core, Nature, 429, 623–628, https://doi.org/10.1038/nature02599, 2004.

Erokhina, O., Rogozhina, I., Prange, M., Bakker, P., Bernales, J., Paul, A., and Schulz, M.: Dependence of slope lapse rate over the Greenland ice sheet on background climate, J. Glaciol., 63, 568–572, https://doi.org/10.1017/jog.2017.10, 2017.

Extier, T., Landais, A., Bréant, C., Prié, F., Bazin, L., Dreyfus, G., Roche, D. M., and Leuenberger, M.: On the use of δ^{18}Oatm for ice core dating, Quaternary Science Reviews, 185, 244–257, https://doi.org/10.1016/j.quascirev.2018.02.008, 2018.

Fausto, R. S., Ahlstrøm, A. P., Van As, D., Bøggild, C. E., and Johnsen, S. J.: A new present-day temperature parameterization for Greenland, J. Glaciol., 55, 95–105, https://doi.org/10.3189/002214309788608985, 2009.

Fettweis, X., Box, J. E., Agosta, C., Amory, C., Kittel, C., Lang, C., van As, D., Machguth, H., and Gallée, H.: Reconstructions of the 1900–2015 Greenland ice sheet surface mass balance using the regional climate MAR model, The Cryosphere, 11, 1015–1033, https://doi.org/10.5194/tc-11-1015-2017, 2017.

Fischer, N. and Jungclaus, J. H.: Effects of orbital forcing on atmosphere and ocean heat transports in Holocene and Eemian climate simulations with a comprehensive Earth system model, Clim. Past, 6, 155-168, https://doi.org/10.5194/cp-6-155-2010, 2010.

Fitzgerald, P. W., Bamber, J. L., Ridley, J. K., and Rougier, J. C.: Exploration of parametric uncertainty in a surface mass balance model applied to the Greenland ice sheet, Journal of Geophysical Research: Earth Surface, 117, https://doi.org/10.1029/2011JF002067, 2012.

Fürst, J. J., Goelzer, H., and Huybrechts, P.: Ice-dynamic projections of the Greenland ice sheet in response to atmospheric and oceanic warming, The Cryosphere, 9, 1039–1062, https://doi.org/10.5194/tc-9-1039-2015, 2015.

Fyke, J. G., Weaver, A. J., Pollard, D., Eby, M., Carter, L., and Mackintosh, A.: A new coupled ice sheet/climate model: description and sensitivity to model physics under Eemian, Last Glacial Maximum, late Holocene and modern climate conditions, Geoscientific Model Development, 4, 117–136, https://doi.org/10.5194/gmd-4-117-2011, 2011.

Fyke, J., Eby, M., Mackintosh, A., and Weaver, A.: Impact of climate sensitivity and polar amplification on projections of Greenland Ice Sheet loss, Clim Dyn, 43, 2249–2260, https://doi.org/10.1007/s00382-014-2050-7, 2014.

Fyke, J., Sergienko, O., Löfverström, M., Price, S., and Lenaerts, J. T. M.: An overview of interactions and feedbacks between ice sheets and the Earth system, Rev. Geophys., 56, 361-408, https://doi.org/10.1029/2018RG000600, 2018.

Gallée, H. and Schayes, G.: Development of a Three-Dimensional Meso-γ Primitive Equation Model: Katabatic Winds Simulation in the Area of Terra Nova Bay, Antarctica, Monthly Weather Review, 122, 671–685, https://doi.org/10.1175/1520-0493(1994)122<0671:DOATDM>2.0.CO;2, 1994.

Ganopolski, A. and Calov, R.: The role of orbital forcing, carbon dioxide and regolith in 100 kyr glacial cycles, Clim. Past, 7, 1415-1425, https://doi.org/10.5194/cp-7-1415-2011, 2011.

Ganopolski, A., Winkelmann, R., and Schellnhuber, H. J.: Critical insolation–CO2 relation for diagnosing past and future glacial inception, Nature, 529, 200–203, https://doi.org/10.1038/nature16494, 2016.

Gardner, A. S., Sharp, M. J., Koerner, R. M., Labine, C., Boon, S., Marshall, S. J., Burgess, D. O., and Lewis, D.: Near-Surface Temperature Lapse Rates over Arctic Glaciers and Their Implications for Temperature Downscaling, Journal of Climate, 22, 4281–4298, https://doi.org/10.1175/2009JCLI2845.1, 2009.

Gent, P. R., Danabasoglu, G., Donner, L. J., Holland, M. M., Hunke, E. C., Jayne, S. R., Lawrence, D. M., Neale, R. B., Rasch, P. J., Vertenstein, M., Worley, P. H., Yang, Z.-L., and Zhang, M.: The Community Climate System Model Version 4, J. Climate, 24, 4973–4991, https://doi.org/10.1175/2011JCLI4083.1, 2011.

Gildor, H. and Tziperman, E.: A sea ice climate switch mechanism for the 100-kyr glacial cycles, Journal of Geophysical Research: Oceans, 106, 9117–9133, https://doi.org/10.1029/1999JC000120, 2001.

Goelzer, H., Huybrechts, P., Loutre, M.-F., and Fichefet, T.: Last Interglacial climate and sea-level evolution from a coupled ice sheet–climate model, Clim. Past, 12, 2195–2213, https://doi.org/10.5194/cp-12-2195-2016, 2016.

Goelzer, H., Robinson, A., Seroussi, H., and van de Wal, R. S. W.: Recent Progress in Greenland Ice Sheet Modelling, Curr Clim Change Rep, 3, 291–302, https://doi.org/10.1007/s40641-017-0073-y, 2017.

Goosse, H., Brovkin, V., Fichefet, T., Haarsma, R., Huybrechts, P., Jongma, J., Mouchet, A., Selten, F., Barriat, P.-Y., Campin, J.-M., Deleersnijder, E., Driesschaert, E., Goelzer, H., Janssens, I., Loutre, M.-F., Morales Maqueda, M. A., Opsteegh, T., Mathieu, P.-P., Munhoven, G., Pettersson, E. J., Renssen, H., Roche, D. M., Schaeffer, M., Tartinville, B., Timmermann, A., and Weber, S. L.: Description of the Earth system model of intermediate complexity LOVECLIM version 1.2, Geoscientific Model Development, 3, 603–633, https://doi.org/10.5194/gmd-3-603-2010, 2010.

Gupta, A. K.: Origin of agriculture and domestication of plants and animals linked to early Holocene climate amelioration, Current Science, 87, 54–59, 2004.

Hansen, B.: The Early History of Glacial Theory in British Geology, Journal of Glaciology, 9, 135–141, https://doi.org/10.3189/S0022143000026861, 1970.

Harvey, B. J., Cook, P., Shaffrey, L. C., and Schiemann, R.: The response of the Northern Hemisphere storm tracks and jet streams to climate change in the CMIP3, CMIP5, and CMIP6 climate models, J. Geophys. Res.-Atmos., 125, e2020JD032701, https://doi.org/10.1029/2020JD032701, 2020.

Hays, J. D., Imbrie, J., and Shackleton, N. J.: Variations in the Earth's Orbit: Pacemaker of the Ice Ages, Science, 194, 1121–1132, https://doi.org/10.1126/science.194.4270.1121, 1976.

Hearty, P. J., Hollin, J. T., Neumann, A. C., O'Leary, M. J., and McCulloch, M.: Global sea-level fluctuations during the Last Interglaciation (MIS 5e), Quaternary Science Reviews, 26, 2090–2112, https://doi.org/10.1016/j.quascirev.2007.06.019, 2007.

Hebeler, F., Purves, R. S., and Jamieson, S. S. R.: The impact of parametric uncertainty and topographic error in ice-sheet modelling, Journal of Glaciology, 54, 899–919, https://doi.org/10.3189/002214308787779852, 2008.

Helmke, J. P., Bauch, H. A., Röhl, U., and Kandiano, E. S.: Uniform climate development between the subtropical and subpolar Northeast Atlantic across marine isotope stage 11, Clim. Past, 4, 181–190, https://doi.org/10.5194/cp-4-181-2008, 2008.

Helsen, M. M., van de Berg, W. J., van de Wal, R. S. W., van den Broeke, M. R., and Oerlemans, J.: Coupled regional climate-ice-sheet simulation shows limited Greenland ice loss during the Eemian, Clim. Past, 9, 1773-1788, https://doi.org/10.5194/cp-9-1773-2013, 2013.

Herold, N., Yin, Q. Z., Karami, M. P., and Berger, A.: Modelling the climatic diversity of the warm interglacials, Quaternary Science Reviews, 56, 126–141, https://doi.org/10.1016/j.quascirev.2012.08.020, 2012.

Herrington, A. R., and Poulsen, C. J.: Terminating the Last Interglacial: the role of ice sheet-climate feedbacks in a GCM asynchronously coupled to an ice sheet model, J. Clim., 25, 1871-1882, https://doi.org/10.1175/JCLI-D-11-00218.1, 2011.

Hestmark, G.: Jens Esmark's mountain glacier traverse 1823 − the key to his discovery of Ice Ages, Boreas, 47, 1–10, https://doi.org/10.1111/bor.12260, 2018.

Hillaire-Marcel, C., de Vernal, A., and Crucifix, M., 2021: Sea-level and summer season orbital insolation as drivers of Arctic sea-ice. arXiv 2102, 02067, https://doi.org/10.48550/arXiv.2102.02067.

Hoyer, S. & Hamman, J.: xarray: N-D labeled Arrays and Datasets in Python. Journal of Open Research Software. 5(1), p.10., https://doi.org/10.5334/jors.148, 2017.

Hurrell, J. W., Holland, M. M., Gent, P. R., Ghan, S., Kay, J. E., Kushner, P. J., Lamarque, J.-F., Large, W. G., Lawrence, D., Lindsay, K., Lipscomb, W. H., Long, M. C., Mahowald, N., Marsh, D. R., Neale, R. B., Rasch, P., Vavrus, S., Vertenstein, M., Bader, D., Collins, W. D., Hack, J. J., Kiehl, J., and Marshall, S.: The Community Earth System Model: a framework for collaborative research, B. Am. Meteorol. Soc., 94, 1339–1360, https://doi.org/10.1175/BAMS-D-12-00121.1, 2013.

Huybers, P. and Wunsch, C.: Obliquity pacing of the late Pleistocene glacial terminations, Nature, 434, 491–494, https://doi.org/10.1038/nature03401, 2005.

Huybers, P.: Early Pleistocene Glacial Cycles and the Integrated Summer Insolation Forcing, Science, 313, 508–511, https://doi.org/10.1126/science.1125249, 2006.

Huybers, P. and Tziperman, E.: Integrated summer insolation forcing and 40,000-year glacial cycles: The perspective from an ice-sheet/energy-balance model, Paleoceanography, 23, https://doi.org/10.1029/2007PA001463, 2008.

Huybers, P.: Combined obliquity and precession pacing of late Pleistocene deglaciations, Nature, 480, 229–232, https://doi.org/10.1038/nature10626, 2011.

Huybrechts, P. and T'siobbel, S.: A three-dimensional climate—ice-sheet model applied to the Last Glacial Maximum, Annals of Glaciology, 25, 333–339, https://doi.org/10.3189/S0260305500014245, 1997.

Huybrechts, P. and Wolde, J. de: The Dynamic Response of the Greenland and Antarctic Ice Sheets to Multiple-Century Climatic Warming, Journal of Climate, 12, 2169–2188, https://doi.org/10.1175/1520-0442(1999)012<2169:TDROTG>2.0.CO;2, 1999.

Huybrechts, P.: A 3-D model for the Antarctic ice sheet: a sensitivity study on the glacial-interglacial contrast, Climate Dynamics, 5, 79–92, https://doi.org/10.1007/BF00207423, 1990.

IPCC: Climate Change 2001: The Scientific Basis. Contribution of Working Group I to the Third Assessment Report of the Intergovernmental Panel on Climate Change, edited by: Houghton, J.T., Ding, Y., Griggs, D. J., Noguer, M., van der Linden, P. J., Dai, X., Maskell, K., and Johnson, C. A., Cambridge University Press, Cambridge, United Kingdom and New York, NY, USA, 881 pp., 2001.

J. D. Hunter, "Matplotlib: A 2D Graphics Environment", Computing in Science & Engineering, vol. 9, no. 3, pp. 90-95, 2007.

Joussaume, S., Taylor, K.E.: Status of the Paleoclimate Modeling Intercomparison Project, in: Proceedings of the First International AMIP Scientific Conference, WCRP-92, Monterey, USA, pp. 425-430, 1995.

Joussaume, S. and Braconnot, P.: Sensitivity of paleoclimate simulation results to season definitions, Journal of Geophysical Research: Atmospheres, 102, 1943–1956, https://doi.org/10.1029/96JD01989, 1997.

Joussaume, S. and Taylor, K. E.: Paleoclimate Modelling Intercomparison Project (PMIP), Proceedings of the third PMIP workshop, 4–8 October 1999, edited by: Braconnot, P., 9–24, WCRP, Canada, La Huardiere, 1999.

Jouvet, G., Cohen, D., Russo, E., Buzan, J., Raible, C. C., Haeberli, W., Kamleitner, S., Ivy-Ochs, S., Imhof, M. A., Becker, J. K., Landgraf, A., and Fischer, U. H.: Coupled climate-glacier modelling of the last glaciation in the Alps, Journal of Glaciology, 1–15, https://doi.org/10.1017/jog.2023.74, 2023.

Jouzel, J., Masson-Delmotte, V., Cattani, O., Dreyfus, G., Falourd, S., Hoffmann, G., Minster, B., Nouet, J., Barnola, J. M., Chappellaz, J., Fischer, H., Gallet, J. C., Johnsen, S., Leuenberger, M., Loulergue, L., Luethi, D., Oerter, H., Parrenin, F., Raisbeck, G., Raynaud, D., Schilt, A., Schwander, J., Selmo, E., Souchez, R., Spahni, R., Stauffer, B., Steffensen, J. P., Stenni, B., Stocker, T. F., Tison, J. L., Werner, M., and Wolff, E. W.: Orbital and Millennial Antarctic Climate Variability over the Past 800,000 Years, Science, 317, 793–796, https://doi.org/10.1126/science.1141038, 2007.

Jungclaus, J. H., Bard, E., Baroni, M., Braconnot, P., Cao, J., Chini, L. P., Egorova, T., Evans, M., González-Rouco, J. F., Goosse, H., Hurtt, G. C., Joos, F., Kaplan, J. O., Khodri, M., Klein Goldewijk, K., Krivova, N., LeGrande, A. N., Lorenz, S. J., Luterbacher, J., Man, W., Maycock, A. C., Meinshausen, M., Moberg, A., Muscheler, R., Nehrbass-Ahles, C., Otto-Bliesner, B. I., Phipps, S. J., Pongratz, J., Rozanov, E., Schmidt, G. A., Schmidt, H., Schmutz, W., Schurer, A., Shapiro, A. I., Sigl, M., Smerdon, J. E., Solanki, S. K., Timmreck, C., Toohey, M., Usoskin, I. G., Wagner, S., Wu, C.-J., Yeo, K. L., Zanchettin, D., Zhang, Q., and Zorita, E.: The PMIP4 contribution to CMIP6 – Part 3: The last millennium, scientific objective, and experimental design for the PMIP4 past1000 simulations, Geosci. Model Dev., 10, 4005–4033, https://doi.org/10.5194/gmd-10-4005-2017, 2017.

Kageyama, M., Albani, S., Braconnot, P., Harrison, S. P., Hopcroft, P. O., Ivanovic, R. F., Lambert, F., Marti, O., Peltier, W. R., Peterschmitt, J.-Y., Roche, D. M., Tarasov, L., Zhang, X., Brady, E. C., Haywood, A. M., LeGrande, A. N., Lunt, D. J., Mahowald, N. M., Mikolajewicz, U., Nisancioglu, K. H., Otto-Bliesner, B. L., Renssen, H., Tomas, R. A., Zhang, Q., Abe-Ouchi, A., Bartlein, P. J., Cao, J., Li, Q., Lohmann, G., Ohgaito, R., Shi, X., Volodin, E., Yoshida, K., Zhang, X., and Zheng, W.: The PMIP4 contribution to CMIP6 – Part 4: Scientific objectives and experimental design of the PMIP4-CMIP6 Last Glacial Maximum experiments and PMIP4 sensitivity experiments, Geosci. Model Dev., 10, 4035–4055, https://doi.org/10.5194/gmd-10-4035-2017, 2017.

Kageyama, M., Sime, L. C., Sicard, M., Guarino, M.-V., de Vernal, A., Stein, R., Schroeder, D., Malmierca-Vallet, I., Abe-Ouchi, A., Bitz, C., Braconnot, P., Brady, E. C., Cao, J., Chamberlain, M. A., Feltham, D., Guo, C., LeGrande, A. N., Lohmann, G., Meissner, K. J., Menviel, L., Morozova, P., Nisancioglu, K. H., Otto-Bliesner, B. L., O'ishi, R., Ramos Buarque, S., Salas y Melia, D., Sherriff-Tadano, S., Stroeve, J., Shi, X., Sun, B., Tomas, R. A., Volodin, E., Yeung, N. K. H., Zhang, Q., Zhang, Z., Zheng, W., and Ziehn, T.: A multi-model CMIP6-PMIP4 study of Arctic sea ice at 127 ka: sea ice data compilation and model differences, Climate of the Past, 17, 37–62, https://doi.org/10.5194/cp-17-37-2021, 2021.

Kirchner, N., Hutter, K., Jakobsson, M., and Gyllencreutz, R.: Capabilities and limitations of numerical ice sheet models: a discussion for Earth-scientists and modelers, Quaternary Science Reviews, 30, 3691–3704, https://doi.org/10.1016/j.quascirev.2011.09.012, 2011.

Kleinen, T., Hildebrandt, S., Prange, M., Rachmayani, R., Müller, S., Bezrukova, E., Brovkin, V., and Tarasov, P. E.: The climate and vegetation of Marine Isotope Stage 11 – Model results and proxy-based reconstructions at global and regional scale, Quatern. Int., 348, 247–265, https://doi.org/10.1016/j.quaint.2013.12.028, 2014.

Kölling, M., Bouimetarhan, I., Bowles, M. W., Felis, T., Goldhammer, T., Hinrichs, K.-U., Schulz, M., and Zabel, M.: Consistent CO2 release by pyrite oxidation on continental shelves prior to glacial terminations, Nat. Geosci., 12, 929–934, https://doi.org/10.1038/s41561-019-0465-9, 2019.

Kremer, A., Stein, R., Fahl, K., Bauch, H., Mackensen, A., and Niessen, F.: A 190-ka biomarker record revealing interactions between sea ice, Atlantic Water inflow and ice sheet activity in eastern Fram Strait, Arktos, 4, 1–17, https://doi.org/10.1007/s41063-018-0052-0, 2018.

Kroon, D., Alexander, I., Little, M., Lourens, L. J., Matthewson, A., Robertson, A. H. F., and Sakamoto, T.: Oxygen isotope and sapropel stratigraphy in the Eastern Mediterranean during the last 3.2 million years, in: Ocean Drilling Program Scientific Results, 160, College Station, Texas, 181-190, https://doi.org/10.2973/odp.proc.sr.160.071.1998, 1998.

Laskar, J., Robutel, P., Joutel, F., Gastineau, M., Correia, A. C. M., and Levrard, B.: A long-term numerical solution for the insolation quantities of the Earth, Astron. Astrophys., 428, 261–285, https://doi.org/10.1051/0004-6361:20041335, 2004.

Le clec'h, S., Quiquet, A., Charbit, S., Dumas, C., Kageyama, M., and Ritz, C.: A rapidly converging initialisation method to simulate the present-day Greenland ice sheet using the GRISLI ice sheet model (version 1.3), Geosci. Model Dev., 12, 2481–2499, https://doi.org/10.5194/gmd-12-2481-2019, 2019.

Lee, S. and Kim, H.: The Dynamical Relationship between Subtropical and Eddy-Driven Jets, J. Atmos. Sci., 60, 1490–1503, https://doi.org/10.1175/1520-0469(2003)060<1490:TDRBSA>2.0.CO;2, 2003.

Lisiecki, L. E. and Raymo, M. E.: A Pliocene-Pleistocene stack of 57 globally distributed benthic $\delta^{18}O$ records, Paleoceanography, 20, PA1003, https://doi.org/10.1029/2004PA001071, 2005.

Lisiecki, L. E.: Links between eccentricity forcing and the 100,000-year glacial cycle, Nature Geosci, 3, 349–352, https://doi.org/10.1038/ngeo828, 2010.

Liu, X., Liu, J., Chen, S., Chen, J., Zhang, X., Yan, J., and Chen, F.: New insights on Chinese cave $\delta^{18}O$ records and their paleoclimatic significance, Earth-Science Reviews, 207, 103216, https://doi.org/10.1016/j.earscirev.2020.103216, 2020.

Lourens, L. J.: Revised tuning of Ocean Drilling Program Site 964 and KC01B (Mediterranean) and implications for the $\delta^{18}O$, tephra, calcareous nannofossil, and geomagnetic reversal chronologies of the past 1.1 Myr, Paleoceanography, 19, PA3010, https://doi.org/10.1029/2003PA000997, 2004.

Loutre, M. F. and Berger, A.: Future Climatic Changes: Are We Entering an Exceptionally Long Interglacial?, Climatic Change, 46, 61–90, https://doi.org/10.1023/A:1005559827189, 2000.

Lüthi, D., Le Floch, M., Bereiter, B., Blunier, T., Barnola, J.-M., Siegenthaler, U., Raynaud, D., Jouzel, J., Fischer, H., Kawamura, K., and Stocker, T. F.: High-resolution carbon dioxide concentration record 650 000–800 000 years before present, Nature, 453, 379–382, https://doi.org/10.1038/nature06949, 2008.

Ma, Y., Gagliardini, O., Ritz, C., Gillet-Chaulet, F., Durand, G., and Montagnat, M.: Enhancement factors for grounded ice and ice shelves inferred from an anisotropic ice-flow model, Journal of Glaciology, 56, 805–812, https://doi.org/10.3189/002214310794457209, 2010.

Mantsis, D. F., Lintner, B. R., Broccoli, A. J., Erb, M. P., Clement, A. C., and Park, H.-S.: The response of large-scale circulation to obliquity-induced changes in meridional heating gradients, J. Climate, 27, 5504–5516, https://doi.org/10.1175/JCLI-D-13-00526.1, 2014.

Marshall, S. J.: Recent advances in understanding ice sheet dynamics, Earth and Planetary Science Letters, 240, 191–204, https://doi.org/10.1016/j.epsl.2005.08.016, 2005.

Mas e Braga, M., Bernales, J., Prange, M., Stroeven, A. P., and Rogozhina, I.: Sensitivity of the Antarctic ice sheets to the warming of marine isotope substage 11c, The Cryosphere, 15, 459–478, https://doi.org/10.5194/tc-15-459-2021, 2021.

Masson-Delmotte, V., Stenni, B., Pol, K., Braconnot, P., Cattani, O., Falourd, S., Kageyama, M., Jouzel, J., Landais, A., Minster, B., Barnola, J. M., Chappellaz, J., Krinner, G., Johnsen, S., Röthlisberger, R., Hansen, J., Mikolajewicz, U., and Otto-Bliesner, B.: EPICA Dome C record of glacial and interglacial intensities, Quaternary Sci. Rev., 29, 113–128, https://doi.org/10.1016/j.quascirev.2009.09.030, 2010.

Matthiessen, J., Knies, J., Nowaczyk, N. R., and Stein, R.: Late Quaternary dinoflagellate cyst stratigraphy at the Eurasian continental margin, Arctic Ocean: Indications for Atlantic water inflow in the past 150,000 years. Global and Planetary Change, 31(1-4), 65-86, https://doi.org/10.1016/S0921-8181(01)00113-8, 2001a.

Matthiessen, J. Knies, J., Nowaczyk, N. R., and Stein, R.: Late Quaternary dinoflagellate cysts at the Eurasian continental margin, Arctic Ocean. PANGAEA, https://doi.org/10.1594/PANGAEA.728133, 2001b.

Melles, M., Brigham-Grette, J., Minyuk, P. S., Nowaczyk, N. R., Wennrich, V., DeConto, R. M., Anderson, P. M., Andreev, A. A., Coletti, A., Cook, T. L., Haltia-Hovi, E., Kukkonen, M., Lozhkin, A. V., Rosén, P., Tarasov, P., Vogel, H., and Wagner, B.: 2.8 million years of Arctic climate change from Lake El'gygytgyn, NE Russia, Science, 337, 315–320, https://doi.org/10.1126/science.1222135, 2012.

Merz, N., Born, A., Raible, C. C., Fischer, H., and Stocker, T. F.: Dependence of Eemian Greenland temperature reconstructions on the ice sheet topography, Clim. Past, 10, 1221–1238, https://doi.org/10.5194/cp-10-1221-2014, 2014.

Merz, N., Raible, C. C., and Woollings, T.: North Atlantic eddy-driven jet in interglacial and glacial winter climates, J. Climate, 28, 3977–3997, https://doi.org/10.1175/JCLI-D-14-00525.1, 2015.

Merz, N., Born, A., Raible, C. C., and Stocker, T. F.: Warm Greenland during the last interglacial: the role of regional changes in sea ice cover, Clim. Past, 12, 2011-2031, https://doi.org/10.5194/cp-12-2011-2016, 2016.

Miettinen, A., Head, M. J., and Knudsen, K. L.: Eemian sea-level highstand in the eastern Baltic Sea linked to long-duration White Sea connection, Quaternary Science Reviews, 86, 158–174, https://doi.org/10.1016/j.quascirev.2013.12.009, 2014.

Milankovitch, M.: Kanon der Erdbestrahlung und seine Anwendung auf des Eiszeitenproblem. Special Publication 132, Section of Mathematical and Natural Sciences, vol. 33, p. 633, Royal Serbian Academy of Sciences, Belgrade, Serbia ("Canon of Insolation and the Ice Age Problem") (trans. Israel Program for the US Department of Commerce and the National Science Foundation, Washington, D.C., USA, 1969, and by Zavod za udzbenike i nastavna sredstva in cooperation with Muzej nauke i tehnike Srpske akademije nauka i umetnosti, Belgrade, Serbia, 1998), 1941.

Milker, Y., Rachmayani, R., Weinkauf, M. F. G., Prange, M., Raitzsch, M., Schulz, M., and Kučera, M.: Global and regional sea surface temperature trends during Marine Isotope Stage 11, Clim. Past, 9, 2231–2252, https://doi.org/10.5194/cp-9-2231-2013, 2013.

Mohtadi, M., Prange, M., and Steinke, S.: Palaeoclimatic insights into forcing and response of monsoon rainfall, Nature, 533, 191–199, https://doi.org/10.1038/nature17450, 2016.

Montoya, M., Griesel, A., Levermann, A., Mignot, J., Hofmann, M., Ganopolski, A., and Rahmstorf, S.: The earth system model of intermediate complexity CLIMBER-3α. Part I: description and performance for present-day conditions, Clim Dyn, 25, 237–263, https://doi.org/10.1007/s00382-005-0044-1, 2005.

Morlighem, M., Williams, C. N., Rignot, E., An, L., Arndt, J. E., Bamber, J. L., Catania, G., Chauché, N., Dowdeswell, J. A., Dorschel, B., Fenty, I., Hogan, K., Howat, I., Hubbard, A., Jakobsson, M., Jordan, T. M., Kjeldsen, K. K., Millan, R., Mayer, L., Mouginot, J., Noël, B. P. Y., O'Cofaigh, C., Palmer, S., Rysgaard, S., Seroussi, H., Siegert, M. J., Slabon, P., Straneo, F., van den Broeke, M. R., Weinrebe, W., Wood, M., and Zinglersen, K. B.: BedMachine v3: complete bed topography and ocean bathymetry mapping of Greenland from multibeam echo sounding combined with mass conservation, Geophys. Res. Lett., 44, 11,051-11,061, https://doi.org/10.1002/2017GL074954, 2017.

Nakamura, N. and Oort, A. H.: Atmospheric heat budgets of the polar regions, J. Geophys. Res.-Atmos., 93, 9510–9524, https://doi.org/10.1029/JD093iD08p09510, 1988.

Nakamura, H. and Sampe, T.: Trapping of synoptic-scale disturbances into the North-Pacific subtropical jet core in midwinter, Geophys. Res. Lett., 29, 8-1-8-4, https://doi.org/10.1029/2002GL015535, 2002.

Neale, R. B., Gettelman, A., Park, S., Chen, C. -C., Lauritzen, P. H., Williamson, D. L., Conley, A. J., Kinnison, D., Marsh, D., Smith, A. K., Vitt, F. M., Garcia, R., Lamarque, J.-F., Mills, M. J., Tilmes, S., Morrison, H., Cameron-Smith, P., Collins, W. D., Iacono, M. J., Easter, R. C., Liu, X., Ghan, S. J., Rasch, P. J., and Taylor, M. A.: Description of the NCAR Community Atmosphere Model (CAM 5.0). NCAR Tech. Note NCAR/TN-486+STR. doi:10.5065/wgtk-4g06, 2012.

NEEM community members: Eemian interglacial reconstructed from a Greenland folded ice core, Nature, 493, 489–494, 2013.

(NGRIP Members) Andersen, K. K., Azuma, N., Barnola, J.-M., Bigler, M., Biscaye, P., Caillon, N., Chappellaz, J., Clausen, H. B., Dahl-Jensen, D., Fischer, H., Flückiger, J., Fritzsche, D., Fujii, Y., Goto-Azuma, K., Grønvold, K., Gundestrup, N. S., Hansson, M., Huber, C., Hvidberg, C. S., Johnsen, S. J., Jonsell, U., Jouzel,

J., Kipfstuhl, S., Landais, A., Leuenberger, M., Lorrain, R., Masson-Delmotte, V., Miller, H., Motoyama, H., Narita, H., Popp, T., Rasmussen, S. O., Raynaud, D., Rothlisberger, R., Ruth, U., Samyn, D., Schwander, J., Shoji, H., Siggard-Andersen, M.-L., Steffensen, J. P., Stocker, T., Sveinbjörnsdóttir, A. E., Svensson, A., Takata, M., Tison, J.-L., Thorsteinsson, Th., Watanabe, O., Wilhelms, F., White, J. W. C., and North Greenland Ice Core Project members: High-resolution record of Northern Hemisphere climate extending into the last interglacial period, Nature, 431, 147–151, https://doi.org/10.1038/nature02805, 2004.

Noël, B., van de Berg, W. J., van Wessem, J. M., van Meijgaard, E., van As, D., Lenaerts, J. T. M., Lhermitte, S., Kuipers Munneke, P., Smeets, C. J. P. P., van Ulft, L. H., van de Wal, R. S. W., and van den Broeke, M. R.: Modelling the climate and surface mass balance of polar ice sheets using RACMO2 – Part 1: Greenland (1958–2016), The Cryosphere, 12, 811–831, https://doi.org/10.5194/tc-12-811-2018, 2018.

NorthGRIP: High-resolution record of Northern Hemisphere climate extending into the last interglacial period, Nature, 431, 147151, 2004.

Otto-Bliesner, B. L., Marshall, S. J., Overpeck, J. T., Miller, G. H., Hu, A., and CAPE Last Interglacial Project Members: Simulating Arctic Climate Warmth and Icefield Retreat in the Last Interglaciation, Science, 311, 1751–1753, https://doi.org/10.1126/science.1120808, 2006.

Otto-Bliesner, B. L., Rosenbloom, N., Stone, E. J., McKay, N. P., Lunt, D. J., Brady, E. C., and Overpeck, J. T.: How warm was the last interglacial? New model–data comparisons, Proc. R. Soc. A, 371, 20130097, https://doi.org/10.1098/rsta.2013.0097, 2013.

Otto-Bliesner, B. L., Braconnot, P., Harrison, S. P., Lunt, D. J., Abe-Ouchi, A., Albani, S., Bartlein, P. J., Capron, E., Carlson, A. E., Dutton, A., Fischer, H., Goelzer, H., Govin, A., Haywood, A., Joos, F., LeGrande, A. N., Lipscomb, W. H., Lohmann, G., Mahowald, N., Nehrbass-Ahles, C., Pausata, F. S. R., Peterschmitt, J.-Y., Phipps, S. J., Renssen, H., and Zhang, Q.: The PMIP4 contribution to CMIP6 – Part 2: Two interglacials, scientific objective and experimental design for Holocene and Last Interglacial simulations, Geosci. Model Dev., 10, 3979–4003, https://doi.org/10.5194/gmd-10-3979-2017, 2017.

Overland, J. E. and Turet, P.: Variability of the atmospheric energy flux across 70°N computed from the GFDL data set, in: The Polar Oceans and Their Role in Shaping the Global Environment, edited by: Johnnessen, O. M., Muench, R. D., and Overland, J. E., American Geophysical Union, Washington, D. C., https://doi.org/10.1029/GM085p0313, 1994.

O'ishi, R., Chan, W.-L., Abe-Ouchi, A., Sherriff-Tadano, S., Ohgaito, R., and Yoshimori, M.: PMIP4/CMIP6 last interglacial simulations using three different versions of MIROC: importance of vegetation, Climate of the Past, 17, 21–36, https://doi.org/10.5194/cp-17-21-2021, 2021.

Pante, G. and Knippertz, P.: Resolving Sahelian thunderstorms improves mid-latitude weather forecasts, Nat. Commun, 10, 3487, https://doi.org/10.1038/s41467-019-11081-4, 2019.

Park, H.-S., Kim, S.-J., Stewart, A. L., Son, S.-W., and Seo, K.-H.: Mid-Holocene Northern Hemisphere warming driven by Arctic amplification, Science Advances, 5, eaax8203, https://doi.org/10.1126/sciadv.aax8203, 2019.

Parrenin, F., Jouzel, J., Kawamura, K., Lemieux-Dudon, B., Loulergue, L., Masson-Delmotte, V., Narcisi, B., Raisbeck, G., Raynaud, D., Ruth, U., Schwander, J., Severi, M., Spahni, R., Steffensen, J. P., Svensson, A., Udisti, R., Waelbroeck, C., and Wolff, E.: The EDC3 chronology for the EPICA Dome C ice core, Clim. Past, 13, 2007.

Past Interglacials Working Group of PAGES: Interglacials of the last 800,000 years: Interglacials of the Last 800,000 Years, Rev. Geophys., 54, 162–219, https://doi.org/10.1002/2015RG000482, 2016.

Pedersen, R. A. and Christensen, J. H.: Attributing Greenland Warming Patterns to Regional Arctic Sea Ice Loss, Geophysical Research Letters, 46, 10495–10503, https://doi.org/10.1029/2019GL083828, 2019.

Perovich, D. K., Grenfell, T. C., Light, B., and Hobbs, P. V.: Seasonal evolution of the albedo of multiyear Arctic sea ice, Journal of Geophysical Research: Oceans, 107, SHE 20-1-SHE 20-13, https://doi.org/10.1029/2000JC000438, 2002.

Petit, J. R., Jouzel, J., Raynaud, D., Barkov, N. I., Barnola, J.-M., Basile, I., Bender, M., Chappellaz, J., Davis, M., Delaygue, G., Delmotte, M., Kotlyakov, V. M., Legrand, M., Lipenkov, V. Y., Lorius, C., PÉpin, L., Ritz, C.,

Saltzman, E., and Stievenard, M.: Climate and atmospheric history of the past 420,000 years from the Vostok ice core, Antarctica, Nature, 399, 429–436, https://doi.org/10.1038/20859, 1999.

Petoukhov, V., Ganopolski, A., Brovkin, V., Claussen, M., Eliseev, A., Kubatzki, C., and Rahmstorf, S.: CLIMBER-2: a climate system model of intermediate complexity. Part I: model description and performance for present climate, Climate Dynamics, 16, 1–17, https://doi.org/10.1007/PL00007919, 2000.

Pollard, D. and Reusch, D. B.: A calendar conversion method for monthly mean paleoclimate model output with orbital forcing, Journal of Geophysical Research: Atmospheres, 107, ACL 3-1-ACL 3-7, https://doi.org/10.1029/2002JD002126, 2002.

Pollard, D. and DeConto, R.: Description of a hybrid ice sheet-shelf model, and application to Antarctica, Geoscientific Model Development, 5, 1273-1295, 2012.

Pollard, D., DeConto, R. M., and Alley, R. B.: Potential Antarctic Ice Sheet retreat driven by hydrofracturing and ice cliff failure, Earth and Plan. Sci. Let., 412, 112-121, https://doi.org/10.1016/j.epsl.2014.12.035, 2015.

Pritchard, M. S., Bush, A. B. G., and Marshall, S. J.: Neglecting ice-atmosphere interactions underestimates ice sheet melt in millennial-scale deglaciation simulations, Geophys. Res. Lett., 35, L01503, https://doi.org/10.1029/2007GL031738, 2008.

Quiquet, A., Punge, H. J., Ritz, C., Fettweis, X., Gallée, H., Kageyama, M., Krinner, G., Salas y Mélia, D., and Sjolte, J.: Sensitivity of a Greenland ice sheet model to atmospheric forcing fields, The Cryosphere, 6, 999–1018, https://doi.org/10.5194/tc-6-999-2012, 2012.

Rachmayani, R., Prange, M., and Schulz, M.: Intra-interglacial climate variability: model simulations of Marine Isotope Stages 1, 5, 11, 13, and 15, Clim. Past, 12, 677–695, https://doi.org/10.5194/cp-12-677-2016, 2016.

Rachmayani, R., Prange, M., Lunt, D. J., Stone, E. J., and Schulz, M.: Sensitivity of the Greenland Ice Sheet to Interglacial Climate Forcing: MIS 5e Versus MIS 11, Paleoceanography, 32, 1089–1101, https://doi.org/10.1002/2017PA003149, 2017.

Raymo, M. E. and Mitrovica, J. X.: Collapse of polar ice sheets during the stage 11 interglacial, Nature, 483, 453–456, https://doi.org/10.1038/nature10891, 2012.

Raynaud, D., Chappellaz, J., Ritz, C., and Martinerie, P.: Air content along the Greenland Ice Core Project core: A record of surface climatic parameters and elevation in central Greenland, J. Geophys. Res., 102, 26607–26613, 1997.

Reeh, N., Parameterization of melt rate and surface temperature on the Greenland ice sheet. Polarforschung, 59(3), 113–128, 1991.

Reijmer, C. H., van den Broeke, M. R., Fettweis, X., Ettema, J., and Stap, L. B.: Refreezing on the Greenland ice sheet: a comparison of parameterizations, The Cryosphere, 6, 743–762, https://doi.org/10.5194/tc-6-743-2012, 2012.

Rennermalm, A. K., Smith, L. C., Stroeve, J. C., and Chu, V. W.: Does sea ice influence Greenland ice sheet surface-melt?, Environ. Res. Lett., 4, 024011, https://doi.org/10.1088/1748-9326/4/2/024011, 2009.

Renssen, H., Seppä, H., Crosta, X., Goosse, H., and Roche, D. M.: Global characterization of the Holocene Thermal Maximum, Quaternary Science Reviews, 48, 7–19, https://doi.org/10.1016/j.quascirev.2012.05.022, 2012.

Reyes, A. V., Carlson, A. E., Beard, B. L., Hatfield, R. G., Stoner, J. S., Winsor, K., Welke, B., and Ullman, D. J.: South Greenland ice-sheet collapse during Marine Isotope Stage 11, Nature, 510, 525–528, https://doi.org/10.1038/nature13456, 2014.

Ridley, J. K., Huybrechts, P., Gregory, J. M., and Lowe, J. A.: Elimination of the Greenland Ice Sheet in a high CO_2 climate, J. Clim., 18, 3409-3427, https://doi.org/10.1175/JCLI3482.1, 2005.

Ridley, J., Gregory, J. M., Huybrechts, P., and Lowe, J.: Thresholds for irreversible decline of the Greenland ice sheet, Clim Dyn, 35, 1049–1057, https://doi.org/10.1007/s00382-009-0646-0, 2010.

Ritz, C., Fabre, A., and Letréguilly, A.: Sensitivity of a Greenland ice sheet model to ice flow and ablation parameters: consequences for the evolution through the last climatic cycle, Climate Dynamics, 13, 11–23, https://doi.org/10.1007/s003820050149, 1996.

Robinson, A., Calov, R., and Ganopolski, A.: An efficient regional energy-moisture balance model for simulation of the Greenland Ice Sheet response to climate change, The Cryosphere, 4, 129-144, https://doi.org/10.5194/tc-4-129-2010, 2010.

Robinson, A., Alvarez-Solas, J., Calov, R., Ganopolski, A., and Montoya, M.: MIS-11 duration key to disappearance of the Greenland ice sheet, Nat. Commun., 8, 16008, https://doi.org/10.1038/ncomms16008, 2017.

Rogozhina, I., Martinec, Z., Hagedoorn, J. M., Thomas, M., and Fleming, K.: On the long-term memory of the Greenland Ice Sheet, Journal of Geophysical Research: Earth Surface, 116, F01011, https://doi.org/10.1029/2010JF001787, 2011.

Rohling, E. J., Hibbert, F. D., Grant, K. M., Galaasen, E. V., Irvalı, N., Kleiven, H. F., Marino, G., Ninnemann, U., Roberts, A. P., Rosenthal, Y., Schulz, H., Williams, F. H., and Yu, J.: Asynchronous Antarctic and Greenland ice-volume contributions to the last interglacial sea-level highstand, Nat Commun, 10, 5040, https://doi.org/10.1038/s41467-019-12874-3, 2019.

Schaefer, J. M., Finkel, R. C., Balco, G., Alley, R. B., Caffee, M. W., Briner, J. P., Young, N. E., Gow, A. J., and Schwartz, R.: Greenland was nearly ice-free for extended periods during the Pleistocene, Nature, 540, 252–255, https://doi.org/10.1038/nature20146, 2016.

Sellevold, R., van Kampenhout, L., Lenaerts, J. T. M., Noël, B., Lipscomb, W. H., and Vizcaino, M.: Surface mass balance downscaling through elevation classes in an Earth system model: application to the Greenland ice sheet, The Cryosphere, 13, 3193–3208, https://doi.org/10.5194/tc-13-3193-2019, 2019.

Sellevold, R., Lenaerts, J. T. M., and Vizcaino, M.: Influence of Arctic sea-ice loss on the Greenland ice sheet climate, Clim Dyn, 58, 179–193, https://doi.org/10.1007/s00382-021-05897-4, 2022.

Serreze, M. C. and Francis, J. A.: The Arctic Amplification Debate, Climatic Change, 76, 241–264, https://doi.org/10.1007/s10584-005-9017-y, 2006.

Serreze, M. C., Barrett, A. P., Slater, A. G., Steele, M., Zhang, J., and Trenberth, K. E.: The large-scale energy budget of the Arctic, J. Geophys. Res., 112, D11122, https://doi.org/10.1029/2006JD008230, 2007.

Serreze, M. C. and Barrett, A. P.: Characteristics of the Beaufort Sea High, Journal of Climate, 24, 159–182, https://doi.org/10.1175/2010JCLI3636.1, 2011.

Sicard, M., Kageyama, M., Charbit, S., Braconnot, P., and Madeleine, J.-B.: An energy budget approach to understand the Arctic warming during the Last Interglacial, Climate of the Past, 18, 607–629, https://doi.org/10.5194/cp-18-607-2022, 2022.

Siegenthaler, U., Stocker, T. F., Monnin, E., Lüthi, D., Schwander, J., Stauffer, B., Raynaud, D., Barnola, J.-M., Fischer, H., Masson-Delmotte, V., and Jouzel, J.: Stable Carbon Cycle-Climate Relationship During the Late Pleistocene, Science, 310, 1313–1317, https://doi.org/10.1126/science.1120130, 2005.

Sigman, D. M., Hain, M. P., and Haug, G. H.: The polar ocean and glacial cycles in atmospheric CO2 concentration, Nature, 466, 47–55, https://doi.org/10.1038/nature09149, 2010.

Sime, L. C., Sivankutty, R., Vallet-Malmierca, I., de Boer, A. M., and Sicard, M.: Summer surface air temperature proxies point to near-sea-ice-free conditions in the Arctic at 127 ka, Climate of the Past, 19, 883–900, https://doi.org/10.5194/cp-19-883-2023, 2023.

Smith, R. S. and Gregory, J.: The last glacial cycle: transient simulations with an AOGCM, Clim Dyn, 38, 1545–1559, https://doi.org/10.1007/s00382-011-1283-y, 2012.

Sommers, A. N., Otto-Bliesner, B. L., Lipscomb, W. H., Lofverstrom, M., Shafter, S. L., Bartlein, P. J., Brady, E. C., Kluzek, E., Leguy, G., Thayer-Calder, K., and Tomas, R. A.: Retreat and regrowth of the Greenland Ice Sheet during the Last Interglacial as simulated by the CESM2-CISM2 coupled climate-ice sheet model, Paleoceanography and Paleoclimatology, 36, e2021PA004272, https://doi.org/10.1029/2021PA004272, 2021.

Son, S.-W. and Lee, S.: The response of westerly jets to thermal driving in a primitive equation model, J. Atmos. Sci., 62, 3741–3757, https://doi.org/10.1175/JAS3571.1, 2005.

Steger, C. R., Reijmer, C. H., and van den Broeke, M. R.: The modelled liquid water balance of the Greenland Ice Sheet, The Cryosphere, 11, 2507–2526, https://doi.org/10.5194/tc-11-2507-2017, 2017.

Stone, E. J., Lunt, D. J., Rutt, I. C., and Hanna, E.: Investigating the sensitivity of numerical model simulations of the modern state of the Greenland ice-sheet and its future response to climate change, The Cryosphere, 4, 397–417, https://doi.org/10.5194/tc-4-397-2010, 2010.

Stone, E. J., Lunt, D. J., Annan, J. D., and Hargreaves, J. C.: Quantification of the Greenland ice sheet contribution to Last Interglacial sea level rise, Clim. Past, 9, 621–639, https://doi.org/10.5194/cp-9-621-2013, 2013.

Tarasov, L. and Peltier, W. R.: A high-resolution model of the 100 ka ice-age cycle, Annals of Glaciology, 25, 58–65, https://doi.org/10.3189/S026030550001380X, 1997.

Tarasov, L. and Peltier, W. R.: Greenland glacial history and local geodynamic consequences, Geophysical Journal International, 150, 198–229, https://doi.org/10.1046/j.1365-246X.2002.01702.x, 2002.

Tarasov, L. and Peltier, W. R.: Greenland glacial history, borehole constraints, and Eemian extent, Journal of Geophysical Research: Solid Earth, 108, https://doi.org/10.1029/2001JB001731, 2003.

Tarasov, L. and Peltier, W. R.: A geophysically constrained large ensemble analysis of the deglacial history of the North American ice-sheet complex, Quaternary Science Reviews, 23, 359–388, https://doi.org/10.1016/j.quascirev.2003.08.004, 2004.

Tarasov, L. and Peltier, W. R.: Coevolution of continental ice cover and permafrost extent over the last glacial-interglacial cycle in North America, Journal of Geophysical Research: Earth Surface, 112, F02S08, https://doi.org/10.1029/2006JF000661, 2007.

Tarasov, L. and Goldstein, M.: Assessing uncertainty in past ice and climate evolution: overview, stepping-stones, and challenges, EGUsphere [preprint], https://doi.org/10.5194/egusphere-2022-1410, 2023.

Tarasov, L., Hank, K., and Lecavalier, B.: The glacial systems model (GSM) V22c, in prep., 2024.

Thomas, Z. A., Jones, R. T., Turney, C. S. M., Golledge, N., Fogwill, C., Bradshaw, C. J. A., Menviel, L., McKay, N. P., Bird, M., Palmer, J., Kershaw, P., Wilmshurst, J., and Muscheler, R.: Tipping elements and amplified polar warming during the Last Interglacial, Quaternary Science Reviews, 233, 106222, https://doi.org/10.1016/j.quascirev.2020.106222, 2020.

Thomson, D. J.: Spectrum estimation and harmonic analysis, P. IEEE, 70, 1055–1096, https://doi.org/10.1109/PROC.1982.12433, 1982.

Tzedakis, P. C., Hodell, D. A., Nehrbass-Ahles, C., Mitsui, T., and Wolff, E. W.: Marine Isotope Stage 11c: An unusual interglacial, Quaternary Science Reviews, 284, 107493, https://doi.org/10.1016/j.quascirev.2022.107493, 2022.

Van Nieuwenhove, N., Bauch, H. A., Eynaud, F., Kandiano, E., Cortijo, E., and Turon, J.-L.: Evidence for delayed poleward expansion of North Atlantic surface waters during the last interglacial (MIS 5e), Quaternary Science Reviews, 30, 934–946, https://doi.org/10.1016/j.quascirev.2011.01.013, 2011.

Varma, V., Prange, M., and Schulz, M.: Transient simulations of the present and the last interglacial climate using the Community Climate System Model version 3: effects of orbital acceleration, Geosci. Model Dev., 9, 3859-3873, https://doi.org/10.5194/gmd-9-3859-2016, 2016.

Vermassen, F., O'Regan, M., de Boer, A., Schenk, F., Razmjooei, M., West, G., Cronin, T. M., Jakobsson, M., and Coxall, H. K.: A seasonally ice-free Arctic Ocean during the Last Interglacial, Nat. Geosci., 16, 723–729, https://doi.org/10.1038/s41561-023-01227-x, 2023.

Vizcaíno, M., Mikolajewicz, U., Gröger, M., Maier-Reimer, E., Schurgers, G., and Winguth, A. M. E.: Long-term ice sheet–climate interactions under anthropogenic greenhouse forcing simulated with a complex Earth System Model, Clim Dyn, 31, 665–690, https://doi.org/10.1007/s00382-008-0369-7, 2008.

Vizcaíno, M.: Ice sheets as interactive components of Earth System Models: progress and challenges, WIREs Climate Change, 5, 557–568, https://doi.org/10.1002/wcc.285, 2014.

Wang, L., Deng, A., and Huang, R.: Wintertime internal climate variability over Eurasia in the CESM large ensemble, Clim. Dynamics, 52, 6735-6748, https://doi.org/10.1007/s00382-018-4542-3, 2019.

Weaver, A. J., Eby, M., Wiebe, E. C., Bitz, C. M., Duffy, P. B., Ewen, T. L., Fanning, A. F., Holland, M. M., MacFadyen, A., Matthews, H. D., Meissner, K. J., Saenko, O., Schmittner, A., Wang, H., and Yoshimori, M.:

The UVic earth system climate model: Model description, climatology, and applications to past, present and future climates, Atmosphere-Ocean, 39, 361–428, https://doi.org/10.1080/07055900.2001.9649686, 2001.

Willerslev, E., Cappellini, E., Boomsma, W., Nielsen, R., Hebsgaard, M. B., Brand, T. B., Hofreiter, M., Bunce, M., Poinar, H. N., Dahl-Jensen, D., Johnsen, S., Steffensen, J. P., Bennike, O., Schwenninger, J.-L., Nathan, R., Armitage, S., de Hoog, C.-J., Alfimov, V., Christl, M., Beer, J., Muscheler, R., Barker, J., Sharp, M., Penkman, K. E. H., Haile, J., Taberlet, P., Gilbert, M. T. P., Casoli, A., Campani, E., and Collins, M. J.: Ancient biomolecules from deep ice cores reveal a forested southern Greenland, Science, 317, 111–114, https://doi.org/10.1126/science.1141758, 2007.

Wu, C.-H. and Tsai, P.-C.: Impact of orbitally-driven seasonal insolation changes on Afro-Asian summer monsoons through the Holocene, Commun. Earth Environ., 2, 4, https://doi.org/10.1038/s43247-020-00073-8, 2021.

Yau, A. M., Bender, M. L., Robinson, A., and Brook, E. J.: Reconstructing the last interglacial at Summit, Greenland: Insights from GISP2, Proceedings of the National Academy of Sciences, 113, 9710–9715, https://doi.org/10.1073/pnas.1524766113, 2016a.

Yau, A. M., Bender, M. L., Blunier, T., and Jouzel, J.: Setting a chronology for the basal ice at Dye-3 and GRIP: Implications for the long-term stability of the Greenland Ice Sheet, Earth and Planetary Science Letters, 451, 1–9, https://doi.org/10.1016/j.epsl.2016.06.053, 2016b.

Yin, Q. Z. and Berger, A.: Individual contribution of insolation and CO_2 to the interglacial climates of the past 800,000 years, Clim. Dyn., 38, 709–724, https://doi.org/10.1007/s00382-011-1013-5, 2012.

Yin, Q. and Berger, A.: Interglacial analogues of the Holocene and its natural near future, Quaternary Science Reviews, 120, 28–46, https://doi.org/10.1016/j.quascirev.2015.04.008, 2015.

Yin, Q. Z., Wu, Z. P., Berger, A., Goosse, H., and Hodell, D.: Insolation triggered abrupt weakening of Atlantic circulation at the end of interglacials, Science, 373, 1035–1040, https://doi.org/10.1126/science.abg1737, 2021.

Yuan, X., M. R. Kaplan, and Cane, M. A.: The interconnected global climate system—a review of tropical-polar teleconnections, J. Climate, 31, 5765-5792, https://doi.org/10.1175/JCLI-D-16-0637.1, 2018.

Zhu, J., Liu, Z., Zhang, J., and Liu, W.: AMOC response to global warming: dependence on the background climate and response timescale, Clim Dyn, 44, 3449–3468, https://doi.org/10.1007/s00382-014-2165-x, 2015.